Title

Creep Properties and Dislocation Kinetics of Dispersion-Strengthened Alloys and Multi-Principal Element Alloys

Author

Zhang, Mingwei

Publication Date

2021

Peer reviewed|Thesis/dissertation

Creep Properties and Dislocation Kinetics of Dispersion-Strengthened Alloys and Multi-Principal Element Alloys

By

MINGWEI ZHANG
DISSERTATION

Submitted in partial satisfaction of the requirements for the degree of

DOCTOR OF PHILOSOPHY

in

Materials Science and Engineering

in the

OFFICE OF GRADUATE STUDIES

of the

UNIVERSITY OF CALIFORNIA

DAVIS

Approved:

Jeffery C. Gibeling, Chair

Jeremy K. Mason

Sabyasachi Sen

Committee in Charge

2021

This dissertation is dedicated to my parents, Ruizhong Zhang and Haifang Huang, and my fiancée, Jingxuan Zhang.

Abstract

Constant stress and stress reduction creep experiments were conducted on several dispersion-strengthened (DS) alloys, GlidCop Al-15 and Al-60 (Cu-Al_2O_3), GRCop-84 (Cu-Cr_2Nb), and FVS0812 (Al-$Al_{13}(Fe,V)_3Si$); and a single phase FCC multi-principal element alloy (MPEA), CrMnFeCoNi, to characterize their creep properties and determine their rate-controlling deformation mechanisms at elevated temperatures. The analysis involves the measurement of the stress exponents and apparent activation energies of creep by constant stress creep experiments, and the determination of the operational activation area, constant structure activation energies, and microstructural strengths by stress reduction experiments. Thereafter, extensive scanning electron microscopy (SEM) and transmission electron microscopy (TEM) characterization of creep microstructure was performed for proper interpretation of the mechanical insights. Finally, physics-based constitutive equations of creep were established based on the output from the creep experiments to describe and predict the creep behavior of these alloys.

The stress exponents and apparent activation energies have previously been measured for DS alloys, and their abnormally high values cannot be rationalized by mechanisms that operate in metals and alloys without dispersoids, thus indicating the importance of dislocation-particle interactions. In the current study, the operational activation areas determined for GlidCop Al-15 and Al-60, GRCop-84, and FVS0812 revealed their rate-controlling deformation mechanisms to be thermally active dislocation detachment from particles, local climb over particles, and interdislocation interactions, respectively, which were also supported by corresponding TEM characterization. These results indicate that a unified model that describes creep in all DS alloys

does not exist, and the respective deformation mechanisms must be well understood in different DS alloys and modeled accordingly.

A uniform stress exponent of 3.7±0.1 was determined for CrMnFeCoNi tested at constant stresses from 1023 to 1173 K, demonstrating no change of dominating deformation mechanisms across all tested stresses. The apparent activation energy turned out to be lower than that of self-diffusion for all five elements in the high entropy matrix and decrease with increasing stress, revealing a stress-assisted, thermally activated behavior. Electron backscatter diffraction (EBSD) and TEM characterization showed no subgrain boundary formation during steady-state creep deformation in CrMnFeCoNi. Instead, the dislocation substructure features high-density arrays of curved and entangled dislocations, illustrating combined control of forest dislocations and concentrated solid solution. These mechanisms were quantitatively verified by the stress reduction creep experiments conducted at 1073 K. The measured activation areas were quantitatively separated by a Haasen plot, and their respective values are appropriate for the two determined mechanisms. The elevated-temperature deformation mode in CrMnFeCoNi appears to be the same as that at room and cryogenic temperatures, suggesting the possibility of a unified framework to describe plastic deformation in this MPEA from cryogenic to elevated temperatures.

Acknowledgements

The completion of this dissertation will truly be impossible without the support from my family, friends, mentors, colleagues, and the materials science and engineering community; I am indebted to them all. Among all who have unselfishly offered their help and company during the course of this exciting journey, I would like to give my special thanks to some outstanding people who have made significant contributions to my work and my life.

I would like to express my sincerest gratitude to my Ph.D. advisor, Prof. Jeffery Gibeling. He is the greatest mentor a graduate student can ever ask for. I learned from him the highest standards of academic integrity, research philosophy, technical knowledge, teaching and interpersonal skills, and even the sense of humor. These important qualities have shaped me to become a better researcher and a better person, and they are the invaluable qualities that I hope to hold on to for the rest of my life. I am also deeply grateful to the other faculty members on my dissertation committee, Profs. Jeremy Mason and Sabyasachi Sen, along with two other professors that constitute my qualifying exam committee, Profs. Michael Hill and Valeria La Saponara; without their guidance and support, I will never be able to finish this dissertation.

My graduate life is blessed with the unwavering love and unconditional support from my family. My parents, Ruizhong Zhang and Haifang Huang, have always had faith in me and provided me with an exceptional learning environment that has shaped my personality and passion towards materials science. The enlightenment, encouragement, and enduring given by my fiancée, Jingxuan Zhang, have been unparalleled. Without her understanding and care, I would not be

able to sail through the choppy waters of graduate school. Thereby, I dedicate this dissertation to the three of them.

I am especially grateful to my fellow students, Bill Bania, Jeffery Lord, Gianmarco Monfared, Dayane Oliveira, Boyi Qu, Christine Smudde, and Bing Yuan, for their friendship and camaraderie. I am most fortunate to have this special “family” in Davis.

I would like to thank Dr. Easo George at the Oak Ridge National Laboratory for kindly providing us the CrMnFeCoNi high-entropy alloy for creep testing. I also owe my gratitude to Dr. Andrew Thron for teaching me many of the skills on electron microscopes and sample preparation. The beautiful images in this dissertation are constant reminders of his input in my work. In addition, I am grateful to Dr. Krishna Yaddanapudi for his TEM work performed on the deformed CrMnFeCoNi.

Finally, I would like to thank the Department of Materials Science and Engineering, the Graduate Studies, Prof. Jeffery Gibeling, Mr. Jeffrey Erhardt and Prof. Yayoi Takamura, Alfred and Marie Gibeling for the fellowships. Their kind support have benefited me in many ways through graduate school and urged me to give back to the community in the future.

Table of Contents

List of Figures

List of Tables

Chapter 1 Introduction

The recent development of deformation-resistant, damage-tolerant structural materials has highlighted the importance of incorporating synergistic hardening routes to achieve exceptional mechanical properties [1-4]. An incomplete list of currently known hardening mechanisms includes grain boundary strengthening, strain hardening, deformation twin boundary strengthening, martensitic transformation, solid solution hardening, precipitation hardening, and dispersion strengthening. Among the above mechanisms, solid solution hardening and dispersion strengthening are of central importance for materials serving at extremely high temperatures because they remain reliable regardless of the increasingly active recovery/diffusion and phase dissolution effects that disable most of the other hardening methods. Therefore, the future development of engineering materials operating under extreme creep conditions is foreseen to pursue an optimal synergy between these two hardening mechanisms. In order to achieve this goal, a thorough understanding of the fundamental deformation mechanisms and a quantitative description of their respective contributions to creep strength must be established.

Dispersion-strengthened (DS) alloys are characterized by a fine distribution of refractory particles that hinders the propagation of dislocations during plastic deformation and thereby significantly increase the strength of the matrix material at creep temperatures. Over history, the creep behavior of DS alloys has been modeled using a variety of approaches starting from simple phenomenological models that involve extensive data fitting to physics-based models that focus on the kinetics of the rate-controlling process(es) [5-7]. Specifically, detailed descriptions of

dislocation-particle interactions at elevated temperatures, including dislocation local climb and general climb over the particles [8-17], thermally activated dislocation detachment from attractive particle/matrix interfaces [18, 19], along with the effects of diffusive particle/matrix interface [20-22] and particle-induced internal stress [17, 23, 24], were established and applied to construct physics-based constitutive creep models with overall success. However, these models have been applied interchangeably to a wide variety of DS alloys, and typically, the model selection is only based on the knowledge of the size and volume fraction of the dispersoids, the nature of the particle-matrix interface, and limited *ex-situ* TEM evidence that shows dislocation-particle interactions. Difficulty often arises when the selected model fails due to the fact that the hypothesized subprocess is not actually rate-controlling. Furthermore, there is little connection between the different models resulting in seemingly isolated approaches. Therefore, it is highly desirable to conduct a detailed mechanistic study on the DS alloys that integrates mechanical and microscopic information into quantitative physical insights of the rate-controlling deformation mechanism(s), which will eventually lead to a comprehensive model that unites current theories.

Recently, the development of high-entropy alloys (HEAs) and medium-entropy alloys (MEAs), together also known as multi-principal element alloys (MPEAs), provides vast opportunities to design new alloys with desirable mechanical properties that can meet the challenges of serving under extreme creep conditions. This new class of alloys is featured by a composition consisting of at least three principal elements (> 10 at. %), thereby standing as a concentrated solid solution. A primary example class among all MPEAs is the CrCoNi-based single phase FCC alloys that have been shown to possess superior oxidation and corrosion resistance and excellent cryogenic and room temperature strength and ductility [1, 25, 26]. Due to their increased capacity for solid

solution hardening, these MPEAs are endowed with great potential to replace pure metals and conventional alloys as the new matrix material to develop MPEA-based DS alloys and superalloys with enhanced creep resistance compared to current DS alloys and Ni-based superalloys. In fact, prototypes of high entropy superalloys [27] and DS-MPEAs [28] have been developed, displaying promising high temperature strength and ductility. However, creep and high temperature tensile or nanoindentation data for MPEAs are generally lacking to date, and dedicated mechanistic studies are completely nonexistent. It is therefore of immediate research interest to understand the creep properties and deformation mechanisms of the matrix MPEA before any physics-based model for high entropy superalloys and DS-MPEAs can be constructed.

The overarching goal of this dissertation is to systematically investigate the creep behavior and deformation mechanisms in two material systems: (i) conventional DS alloys with FCC metal or dilute alloy matrix; and (ii) FCC MPEAs using a combination of standard constant stress creep tests, mechanism-probing constant structure creep experiments, and extensive microstructural characterization. The seemingly separated studies on these two types of materials are in fact deeply interconnected in both scientific and engineering aspects (i.e., shared theoretical framework for dislocation glide and shared information to guide the design of the same target material) and are expected to provide important insights into the development of DS-MPEAs.

The results of this dissertation are separated into five self-contained chapters which have also been published or submitted to in scientific journals, and an overview of the following chapters is provided as follows: Chapter 2-4 provides the characterization of creep properties and

quantitative analysis of dislocation kinetics across a broad spectrum of DS-alloys with various natures of particle/matrix interface, particle size and distribution, and particle volume fraction. Chapter 2 describes a study of the creep mechanism of thermally activated dislocation detachment from particles in a model DS alloy with incoherent interface and low particle volume fraction, GlidCop (Cu-Al_2O_3), and an improved version of the customary Rösler-Arzt model by including the insights from constant structure creep experiments. This study is in collaboration with Dr. Stuart Broyles as a part of the steady-state creep and stress reduction creep data was originally measured by him as a part of his dissertation [29]; Chapter 3 extends the study to another DS-Cu alloy also with incoherent interfaces, GRCop-84 (Cu-Cr_2Nb), but with a higher particle volume fraction and a larger particle size; Chapter 4 examines a DS-Al alloy with coherent interface and much higher particle volume fraction, FVS0812 (Al-$Al_{13}(Fe,V)_3Si$), highlighting the difference in creep mechanisms from the prior DS-alloys caused by the difference in the nature of the particle/matrix interface and particle volume fraction. This study is in collaboration with Robert Lewis as the steady-state creep and stress reduction creep data were originally measured by him as a part of his thesis [30]; Chapters 5 and 6 constitute a complete study of the creep properties, creep microstructure, and deformation mechanisms of an FCC MPEA, CrMnFeCoNi. This specific variant in the CrCoNi family was selected because it is the most widely studied MPEA to date, allowing a detailed comparison of its elevated-temperature deformation behavior with its well-known room and low-temperature properties. Chapter 5 gives the basic creep information and steady-state creep microstructure; and Chapter 6 provides a comprehensive mechanistic study on CrMnFeCoNi, revealing its rate-controlling deformation modes at elevated temperatures. Finally, all raw creep data presented in this dissertation are tabulated in the **Appendix**.

References

[1] B. Gludovatz, A. Hohenwarter, D. Catoor, E.H. Chang, E.P. George, R.O. Ritchie, Science 345(6201) (2014) 1153-1158.
[2] Z. Li, K.G. Pradeep, Y. Deng, D. Raabe, C.C. Tasan, Nature 534(7606) (2016) 227-30.
[3] X.T. Fang, G.Z. He, C. Zheng, X.L. Ma, D. Kaoumi, Y.S. Li, Y.T. Zhu, Acta Mater. 186 (2020) 644-655.
[4] Y.T. Chen, Y.J. Chang, H. Murakami, T. Sasaki, K. Hono, C.W. Li, K. Kakehi, J.W. Yeh, A.C. Yeh, Sci. Rep. 10(1) (2020) 12163.
[5] W. Blum, B. Reppich, Creep of particle-strengthened alloys, Pineridge Press Ltd., Creep Behaviour of Crystalline Solids (1985) 83-135.
[6] M. Heilmaier, B. Reppich, Particle threshold stresses in high temperature yielding and creep: a critical review, Creep Behavior of Advanced Materials for the 21st Century (1999) 267-281.
[7] C.M. Sellars, R.A. Petkovic-Luton, Mater. Sci. Eng. 46(1) (1980) 75-87.
[8] L. Brown, R. Ham, Dislocation-particle interactions, Strengthening methods in crystals (1971) 9-135.
[9] R. Lagneborg, Scr. Metall. 7(6) (1973) 605-613.
[10] J. Rösler, E. Arzt, Acta Metall. 36(4) (1988) 1043-1051.
[11] E. Arzt, J. Rosler, Acta Metall. 36(4) (1988) 1053-1060.
[12] E. Arzt, M.F. Ashby, Scr. Metall. Mater. 16 (1982) 1285-1290.
[13] M. McLean, Acta Metall. 33(4) (1985) 545-556.
[14] R.S.W. Shewfelt, L.M. Brown, Philos. Mag. A 30(5) (1974) 1135-1145.
[15] R.S.W. Shewfelt, L.M. Brown, Philos. Mag. A 35(4) (1977) 945-962.
[16] R.A. Stevens, P.E.J. Flewitt, Acta Metall. 29(5) (1981) 867-882.
[17] J.H. Hausselt, W.D. Nix, Acta Metall. 25(12) (1977) 1491-1502.
[18] J. Rosler, E. Arzt, Creep in Dispersion Strengthened Aluminum-Alloys at High-Temperatures - a Model Based Approach, New Materials by Mechanical Alloying Techniques (1989) 279-286.
[19] J. Rösler, E. Arzt, Acta Metall. Mater. 38(4) (1990) 671-683.
[20] R.C. Koeller, R. Raj, Acta Metall. 26(10) (1978) 1551-1558.
[21] T. Mori, M. Okabe, T. Mura, Acta Metall. 28(3) (1980) 319-325.
[22] D.J. Srolovitz, R.A. Petkovic-luton, M.J. Litton, Philos. Mag. A 48(5) (1983) 795-809.
[23] C.N. Ahlquist, W.D. Nix, Acta. Metall. 19(4) (1971) 373-&.
[24] W. Blum, E. Weckert, Mater. Sci. Eng. 86 (1987) 145-158.
[25] B. Gludovatz, A. Hohenwarter, K.V.S. Thurston, H.B. Bei, Z.G. Wu, E.P. George, R.O. Ritchie, Nat. Commun. 7 (2016).
[26] G. Laplanche, A. Kostka, C. Reinhart, J. Hunfeld, G. Eggeler, E.P. George, Acta Mater. 128 (2017) 292-303.
[27] T.K. Tsao, A.C. Yeh, C.M. Kuo, K. Kakehi, H. Murakami, J.W. Yeh, S.R. Jian, Sci. Rep. 7(1) (2017) 12658.
[28] T.M. Smith, A.C. Thompson, T.P. Gabb, C.L. Bowman, C.A. Kantzos, Sci. Rep. 10(1) (2020).
[29] S.E. Broyles, Ph.D. Dissertation, University of California, Davis (1995).
[30] R.J. Lewis, Master's Thesis, University of California, Davis (1990).

Chapter 2 An Improved Description of Creep in Dispersion-Strengthened Metals[1]

2.1 Introduction

The Rösler-Arzt (RA) model established in the late 1980's and early 1990's represents a significant advancement towards understanding the deformation mechanisms of dispersion-strengthened (DS) alloys and quantitatively predicting the steady-state creep rates of those materials [1]. This physics-based model recognizes thermally activated dislocation detachment from particles as the rate-controlling process of creep deformation at elevated temperatures when the relaxation energy for dislocations at the incoherent particle/matrix interface is sufficiently high. It gives the steady-state creep rate (as tensile strain rate), $\dot{\epsilon}_{SS}$, in the following form:

$$\dot{\epsilon}_{SS} = \frac{6D_v\lambda\rho}{Mb} exp\left[-\frac{\mu b^2 r}{k_B T}(1-k)^{3/2}\left(1-\frac{\sigma}{\sigma_D}\right)^{3/2}\right] \quad (2.1)$$

where M is the Taylor factor of the material, D_v is the lattice vacancy diffusion coefficient, λ is the half interparticle spacing, ρ is the dislocation density, b is the Burgers vector, μ is the shear modulus, r is the particle radius, k_B is the Boltzmann factor, T is the temperature, k is an interaction parameter that describes the extent of relaxation of dislocation line energy at the particle/matrix interface, σ is the applied stress, and σ_D is the athermal detachment stress, which is essentially the strength of the material at 0 K. Because the dislocations must climb over the particles and reach the departure side prior to detachment, the RA model is only applicable when the detachment process is slower than the climb process, which translates to conditions of $k <$

[1]Published as M. Zhang, S.E. Broyles, J.C. Gibeling, *Acta Mater*. **196** (2020) 384-395

0.94 assuming a uniform distribution of particles [1]. In practice, σ_D can be experimentally determined by:

$$\frac{\sigma}{\sigma_D} = \left(\frac{3\left(Q_{app} - Q_c\right)}{2RT \cdot n_{app}\left(1 - \frac{\partial \mu}{\partial T} \cdot \frac{T}{\mu}\right)} + 1 \right)^{-1} \tag{2.2}$$

where Q_c is the activation energy for creep in pure metal matrix, R is the ideal gas constant, and n_{app} and Q_{app} are the apparent stress exponent and activation energy derived from the power-law model of creep deformation [2]:

$$\dot{\epsilon}_{SS} = A\sigma^{n_{app}} exp\left(-\frac{Q_{app}}{RT}\right) \tag{2.3}$$

in which A is a constant. Similarly, k can be determined from:

$$k = 1 - \left(\frac{2k_B T}{3\mu b^2 r} \cdot \frac{n_{app}}{\left(1 - \frac{\sigma}{\sigma_D}\right)^{1/2}\left(\frac{\sigma}{\sigma_D}\right)} \right)^{2/3} \tag{2.4}$$

The RA model has been successfully applied to various DS alloy systems (e.g. Al, Fe, Cu) over the years [3-5] and is regarded as an appropriate alternative to the traditional phenomenological power-law model (Eqn. 2.3) in describing the creep behavior of DS alloys, as the latter gives abnormally high stress exponents and activation energies that are difficult to rationalize [6]. However, it is important to realize that the RA model has several critical limitations that have left room for refinement. A few studies critically assessed the application of the RA model to DS alloys [7-9], and several issues were identified: i) k plays a critical role in the RA model, but it

cannot be theoretically predicted; ii) both $\dot{\epsilon}_{SS}$ and k are highly sensitive to the value of Q_{app} based on Eqns. 2.1-2.4, but that parameter varies substantially with the number of available data points and the way it is determined (e.g. by an Arrhenius plot at a constant stress across all temperatures, or across only two closely spaced isotherms); and iii) the dislocation density ρ is assumed to be a constant under different stresses at a certain temperature, which is not a good assumption, and the fitted values of this parameter are often unreasonably large. The arguments listed above primarily focus on practical issues during application of the model. However, there are also more general drawbacks that originate from the basic assumptions that the model incorporates: i) the RA model cannot explain the threshold behavior that is often observed in dispersion-strengthened alloys as noted originally by Rösler and Arzt [1], and it actually predicts the opposite trend of too-high creep rates at low stresses (σ_D should not be confused with the true threshold stress, see Ref. [10]); and ii) the RA model ignores dislocation-dislocation interactions, even though the dislocation detachment process is also likely to be influenced by the presence of other nearby dislocations.

The deficiencies listed above can be mitigated by including an additional experimental method that is able to produce an independent set of data to refine the RA model, namely, constant structure creep tests. The rationale and merits of this method are described in detail in **Section 2**. Through these tests, the transient response of the material to the sudden stress reduction provides additional information apart from the steady-state creep rates corresponding to the initial and reduced stresses. The goal of the present work was to use such stress reduction tests to refine the original RA model by incorporating these new observations. The materials chosen for this investigation were GlidCop Al-15 and Al-60, in which the pure copper matrix is strengthened by

fine cubic γ-Al_2O_3 particles of 0.7 and 2.7 vol. %, respectively [11]. Our motivation for choosing these alloys is that they represent the ideal case for application of the RA model: a pure metal matrix with a single dispersoid type. Further, the steady-state creep behavior and RA model fit results for this very type of DS alloy were partially described in our previous study [5], and the necessary microstructural parameters (e.g. grain size, particle size, particle spacing) are also available in literature [12-14]. In a recent paper [15] we have shown that grain size and texture have a very limited influence on the creep behavior of GlidCop. Therefore, the contributions from these two factors are not considered in this investigation. Still, multiple forms of GlidCop need to be included to thoroughly examine the effects caused by particle/matrix interface, particle size and particle spacing. Earlier research [11] suggests that long-term annealing of extruded GlidCop facilitates the transformation of Al_2O_3 particles to $9Al_2O_3$-B_2O_3 that results in an interface with a lower k value, whereas the particle size and spacing remain about the same. On the other hand, larger particles and interparticle spacing are present for GlidCop Al-60 than in Al-15 because of the larger fraction of Al atoms. Therefore, three versions of GlidCop were tested and are compared to each other in the present study: as-received extruded Al-15 (Al-15 AR), annealed Al-15 (Al-15 AN) and as-received extruded Al-60 (Al-60 AR).

2.2 Theoretical Background

The theoretical basis for understanding stress reduction creep tests is the thermally-activated dislocation glide model described by Kocks, Argon and Ashby [16]:

$$\dot{\epsilon} = \dot{\epsilon}_0 exp\left(-\frac{\Delta G}{RT}\right) = f(\sigma, T, \hat{\sigma}_i) \tag{2.5}$$

where $\dot{\epsilon}_0$ is a constant, and ΔG is the free energy of thermal activation. Eqn. 2.5 indicates that the strain rate is determined by the thermal release of glide dislocations from obstacles and is a function of the applied stress, temperature, and the current microstructural strength of the material which is described by *i* structure parameters $\hat{\sigma}_i$ (e.g. dislocation density, subgrain size, particle size and spacing, etc.). Therefore, the microstructure of the material can be mechanically probed by changing σ and recording the response of $\dot{\epsilon}$ while holding T and $\hat{\sigma}_i$ constant. This experimental approach is based on the assumption that the microstructural elements of interest remain unaltered before and after the stress reduction in a short time interval to exclude any change in strain rate associated with the evolution of the microstructure. Although truly keeping every aspect of the internal structure constant is idealistic, this assumption is widely validated by various studies [17-21] through the continuing effort to improve strain and time resolution in experimental setups so that data acquisition is much faster than microstructural rearrangement. Thus, such tests are termed "constant structure creep tests" in these studies. The creep curve in the stress reduction transient is characterized by a constant structure creep rate, $\dot{\epsilon}_C$, which gives the rate of deformation under the reduced stress but with the microstructure developed by the initial stress. One of the most important parameters that can be determined in this type of test is the operational activation area for dislocation glide:

$$\Delta a'' = \frac{M k_B T}{b} \cdot \left. \frac{\partial ln \dot{\epsilon}_C}{\partial \sigma} \right|_{T,\hat{\sigma}_i} \tag{2.6}$$

The physical meaning of the operational activation area and its difference compared to the true activation area, Δa^*, and apparent activation area, $\Delta a'$, are discussed in detail in Ref. [16], and therefore not elaborated on here. $\Delta a''$ reflects the length scale of the dislocation segments pinned

between two neighboring rate-controlling obstacles, and thus is very helpful in identifying the dominant rate controlling obstacle(s). It takes the value of 1~10 b^2 for lattice friction [22], 100 b^2 for dilute solid solution hardening [23], and approximately 100 - 1000 b^2 and proportional to forest dislocation spacing for dislocation hardening [24]. However, $\Delta a''$ has not yet been documented for oxide dispersion strengthened (ODS) copper, and thus one goal of the present work is to determine the activation area involved in the dislocation detachment process.

The Gibbs free energy of activation, ΔG, in Eqn. 2.5 can be described by a phenomenological model [16]:

$$\Delta G = \Delta F \left[1 - \left(\frac{\sigma}{\hat{\sigma}}\right)^p\right]^q \tag{2.7}$$

where $\hat{\sigma}$ is the maximum glide resistance provided by the microstructure, which can be also interpreted as the flow stress at 0 K. $\Delta F = \Delta G + \tau b \Delta a'' = \Delta G + \sigma/M \cdot b \Delta a''$ is the Helmholtz free energy of thermal activation which consists of the sum of the free energy of activation and the work done by the external stress. In Eqn. 2.7, p describes the range and q describes the strength of the thermal barrier. The determination of the thermal activation parameters given above is discussed in detail in the results and discussion section of this paper. It is also important to note that ΔG is a more fundamental parameter than Q_{app} because it is determined at constant structure, whereas Q_{app} is obtained across various steady-state strain rates that have different microstructures.

2.3 Experimental

2.3.1 Materials and Creep Sample Preparation

Extruded GlidCop Al-15 (C15715) and GlidCop Al-60 (C15760) with low oxygen content were provided by SCM Metal Products (now North American Höganäs) and the nominal chemical compositions are shown in **Table 2-1**. All aluminum atoms were internally oxidized to Al_2O_3 particles and the remaining oxygen atoms are limited by the addition of boron. Detailed microstructural studies of the as-received materials were provided elsewhere [5, 12, 14], and only relevant microstructural parameters are tabulated in **Table 2-1**. Electro-discharge machining (EDM) was used to machine flat tensile specimens from the stock with a nominal gauge length of 20.32 mm, gauge width of 2.54 mm and a thickness of 0.762 mm for Al-15 AR and Al-15 AN, and 0.635 mm for Al-60 AR. The samples were then mechanically polished to a 600-grit finish to ameliorate effects caused by surface asperities. Several Al-15 AR specimens were annealed for 100 hours at 1273 K under a vacuum level at or below 5×10^{-4} Pa to produce the Al-15 AN specimens.

Table 2-1. Chemical composition and particle dimensions of GlidCop Al-15 and Al-60.

Alloy	Cu (wt. %)	Al (wt. %) [11]	B (wt. %) [11]	Al_2O_3 content (vol. %) [11]	Particle diameter (nm) [5, 9]	Particle spacing (nm) [5]
Al-15	Balance	0.15	0.015	0.7	5	86.5
Al-60	Balance	0.60	0.015	2.7	10	88.1

2.3.2 Creep Testing Procedures

The creep testing equipment and procedures used in this study are the same as those used in our previous steady-state and constant structure creep studies [15, 19, 20]. Creep experiments were

carried out in vacuum and at constant true stress by using an Andrade-Chalmers lever arm [25] except for one abrupt stress reduction during the creep test for each sample. The creep specimens were first loaded to the initial stress σ_{in} which would then produce the steady state creep rate of $\dot{\epsilon}_A$. Here we use the notation of Gibeling and Biberger [18] to describe the different creep rates before and after the stress reduction. A stress reduction was then initiated by manually removing part of the load from the arm. The constant structure creep rate $\dot{\epsilon}_C$ was calculated by a least squares linear regression of the strain-time data after the stress reduction. The samples were subsequently allowed to deform under the reduced stress σ_{red} to a new steady state with creep rate $\dot{\epsilon}_D$. The initial and reduced stresses used in the creep tests are listed in **Table 2-2**. Finally, the samples were furnace cooled to room temperature under stress.

Significant improvement of strain measurement and data acquisition compared to previous work was achieved in this study. A custom quartz tube and rod assembly was used to attach a LVDT to the specimen to measure strain directly at the specimen [15]. The strain was measured by a Schaevitz 250 MHR linear variable differential transformer (LVDT), whose signal was then conditioned by a 3230 Daytronics signal conditioner. The strain transient was recorded by an improved data acquisition system consisting of two Hewlett-Packard 3457A digital voltmeters (DVMs) and a Keithley-Metrabyte CTM-05 counter/timer card. The range of the output LVDT signal was tuned to be identical to the range of the DVMs at ±3V (thus providing full 6.5-digit voltage resolution). In addition, the inclusion of a CTM-05 card to trigger voltmeter readings and measure time improved the time resolution and isolated the time sampling process to eliminate the possible lag generated by the test software calling the internal computer clock for time information. Those efforts yielded a maximum strain resolution of 8×10^{-8}, a time resolution of 1

μs, and a maximum data acquisition rate of 66.7 Hz. The new system provided better strain and time resolutions compared to other systems described in literature at 5×10^{-7}-1×10^{-6} and 25-55 ms, respectively [17, 19, 21]. In practice, the accuracy of any measurements (including those in the literature) will be lower than these resolution levels due to systematic and random errors, but efforts were made to minimize the former and account for the latter in the data analysis. For example, the extensometer assembly was carefully balanced by a counterweight on the opposite side of the specimen to ensure that no systematic bending strains were introduced.

Table 2-2 Initial and reduced stresses selected for stress reduction creep tests. Each sample was subjected only to one stress reduction.

Material	σ_{in} (MPa)	σ_{red} (MPa)
Al-15 AR	70	50, 40, 28, 20
Al-15 AN	70	55, 50, 45, 40, 35, 30
Al-60 AR	70	60, 55, 50, 45, 40
Al-60 AR	80	60, 50, 40
Al-60 AR	60	50, 45

2.4 Results and Discussion

2.4.1 Steady-state Creep Behavior

We have previously described the steady-state creep behavior of Al-15 AR and Al-15 AN in detail, including critically reviewing the RA model and threshold stress model fits for both materials [15]. In the latter, $\dot{\epsilon}_{SS} = A'(\sigma - \sigma_{th})^{n'_{app}}$, where A' is a constant, σ_{th} is the threshold stress and n'_{app} is the new stress exponent. Similar procedures were employed for Al-60 AR in this study using the data analysis software OriginLab. The steady-state creep data and various model fits are shown in Fig. 2-1 and the fitting parameters are given in **Table 2-3**. As noted

earlier, two types of steady-state creep rates are present: those which correspond to the initial applied stress, $\dot{\epsilon}_A$, and those corresponding to the reduced stress, $\dot{\epsilon}_D$. No distinction was made in data fitting between the two strain rates since they appear to overlap with each other. As mentioned above, the RA model cannot describe the true threshold so that the data points that indicate threshold behavior (below the horizontal dashed line in Fig. 2-1) were omitted when fitting the model. The RA model gives a good representation of the data outside of the threshold regime. The threshold stress model also provides a moderately good description of creep for GlidCop, although it is purely phenomenological and lacks a coherent physical interpretation. In general, GlidCop Al-60 shows superior creep resistance compared to Al-15 as expected because a greater volume fraction of Al_2O_3 particles is present to impede dislocation motion.

Table 2-3 The values of the fitting parameters that describe the stress dependence of the steady-state creep rate of Al-15 AR, Al-15 AN and Al-60 AR at 973 K using the power-law model, threshold stress model and Rösler-Arzt model.

Model	Power-law	Threshold stress		Rösler-Arzt model	
Material	n_{app}	n'_{app}	σ_{th} (MPa)	k	σ_D (MPa)
Al-15 AR [5]	10.7	5.6	20.0	0.915	130.5
Al-15 AN [15]	14.8	7.1	23.3	0.894	160.3
Al-60 AR (this study)	12.3	6.4	31.0	0.918	213.3

2.4.2 Stress Reduction Transient Creep behavior

Fig. 2-2 shows example strain transients of Al-15 AN at a small stress reduction from 70 MPa to 50 MPa and a large stress reduction from 70 MPa to 30 MPa. Metallic materials experience an anelastic backflow following a stress reduction during creep, which is increasingly important when the stress reduction is large [26]. Such behavior can greatly affect the determination of $\dot{\epsilon}_C$ because the measured creep rate is in fact the difference between the forward creep rate resulted

from the applied stress and the backward creep rate resulted from the backflow. Therefore, only after the anelastic backflow has been carefully examined will the determination of $\dot{\epsilon}_C$ be reliable. For a small stress reduction given by Fig. 2-2a, only instantaneous elastic contraction and fast anelastic contraction were observed before constant structure creep was reached. The instantaneous elastic strain was calculated by $\frac{\sigma_{in}-\sigma_{red}}{E}$, where E = 81.9 GPa is the elastic modulus of the Cu matrix at 973 K [27]. For a large stress reduction depicted by Fig. 2-2b, the decay of anelastic contraction is considerably slower so that a transition exists before constant structure creep. The same behavior has been widely observed in pure metals [26, 28, 29], where the fast anelastic backflow is attributed to the reverse motion of dislocations in the subgrain interior, and the slower anelastic backflow is related to the relaxation of the subgrain walls. This explanation can be extrapolated to GlidCop, in which well-defined subgrains have been observed to form during creep [5, 15, 30], and the reverse motion of the dislocations on the approach side of the particles is able to account for the fast backflow. As a result, $\dot{\epsilon}_C$ must be chosen as the local maximum creep rate after anelasticity has been exhausted.

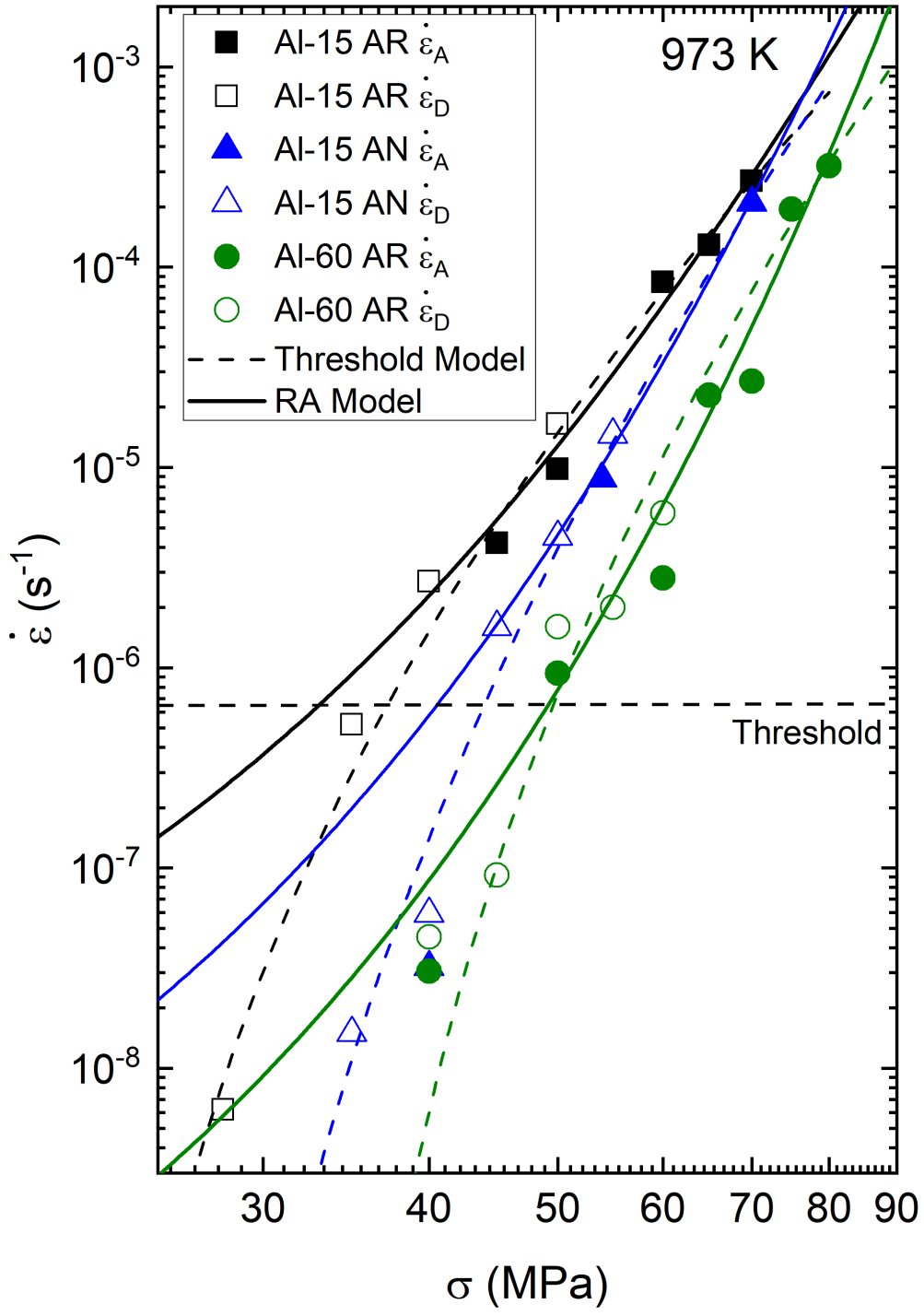

Fig. 2-1 Double Logarithmic plot of steady-state creep rate versus true applied stress for GlidCop Al-15 AR [5], Al-15 AN [15] and Al-60 AR. The solid symbols represent the steady-state creep rates corresponding to the initial applied stress and the open symbols are for those which correspond to the reduced stress. The solid lines represent the RA model and dashed lines are the threshold stress model fits to the steady-state creep data.

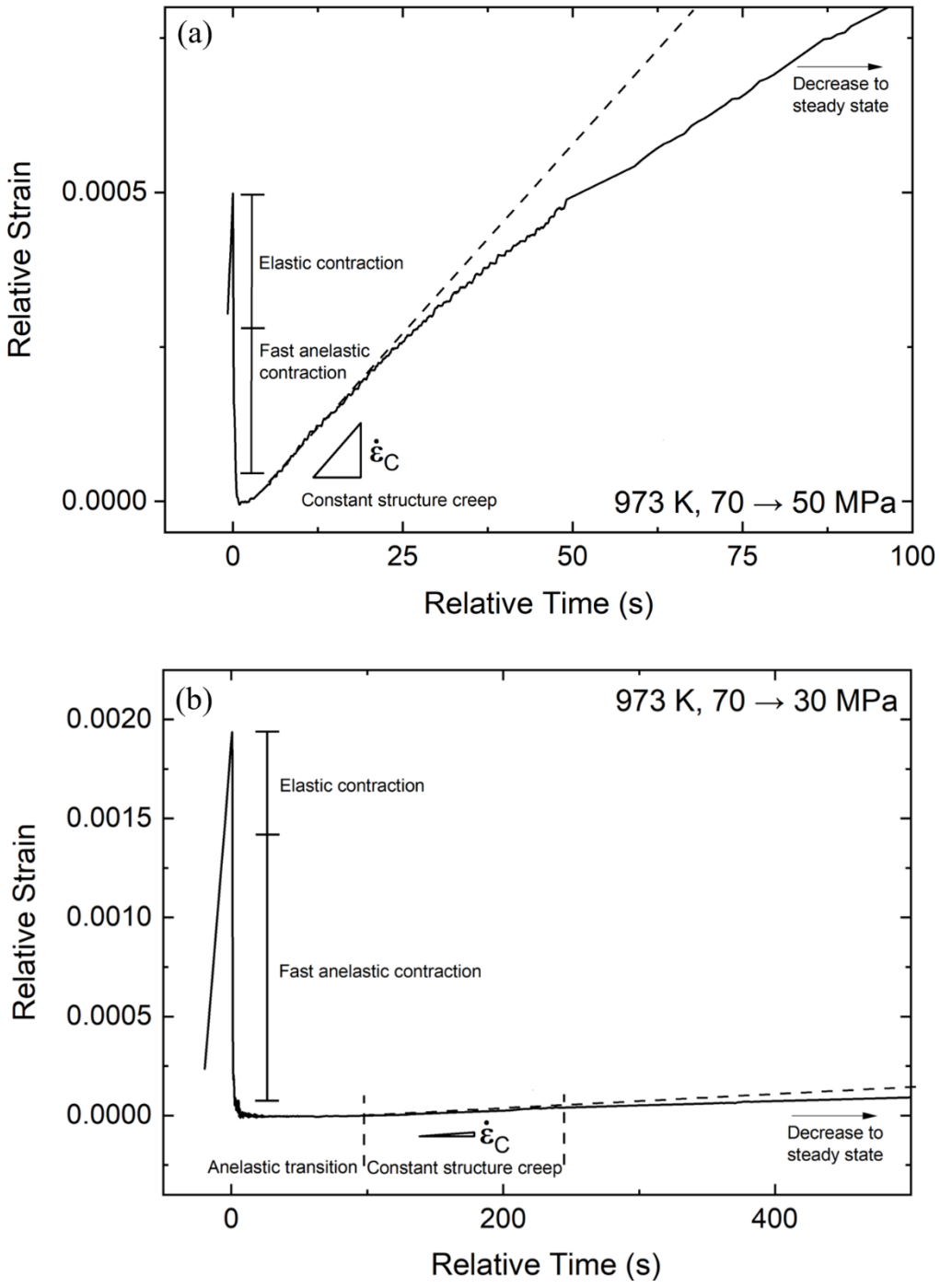

Fig. 2-2 Example creep curves of Al-15 AN at the stress reduction transients (a) from 70 MPa to 50 MPa and (b) from 70 MPa to 30 MPa. The curves were shifted both vertically and horizontally such that the minimum strain is now zero strain and the point of stress reduction is now zero time. The dashed line delineates the extension of the constant structure region of the creep curve to illustrate how $\dot{\epsilon}_C$ was determined. These stress reduction transients are qualitatively representative for all Al-15 AR, Al-15 AN and Al-60 AR specimens tested at small and large stress reductions.

From Fig. 2-2, another important observation is that the constant structure creep rate $\dot{\epsilon}_C$ decreases to the subsequent steady-state creep rate $\dot{\epsilon}_D$ for both small and large stress reductions. This observation is consistent across all stresses tested for all materials, and an example for Al-15 AN is given in Fig. 2-3, where the constant structure creep rates are always greater than the corresponding steady-state values. There are two possible explanations of the creep rate decrease following a stress reduction: the first one is the so-called "anomalous creep" such as that observed in pure Al, where extra forward strain can be created by dynamic recovery [31, 32]. However, such behavior was only observed at very large stress reductions for pure Al (~70%, i.e. $\frac{\sigma_{red}}{\sigma_{in}}$ = 30%), but the observation of constant structure rates greater than the new steady state was consistent for all stress reductions in our experiments, including very small ones of ~15%. Furthermore, the "anomalous" rates decreased to the constant structure rates in pure Al, then increased again to steady state due to subgrain coarsening (three stages of forward creep in the transient). This observation differs from the present results for DS-Cu. Recently, Sun, *et al.* [33] reported a monotonically decreasing trend for creep rates of nanocrystalline Ni after stress reduction, which is related to grain boundary recovery mechanisms. This trend even holds at small stress reductions due to the absence of subgrains. However, subgrains readily form in GlidCop and the grain size is well beyond the nanocrystalline regime. Therefore, it is more likely that the strain transient of GlidCop resembles the inverted transient behavior observed in class A alloys, where the decrease of the mobile dislocation density causes the reduction of creep rate [17, 34]. However, GlidCop does not match the characteristics of a class A alloy in other aspects. For example, the formation of subgrain boundaries in class A alloys is limited, but in GlidCop they form readily. In addition, GlidCop exhibits normal primary creep [15] (creep rate decreases to steady state upon initial loading), which is the opposite of the inverted primary that class A

alloys normally show [17, 32, 35, 36]. The normal primary creep behavior typically observed in pure metals and class M alloys is associated with subgrain formation and refinement [19, 20], which can be considered to be a hard microstructure.

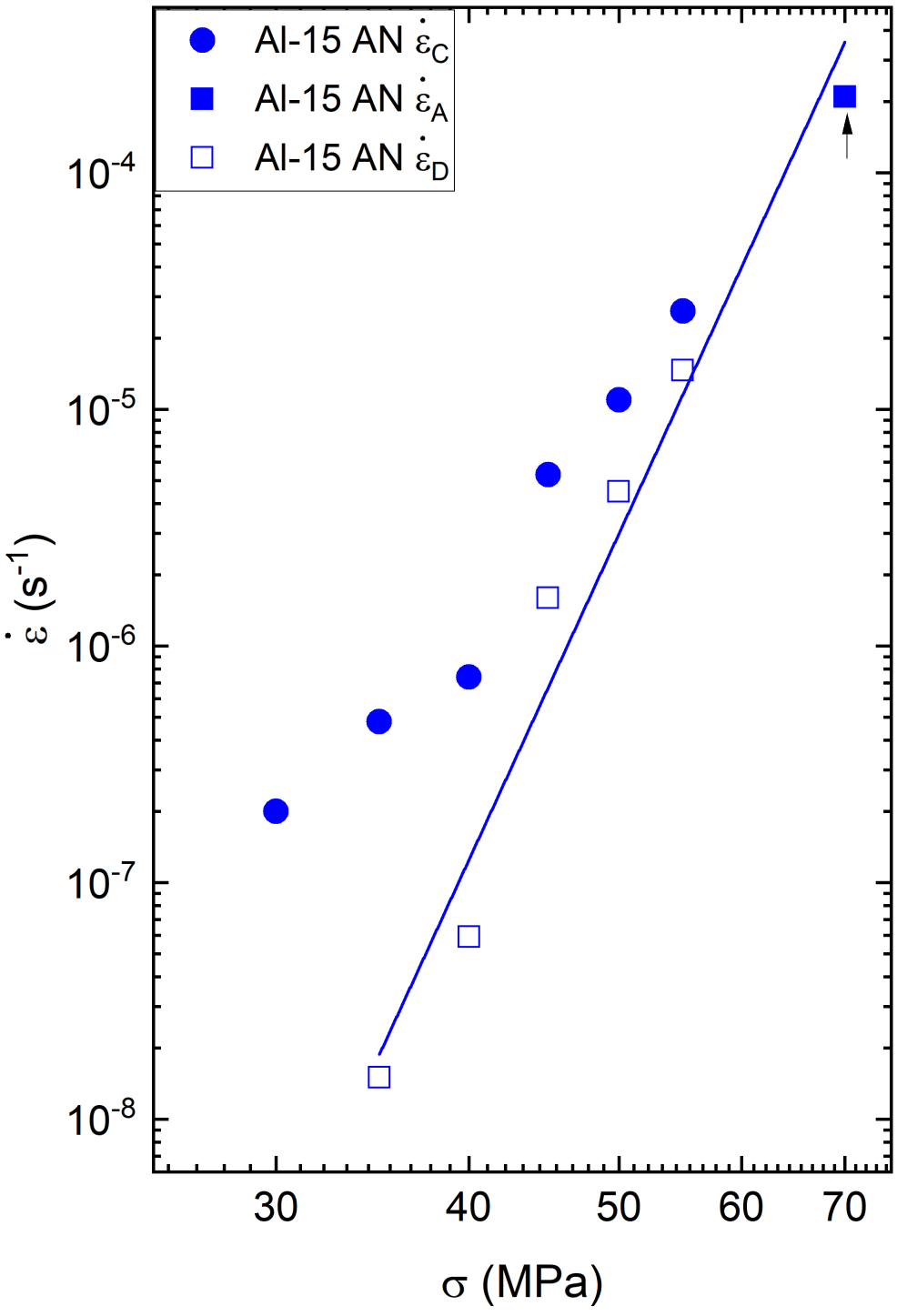

Fig. 2-3 Double logarithmic plot of both constant structure and steady-state creep rates versus true applied stress for GlidCop Al-15 AN. The black arrow indicates the initial stress before stress reduction. The solid line is a linear fit of the steady state data.

The findings in this study suggest that the ODS GlidCop alloys may exhibit behavior similar to that of pure metals or class M alloys (a normal primary and subgrain boundary formation) and other behavior similar to that of class A alloys (inverted transients with constant structure creep rates greater than the corresponding steady state rates) even though there are no solutes controlling deformation. Thus, GlidCop cannot be categorized by either type. Instead, strong evidence of dislocation particle interaction was revealed in various previous studies [5, 11, 14], and the contribution of the particles needs to be taken into account. A possible explanation is provided as follows: the normal primary creep is an indication that the mobile dislocation density decreases after loading, which can be rationalized by both the refinement of subgrains and a pinning effect as dislocations become blocked by the particles. In contrast, the inverted transient creep behavior can be explained from the viewpoint of the dislocation detachment model. If dislocation detachment is the rate determining process, it is reasonable to assume that the dislocations between the particles are stuck behind the dislocation on the departure side of the particle and are waiting for it to detach. Such a dislocation configuration exerts a forward internal stress on the critical dislocation on the departure side of the particle that governs the deformation rate. One possibility for the decreasing creep rate during the transient is therefore the decay of the forward stress after the stress reduction when the density of the dislocations between the particles diminishes and the spacing between these dislocations and the critical dislocation increases. This interpretation relies on the existence of a forward stress originating from the dislocation-dislocation interactions near particles that aids dislocation detachment, which is described in more detail in **Section 4.3**. Another important point is that the time required for GlidCop to reach the new steady state following a stress reduction scales from a few seconds to several minutes, which is much faster than pure metals that require hours or even days

at similar strain rates [26]. This observation suggests that the dislocations that affect the deformation rate during constant structure creep of ODS Cu have more freedom to move and can annihilate more quickly compared to those in pure metals that form severely entangled dislocation forests and subgrain structures. Such behavior is consistent with our hypothesized dislocation configuration because the free dislocations between the particles can climb and annihilate by combining with those which have opposite signs in a relatively short time as opposed to the coarsening of dislocation networks and subgrains in pure metals which takes a significantly longer time.

2.4.3 Thermally Activated Dislocation Glide Analysis

A quantitative description of the constant structure creep data obtained from the stress reduction tests described in **Section 4.2** cannot be provided by the RA model that only describes the steady-state strain rates. Rather, a more fundamental treatment is required to first identify the rate-controlling deformation mechanism, and then describe the creep rates in relation to the microstructure of the material. Historically, the thermally-activated dislocation glide model that considers dislocations overcoming microstructural obstacles by thermal activation is successful for pure metals and solid solutions [5, 19, 37]. Here, such an analysis is extended to ODS-Cu with certain modifications that are described in detail in the two following subsections: the determination of the operational activation area that indicates the controlling deformation mechanism; and the proposal of an effective stress that takes into account near-particle dislocation/dislocation interactions.

2.4.3.1 Operational Activation Area

As mentioned earlier, the constant structure creep data can be analyzed to determine the operational activation area. Using Eqn. 2.6, $\Delta a''$ can be calculated by obtaining the derivative $\left.\frac{\partial ln\dot{\epsilon}_C}{\partial \sigma}\right|_{T,\hat{\sigma}_i}$, which is based on the slope of the fit to the semilogarithmic plot of the constant structure creep rate as a function of stress shown on Fig. 2-4. It is paramount that the creep rates are obtained at constant structure when calculating $\Delta a''$ because this parameter is specific for a certain microstructure, and more particularly, for a certain spacing of the rate-determining obstacles and number of gliding dislocations. The value of $\Delta a''$ will not be meaningful if the derivative is taken from two separate microstructures (e.g. from two steady states) for which the spacing of the obstacles may be different. In Fig. 2-4, the data points with the largest stress on each line correspond to the initial steady-state creep rate, $\dot{\epsilon}_A$, at σ_{in}. They are also considered to be at constant structure and included in the fit because all $\dot{\epsilon}_C$ values were obtained at the same microstructure developed by the steady states at σ_{in}. Threshold behavior for the constant-structure data was not observed so that all data points were included into the linear fit. The linearity of the data points is reasonably good since R^2 for all five fits is greater than 0.97. Hence, $\left.\frac{\partial ln\dot{\epsilon}_C}{\partial \sigma}\right|_{T,\hat{\sigma}_i}$ can be considered as a constant for each initial stress. The observation that the constant structure data are linear on the semilogarithmic plot also suggests that p and q in Eqn. 2.7 can both be taken as unity. Finally, the average Taylor factor, *M*, given in Eqn. 2.6 cannot be assumed to be 3.06 for an untextured polycrystalline FCC metal [38], since the GlidCop materials are highly textured according to our previous study [15], so their values calculated by EBSD analysis (shown in **Table 2-4**) are used here.

The calculated $\Delta a''$ values are listed in **Table 2-4**, and very good agreement is reached between the $\Delta a''$ values normalized by b^2 and the interparticle spacing 2λ normalized by b. In other words, $\Delta a'' \sim 2\lambda b$. Measured 2λ values for Al-15 AN and Al-60 AR are currently unavailable in literature, but several studies point out that the particle distribution for Al-15 AN undergoes no apparent change in the annealing process [11, 15, 39], and the interparticle spacing for Al-60 AR was approximated by $\sqrt{\pi/6f} \cdot 2r$ [40], where f = 2.7% is the volume fraction of the Al_2O_3 particles. The correspondence between $\Delta a''$ and 2λ is verification that the rate-determining obstacles in creep deformation are indeed the Al_2O_3 particles. A similar activation area ~310 b^2 has been reported for an Fe–14% Cr ODS alloy that has a similar interparticle spacing (~100 nm) at 1023 K by Praud, *et al.* [41]. Fig. 2-5a shows the schematic of a dislocation detachment event at one particle where the dislocation line overcomes the attraction of the particle and glides forward by the distance of b with the aid of thermal activation. The shaded area depicts the area that the dislocation sweeps through during this process, which is also approximately equal to $2\lambda b$.

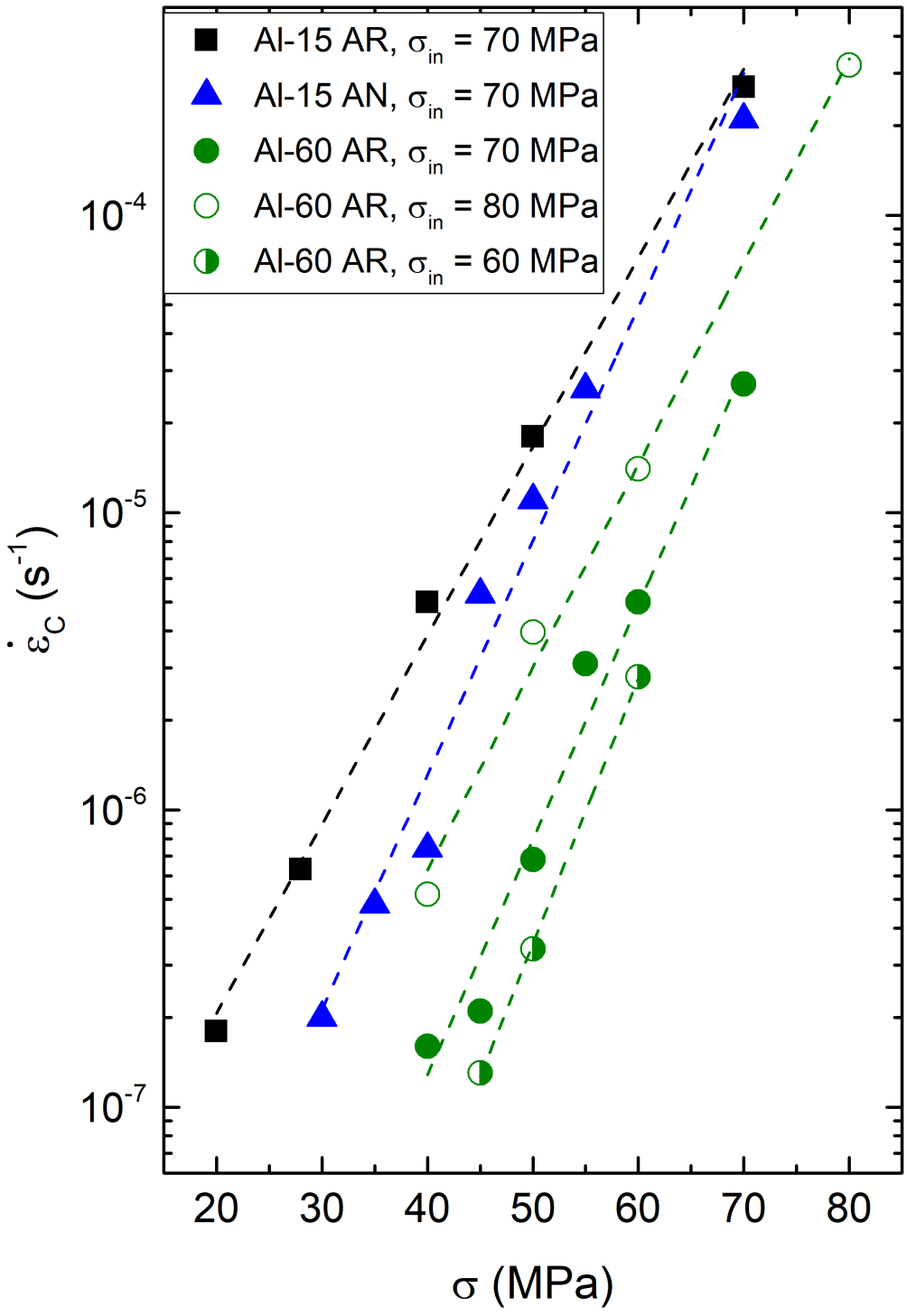

Fig. 2-4 Semilogarithmic plot of constant structure creep rate versus stress for Al-15 AR, Al-15 AN, and Al-60 AR at 973 K. Stress reduction creep tests were performed at an initial stress of 70 MPa for all three materials. For Al-60 AR, these tests were also carried out from 80 and 60 MPa.

Table 2-4 Operational activation areas of dislocation motion for Al-15 AR, Al-15 AN and Al-60 AR measured by constant structure creep tests at 973 K.

Material	σ_{in} (MPa)	M [15]	2λ	Δa"
Al-15 AR	70	2.71	340 b	320 b^2
Al-15 AN	70	2.66	340 b	390 b^2
Al-60 AR	70	2.73	345 b	405 b^2
Al-60 AR	80	2.73	345 b	350 b^2
Al-60 AR	60	2.73	345 b	455 b^2

Apart from dislocation-particle interactions, other possible deformation mechanisms that could control the creep rate for GlidCop include forest dislocation cutting and grain boundary sliding. In cases where creep is controlled by forest dislocation cutting, $\Delta a''$ is roughly equal to the average dislocation spacing l times b, where l can be approximated by $\frac{\alpha M \mu b}{\sigma}$, where α is the Taylor hardening coefficient. Since α can range from 0.3 to 1 for pure copper [42], $\Delta a''$ calculated by this method can range from ~300-1000 b^2, which is either consistent with or greater than the value that what was obtained from the experiments. Therefore, additional evidence is needed to examine the possibility of forest dislocation controlled creep. This discussion is included in the section 4.5, after the athermal flow stress is obtained for GlidCop. Grain boundary sliding also needs to be considered due to the fine grain size of the material [15]. In fact, this mechanism has been identified in another dispersion strengthened material, TD-NiCr [43]. However, the activation area for grain boundary sliding is on the order of 1 b^2 as this mechanism is a diffusional process [44]. Therefore, both of these mechanisms can be excluded because the activation areas do not match the experimentally measured values. It is important to realize that a satisfactory fitting of the RA model to the data alone does not guarantee confirmation of the dislocation detachment mechanism. It could also be somewhat coincidental because the adjustable fitting parameters give much flexibility to enhance the coefficient of

determination. Hence, the activation area analysis described here is crucial because it verifies the physical basis of the dislocation detachment model.

2.4.3.2 Dislocation/dislocation Interactions

In **Table 2-4**, it is evident that $\Delta a''$ also decreases with increasing σ_{in}, as shown by Al-60 AR tested at different σ_{in}. A possible reason is that the inter-dislocation forces that could contribute to $\dot{\epsilon}_C$ are related to σ_{in}. The RA model only counts the critical dislocations on the departure side of the particles and ignores all the other dislocations that form a fairly complicated substructure in GlidCop as described by Broyles, Zhang and Gibeling [15]. Even though most of these "background" dislocations reside in the subgrain boundaries and have little direct effect, the dislocations near the particles can interact with the critical dislocations and contribute to the creep rate. As noted earlier, the detaching dislocations are subject to a forward internal stress generated by the dislocations behind them (that is, on the approach side of the particles) as represented schematically in Fig. 2-5b. This is a natural consequence from the fact that the dislocations spend the greatest time waiting for the detachment process, and glide between the particles is considered to be much faster. Confirmation of this perspective was provided directly by Jansen and Dunand in a Al_2O_3 strengthened Al alloy [45] and Liu and Cowley in a Re strengthened W alloy [46]. Another supporting point is that $\dot{\epsilon}_C$ at a given reduced stress was observed to increase with increasing σ_{in} as shown in Fig. 2-4 for Al-60 AR, which can be explained by the fact that a higher ρ, and more particularly more dislocations between the particles resulting from a higher σ_{in}, can exert a higher forward stress on the detaching dislocation. Unfortunately, the magnitude of the forward stress *per se* cannot be modeled because it is very difficult to calculate the number of dislocations between the particles.

However, this value can be derived by combining the steady-state and the constant structure creep data as discussed in the next section.

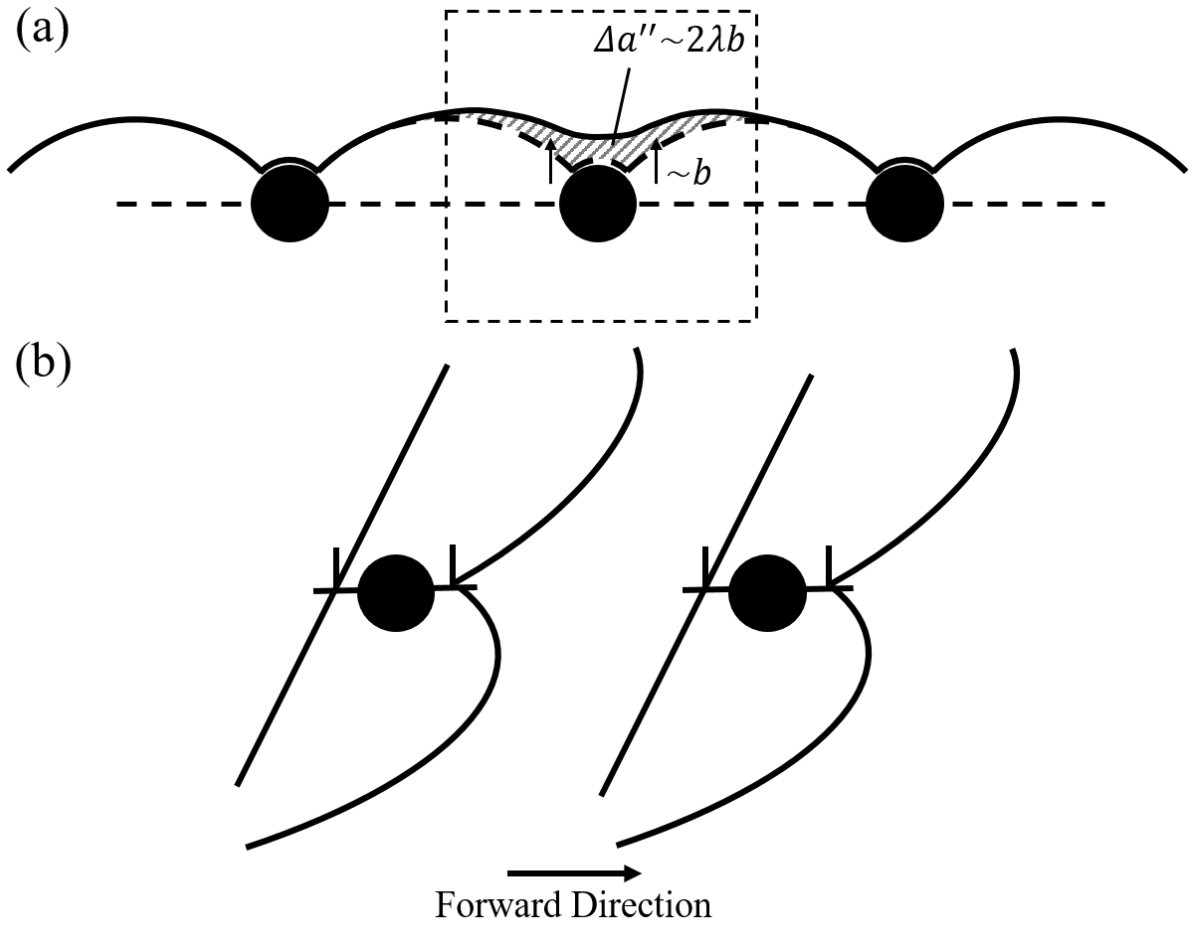

Fig. 2-5 Schematic illustration of dislocations interacting with particles: (a) a single thermal activation event where a segment of the dislocation line detaches from a particle and glides forward by a distance b (exaggerated on the schematic for display purposes). The shaded area delineates the activation area of this event; (b) a quasi-equilibrium condition for dislocations under stress: the dislocations on the approach side of the particle exert a forward stress on the dislocations on the departure side.

2.4.4 Modified RA Model for the Creep Behavior of ODS Alloys

Based on the discussion above, a modified RA model that combines the thermally activated dislocation glide model and the dislocation detachment model is proposed. As a starting point, we write the equivalent of Eqn. 2.1 as:

$$\dot{\epsilon} = \frac{6D_v \lambda \rho_D(\sigma)}{Mb} exp\left(-\frac{\Delta G_D}{k_B T}\right) \tag{2.8}$$

where ΔG_D is the Gibbs free energy of activation for the detachment process and $\rho_D(\sigma)$ is the stress dependent density of dislocations on the departure side of the particles only, which should be much smaller than the total dislocation density ρ_{tot}. Unlike the RA model that assumes ρ_D is constant, our new model considers the stress dependence of ρ_D. Several researchers, including Lloyd and Martin who studied single crystal ODS-Cu, report a squared dependence of the dislocation density on the applied stress for dispersion strengthened alloys [47-49]. Here, as a first approximation, we assume ρ_D shares the same dependence:

$$\rho_D(\sigma) = f_D\left(\frac{\sigma}{M\alpha\mu b}\right)^2 \tag{2.9}$$

where f_D is a dimensionless constant that describes the fraction ρ_D/ρ_{tot}, and here we take α as unity. We note that it is very difficult to model or measure ρ_D directly so that f_D can only be obtained by fitting the experimental creep data. ΔG_D in Eqn. 2.8 can be further expanded by Eqn. 2.7 as long as the parameters p and q are determined. Even though the assumption of $p = q = 1$ was made when determining $\Delta a''$, here we assign $p = 1$, $q = 3/2$ to be consistent with the RA model for further comparison. These values are also validated by Kocks, *et al.* [16] for strong obstacles such as dispersoids. Furthermore, since the inter-dislocation forces create an effective

forward stress as noted in the previous section, the applied stress needs to be modified with an extra positive term σ_s to account for this effect. Therefore, Eqn. 2.7 can be rewritten as:

$$\Delta G_D = \Delta F_D \left(1 - \frac{\sigma + \sigma_s}{\hat{\sigma}}\right)^{3/2} \tag{2.10}$$

By combining Eqns. 2.8, 2.9 and 2.10, we obtain the essential equation of the model:

$$\dot{\epsilon} = \frac{6 D_v \lambda f_D}{M \alpha^2 b^3} \left(\frac{\sigma}{M\mu}\right)^2 exp\left[-\frac{\Delta F_D}{k_B T}\left(1 - \frac{\sigma + \sigma_s}{\hat{\sigma}}\right)^{3/2}\right] \tag{2.11}$$

We note that σ_s should not appear in the pre-exponential stress term because ρ_D is not influenced by σ_s. At constant structure after a stress reduction, ρ_D developed by σ_{in} is retained in the term related to dislocation density whereas the reduced stress is needed to describe the glide kinetics:

$$\dot{\epsilon}_C = \frac{6 D_v \lambda f_D}{M \alpha^2 b^3} \left(\frac{\sigma_{in}}{M\mu}\right)^2 exp\left[-\frac{\Delta F_D}{k_B T}\left(1 - \frac{\sigma_{red} + \sigma_s}{\hat{\sigma}}\right)^{3/2}\right] \tag{2.12}$$

At the subsequent steady state, ρ_D reduces to a value that corresponds to σ_{red}:

$$\dot{\epsilon}_D = \frac{6 D_v \lambda f_D}{M \alpha^2 b^3} \left(\frac{\sigma_{red}}{M\mu}\right)^2 exp\left[-\frac{\Delta F_D}{k_B T}\left(1 - \frac{\sigma_{red} + \sigma_s}{\hat{\sigma}}\right)^{3/2}\right] \tag{2.13}$$

From one series of stress reduction tests that starts from the same σ_{in} with varying σ_{red}, the stress exponent for constant structure creep $n_C = \frac{\partial ln \dot{\epsilon}_C}{\partial ln \sigma_{red}}$ should be less than that for steady-state creep n_{app} by 2 (i.e. n_{app} - n_C = 2) because an extra ${\sigma_{red}}^2$ dependence is present for $\dot{\epsilon}_D$. Therefore, σ_s is determined as the stress which is required to ensure this equality holds. The values of σ_s are listed in **Table 2-5**, and it is clear that for Al-60 AR, σ_s increases with increasing

σ_{in} because the number of dislocations that form the pile-up scales with the applied stress. Fig. 2-6 shows the $\dot{\epsilon}_C$ data for Al-60 AR with different initial stresses plotted with regard to the effective stress $\sigma + \sigma_s$, and illustrates that the data collapse satisfactorily onto a single line, indicating a good representation of the effects caused by inter-dislocation interactions.

ΔF_D and $\hat{\sigma}$ can be determined by taking the derivative of Eqn. 2.12 on a logarithmic basis and squaring:

$$\left(\frac{dln\dot{\epsilon}_C}{d\sigma_{red}}\right)^2 = \left(-\frac{3\Delta F_D}{2k_BT}\right)^2 \left(\frac{1}{\hat{\sigma}}\right)^2 \left(1 - \frac{\sigma_{red} + \sigma_s}{\hat{\sigma}}\right) \tag{2.14}$$

By performing a linear regression of the reduced stress and the squared derivative of the logarithmic strain rate with respect to the reduced stress, ΔF_D and $\hat{\sigma}$ can be obtained from the slope and intercept, and ΔG_D can then be calculated by Eqn. 2.10. The values for σ_s, ΔF_D, ΔG_D and $\hat{\sigma}$ are listed in **Table 2-5**.

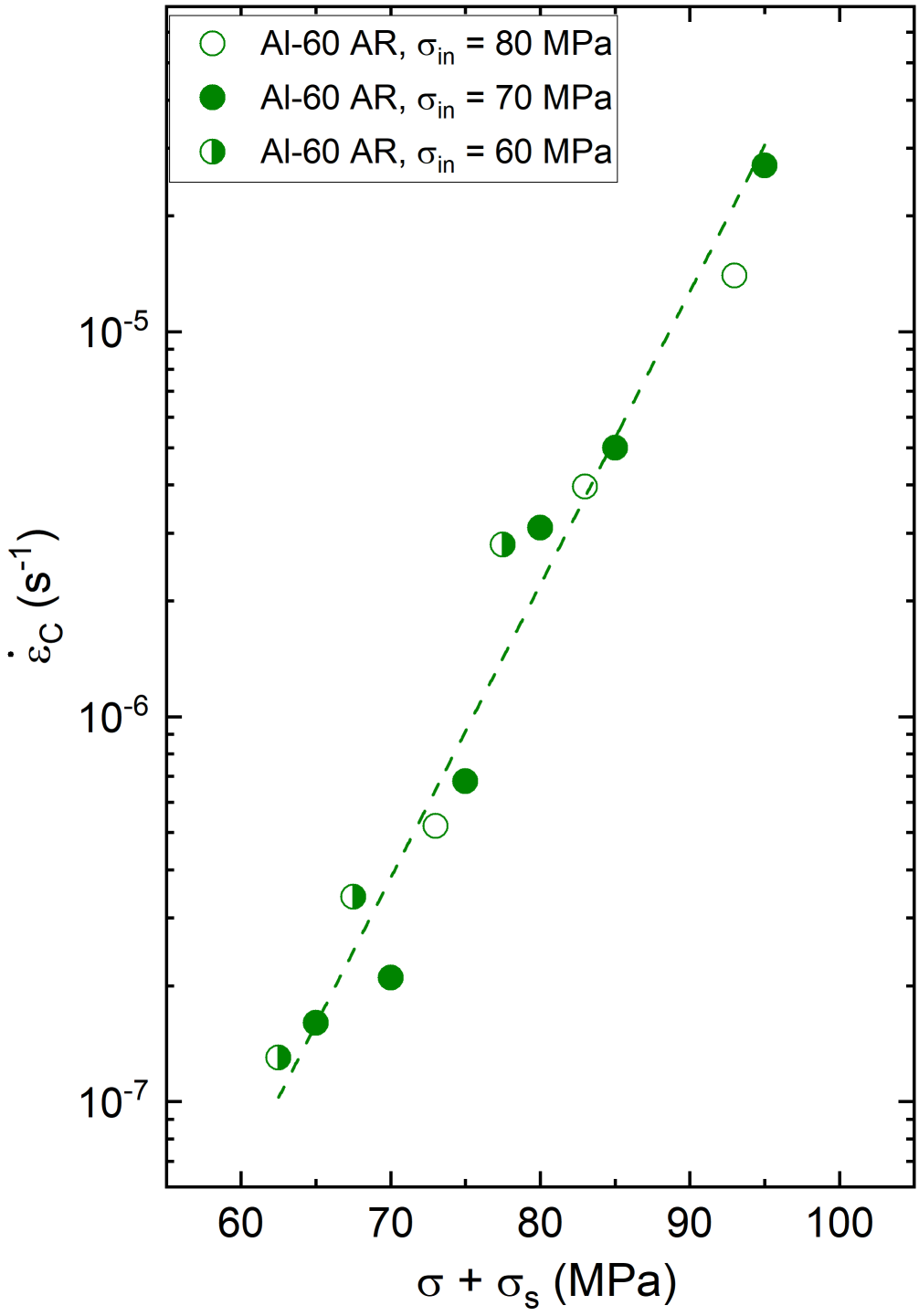

Fig. 2-6 Semilogarithmic plot of the constant-structure creep rate versus the effective stress for Al-60 AR at 973 K from the initial stresses at 80, 70 and 60 MPa.

Table 2-5 Modified RA model parameters of GlidCop Al-15 AR, Al-15 AN and Al-60 AR with microstructures developed at different σ_{in}

Material	σ_{in} (MPa)	σ_s (MPa)	$\hat{\sigma}$ (MPa)	ΔF_D (kJ/mol)	ΔG_D (kJ/mol)
Al-15 AR	70	18	103.4	130.2	7.2
Al-15 AN	70	22	110.0	184.9	12.2
Al-60 AR	70	25			57.4
Al-60 AR	80	33	165.2*	207.6*	36.7
Al-60 AR	60	17.5			80.2

* The σ_{in} dependence of creep microstructure was eliminated by using $\sigma + \sigma_s$ as the applied stress in data analysis. However, ΔG_D is still directly stress dependent (Eqn. 2.10) so three values were obtained corresponding to the three σ_{in} values.

The true threshold behavior observed in the steady-state creep rates for ODS-Cu has not been properly addressed in the RA model. In fact, as shown in Fig. 2-1, the RA model fit deviates from the experimental data and exhibits an opposite trend. As was discussed previously [15], when the applied stress is fairly small, one cannot make the assumption that once a dislocation has detached from a particle it will move to the departure side of the next particle instantaneously. In an extreme case, the RA model predicts finite strain rate under zero applied stress because the dislocations detaching from particles purely by thermal activation (unlikely but not impossible) contribute to plastic strain. Here we propose further modifications to the model to rationalize the threshold behavior of ODS alloys by its physical origin.

It is important to realize that back jumps of detached dislocations cannot be ignored when particles with attractive interfaces are present in the backward direction of dislocation motion even if a modest forward stress is applied. It has been argued that considering back jumps in a thermally-activated dislocation glide model and using a hyperbolic sine function to describe the plastic strain rate is not appropriate because after a dislocation overcomes an obstacle, it will

travel to the next obstacle in a very short time with the aid of the applied stress so that it virtually has no time to jump back, leading to an ignorable back jump rate. Indeed, this argument is true for pure metals and solid solution alloys that have forest dislocations and solute atoms as their rate-controlling obstacles where back jumps are energetically unfavorable because the dislocation would need to overcome the obstacle again in the reverse direction (i.e. cutting through forest dislocations or solute segregations). However, the situation is different for DS alloys because back jumps are energetically favorable in that the particles generate an attractive field for the dislocations to relax their line energies. Once a back jump occurs and the dislocation is again attached to the departure side of the particle, it needs another relatively long period of time to detach from the particle again. In addition, it is worth noting that the attempt frequencies for forward and back jumps are considered to be equal, or at least not too different, and are normally assumed to be equal to the Debye frequency of the lattice. Therefore, the threshold behavior of ODS alloys can be described by a simple equation with several reasonable assumptions: for simplicity, only the back jumps of the just-detached dislocations one atomic distance away from the particle (i.e. the distance between the dislocation and particle, $x = b$) are considered. The probability of consecutive back jumps is significantly lower in the presence of an applied forward stress, so they are neglected. If a back jump does not occur for a dislocation, it will move on to the next particle at high velocity (as in the RA model). If a back jump occurs, the distance that this dislocation travels in the forward direction is zero. Therefore, the new constitutive equation for creep of ODS alloys must include a second exponential term representing the back jumps and can be written as:

$$\dot{\epsilon}_{SS} = \frac{6D_v\lambda f_D}{M\alpha^2 b^3}\left(\frac{\sigma}{M\mu}\right)^2 \left\{ exp\left[-\frac{\Delta F_D}{k_B T}\left(1-\frac{\sigma+\sigma_s}{\hat{\sigma}}\right)^{3/2}\right] - exp\left[-\frac{\frac{\sigma+\sigma_s}{M} b\Delta a''}{k_B T}\right]\right\} \quad (2.15)$$

where the additional term $\frac{\sigma+\sigma_s}{M} b\Delta a''$ is the work done by the forward stress (which needs to be converted to shear stress when computing work) that now needs to be overcome by the attractive stress to achieve a back jump. The change of line tension caused by the change in line geometry before and after detachment is calculated to be small and thus ignored in the equation.

The dashed line in Fig. 2-7 shows an example of the application of Eqn. 2.15 to GlidCop Al-15 AN, which predicts a threshold stress. However, the result shown in Fig. 2-7 appears to underestimate the measured threshold stress, which indicates that the dislocations still experience an attraction from the particles after the detachment process. This contribution can be considered by assuming there is an attractive force from the particle acting on the dislocation that decays with distance and does work when back jumps take place. Since neither the magnitude of this force nor how this force decays are known explicitly, the work done by the force during back jumps is assumed to be $\zeta \cdot \Delta F_D$, where $\zeta = \zeta(x)$ describes the extent of the decay in the stress field. Since $x = b$ is assumed, ζ becomes a constant and serves as a fitting parameter when analyzing creep data. We also note that $0 \leq \zeta \leq 1$ and when $\zeta = 0$, the dislocation can relax its line energy only when it is attached to the particle, whereas when $\zeta = 1$, the dislocation fully relaxes its line energy even if it is a distance b away from the particle. Hence, Eqn. 2.15 now becomes

$$\dot{\epsilon}_{SS} = \frac{6D_v \lambda f_D}{M\alpha^2 b^3}\left(\frac{\sigma}{M\mu}\right)^2 \left\{ exp\left[-\frac{\Delta F_D}{k_B T}\left(1-\frac{\sigma+\sigma_s}{\hat{\sigma}}\right)^{3/2}\right] - exp\left[-\frac{\frac{\sigma+\sigma_s}{M} b\Delta a'' - \zeta \cdot \Delta F_D}{k_B T}\right]\right\} \quad (2.16)$$

A value of ζ = 0.15 was determined by a nonlinear regression to best describe the steady-state creep data for Al-15 AN, as shown in Fig. 2-7 by the solid line. Finally, Eqn. 2.16 is applied to all three GlidCop alloys and excellent agreement is reached between the experimental data and our new model as shown in Fig. 2-8. ζ was determined to be vanishingly small for Al-15 AR and Al-60 AR, suggesting almost no attraction once dislocations have detached from the particle in these two cases. This result suggest that the transformation of Al_2O_3 particles to $9Al_2O_3$-B_2O_3 after annealing extruded GlidCop Al-15 leads to a longer-range attraction on the detached dislocations. Generally, the attraction between the particles and the dislocations appears to be very short-ranged because a small value of ζ is determined even when the distance is as small as b.

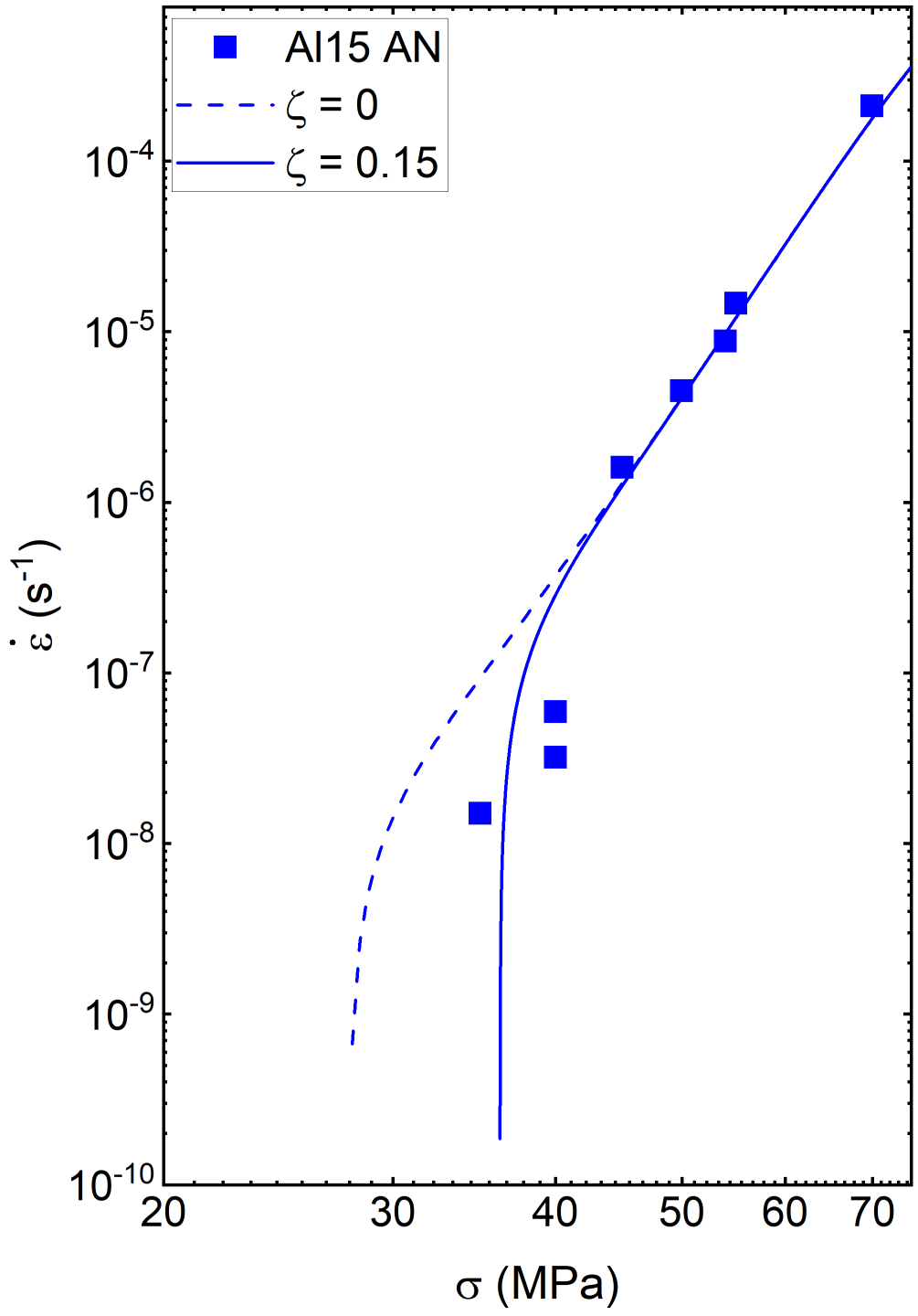

Fig. 2-7 Double Logarithmic plot of steady-state creep rate versus true applied stress for GlidCop Al-15 AN without ζ or an optimized ζ of 0.15.

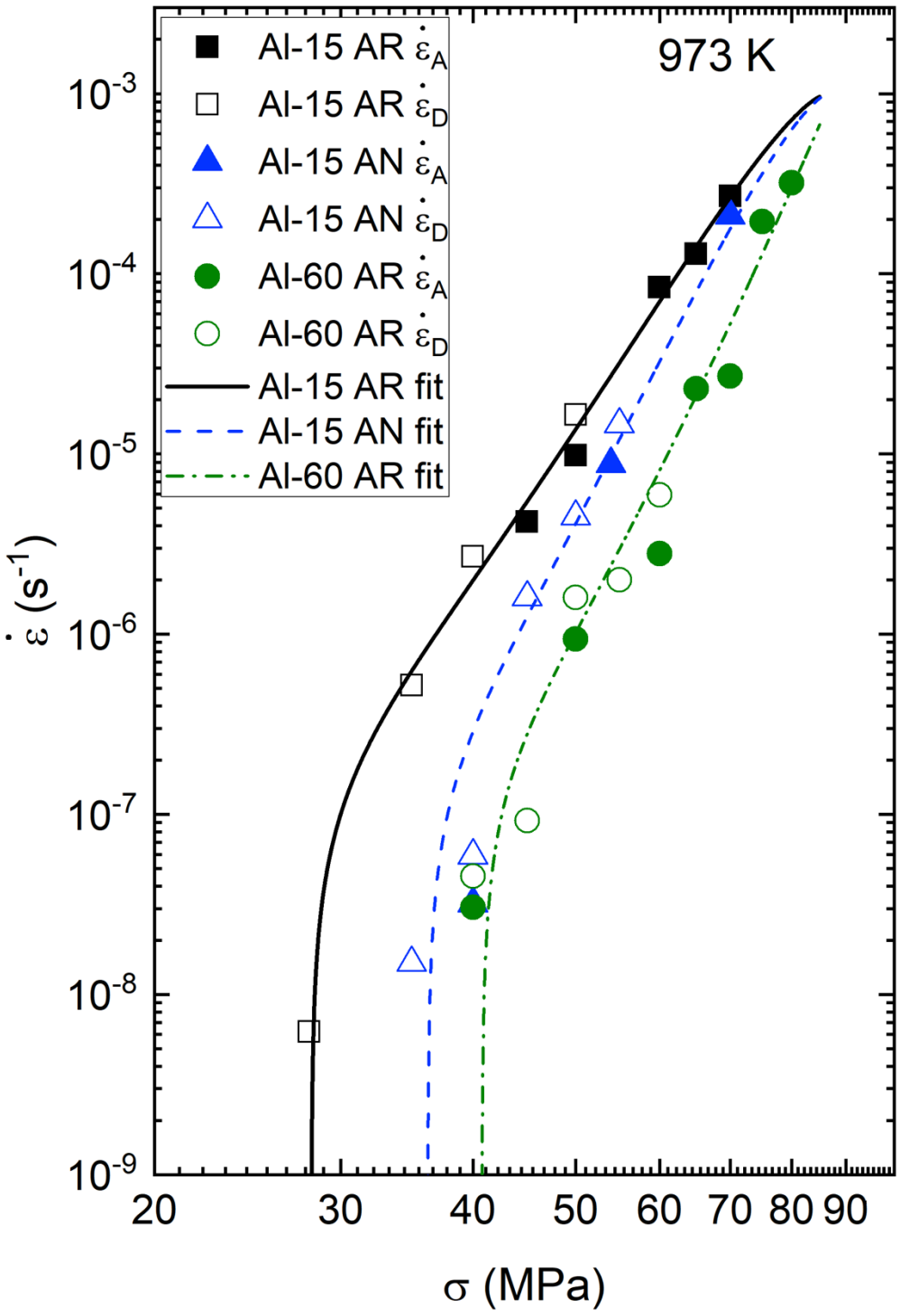

Fig. 2-8 Double Logarithmic plot of steady-state creep rate versus true applied stress for GlidCop Al-15 AR (ζ = 0), Al-15 AN (ζ = 0.15) and Al-60 AR (ζ = 0) with the modified RA model.

2.4.5 Implications of the Modified RA Model

The new model serves to enhance the dislocation detachment description of creep in dispersion strengthened metals because it includes the data from constant-structure creep tests that are independent from those obtained in steady state. The extent of dislocation-particle and dislocation-dislocation interactions can be quantitatively described by ΔF_D, $\hat{\sigma}$ and σ_s. By comparing Eqns. 2.1 and 2.11, it is evident that the new model and the RA model have very similar form because they both start from the thermal activation framework. For instance, ΔG_D in the new model plays an equivalent role as the activation energy for creep deformation in the RA model, $E_d = \mu b^2 r(1-k)^{3/2}\left(1-\frac{\sigma+\sigma_s}{\sigma_D}\right)^{3/2}$ (the original forward stress σ is modified here to be $\sigma + \sigma_s$). In addition, the relaxation parameter, k, can now be related to ΔF by:

$$k = 1 - \left(\frac{\Delta F_D}{\mu b^2 r}\right)^{2/3} \tag{2.17}$$

This provides an improved way to approach k so that Eqns. 2.2 and 2.4 are not the only means to determine this parameter. In fact, the traditional method of calculating k has the shortcoming that the determination of the apparent activation energy is typically subject to a large amount of error because it is both stress and temperature dependent [50-53]. By adopting our new technique, constant structure and temperature are maintained during the tests to accurately determine the activation energies and areas. This enables us to avoid using the less-reliable quantities described above.

Table 2-6 Comparison of model parameters between the modified RA model and the RA model. ΔG_D in the modified RA model and E_d in the RA model are based on a common initial stress of 70 MPa. All parameters related to the RA model are annotated (RA) for easier recognition.

Material	k	k (RA)	$\hat{\sigma}$ (MPa)	σ_D (RA) (MPa)	ΔF_D (kJ/mol)	ΔG_D (kJ/mol)	E_d (RA) (kJ/mol)
Al-15 AR	0.922	0.915	103.4	130.5	130.2	7.2	28.0
Al-15 AN	0.902	0.894	110.0	160.3	184.9	12.2	57.9
Al-60 AR	0.933	0.918	165.2	213.3	207.6	57.4	117.0

The determined parameters from our new model are tabulated in **Table 2-6** with a comparison to those obtained by the standard analysis based on the RA model. It appears that the determination of k as outlined by the RA model gives lower values by assuming the effect of dislocation density on the pre-exponential term is negligible. Since the RA model does not account for the forces between dislocations either, it also results in some overestimation of σ_D. The values of ΔG_D obtained in our new model can be regarded as the true activation energy for dislocation detachment in the ODS alloy because they were determined at constant microstructure and temperature, and their stress dependence was also considered (Eqn. 2.10). ΔG_D is highly dependent on the detachment stress and more generally, the deformation microstructure associated with particles and dislocations. Therefore, assuming a constant activation energy for the materials deforming at different stresses and temperatures is not valid. ΔG_D determined in our model is lower than E_d from the RA model because of the overestimation of σ_D in the latter approach. In addition, ΔG_D is a relatively small fraction of ΔF_D, indicating that dislocation detachment is more mechanically controlled than thermally controlled. That is, the work component of ΔF_D is relatively large compared to the thermal component represented by ΔG_D.

To understand the small values of ΔG_D from our new model (and E_d from the original RA model), we note that the pre-exponential factor in both models contains D_v, which implicitly includes an additional activation energy equal to that of vacancy diffusion. In the original RA model [1], D_v was introduced without detailed justification in connection with vacancy absorption when dislocation detachment occurs. It should be emphasized that the rate-controlling final detachment of the dislocation from the particle is a glide process instead of a climb process. This view is further supported by other work [8, 54, 55], which modeled final detachment as glide behavior. The incorporation of D_v can be rationalized by noting that at low temperatures, the dislocation will face repulsion from the interface if the shear modulus of the particle is larger than that of the matrix because of the stress concentration at the interface. This extra interaction energy caused by the stress field of the dislocation is especially strong when the dislocation is in the close vicinity of the particle. Srolovitz *et al.* [56] attributed the absence of such repulsion at high temperatures to diffusional relaxation of the interface, and the attraction can be subsequently explained by dislocation core relaxation at the incoherent interface. If the interface has been relaxed by diffusion to equilibrate the stress field of the dislocation, when the dislocation detaches and moves away from the particle, diffusional relaxation must happen again in the opposite sense when the stress field of the dislocation is removed. This energy contribution from the interface is separate from the energy of dislocation core relaxation that needs to be provided by both the applied stress and thermal activation for detachment to occur. Here we follow the RA model and use the activation energy of vacancy diffusion to describe the interface relaxation since the temperature (973 K, or 0.7 T_m) is reasonably high.

The effect of particle size and volume fraction can be examined by comparing the results for Al-15 AR and Al-60 AR. $\hat{\sigma}$, ΔF_D and ΔG_D for Al-60 AR are much larger than for Al-15 AR, indicating that either the particle size or spacing plays an important role in governing the detachment process. Since the particle spacing for the two alloys is almost equal, it can be concluded that a larger particle size in Al-60 AR leads to stronger attraction of the dislocations by the particles. This interpretation can be justified by the fact that the dislocation line length attached to a particle may increase with the particle size, so larger particles require detachment of a longer segment of dislocation. The athermal detachment stress $\hat{\sigma}$ and the total energy associated with this process, ΔF_D, for Al-60 AR are about 1.6 times larger than those for Al-15 AR, which is in good agreement with the proportionality between the particle sizes. The effect of particle type can be evaluated as well by considering the value of k. The difference of k values for the two as-received alloys is small because the nature of the particle/matrix interface is the same despite the difference in curvature. However, k for the annealed Al-15 alloy differs greatly from the as-received Al-15 because the particles transformed to $9Al_2O_3$-$2B_2O_3$ and became more attractive, which was described in our previous paper [15].

It is necessary to compare the results of ODS Cu and pure Cu, both obtained from the thermally activated glide model. The athermal flow stress in pure Cu for stress reductions from 16 MPa was found to be roughly 33 MPa [20]. For ODS Cu, it was found to be 100-165 MPa. Mechanically speaking, the particles present obstacles to glide that are 3-5 times stronger than the forest dislocations that are considered to be the obstacles to glide in pure metals, which explains the superior creep strength gained from the addition of the oxide dispersoids. Therefore, despite the fact that forest dislocation cutting may present a comparable activation area to

detachment from particles in the case of ODS Cu (if α is small), the large difference in the athermal flow stress rules out the possibility of the former mechanism.

Our physics-based model also offers a clear, unified description of the threshold behavior in ODS Cu in a way that is consistent with the concept of dislocation detachment from particles as the rate-controlling mechanism. Even though the introduction of ζ as a fitting parameter makes the model phenomenological to some degree, the creep equation still gives a reasonable prediction of threshold stress even if $\zeta = 0$ as shown in Fig. 2-7 and 2-8. More computation and microscopy work of dislocation-particle interactions is needed in the future to better understand the origin of ζ. The threshold stresses for Al-15 AR, Al-15 AN and Al-60 AR were calculated to be 28 MPa, 36 MPa and 41 MPa, respectively, which are slightly higher than the values determined from the threshold stress model, exhibiting a stiffer transition from the power law regime to the threshold regime.

Finally, it is important to examine the critical dislocation density, ρ_D, that is determined from fitting the creep data. The constant that plays a similar role in the RA model is the fitted dislocation density ρ in Eqn. 2.1. **Table 2-7** shows the comparison between f_D and the resulting ρ_D at an applied stress of 70 MPa in our model and ρ in the RA model. It is evident that ρ_D is 100 to 10,000 times smaller than ρ_{tot}, which suggests that the dislocation density derived from our model is not overly high. It also supports our earlier statement that most of the dislocations form subgrains and networks that are immobile, and only a small fraction of dislocations that interact with particles control the creep rate. However, it is still hard to imagine ρ_D is 100 times higher for Al-60 AR than Al-15 AR even though this difference between the two materials is smaller than the factor of 10^4 in the RA model. f_D or ρ_D most likely includes some inaccuracy of

the model due to an inadequate description of the stress dependence of ΔF_D, ΔG_D, and $\hat{\sigma}$. Strictly speaking, ΔF_D, ΔG_D, and $\hat{\sigma}$ obtained in this study are only accurate for the stresses shown in **Table 2-5** where stress reduction tests were carried out. The extrapolation of these values to all stresses tested in steady state inevitably causes error, especially when they are in the exponential term. Therefore, although challenging, stress reduction creep experiments at all test stresses are necessary in order to obtain a fully accurate description of steady-state creep. In addition, the effect of dynamic recovery has not been considered in this study, which can be a limitation of the model at large stress reductions. Such effect can be studied in the future by performing near total stress reductions (i.e. ~100% stress reductions), but is beyond the scope of the current paper.

Table 2-7 Comparison between the fitting constants f_D and resulting ρ_D at an applied stress of 70 MPa in our model and ρ in the RA model.

Material	f_D	ρ_D (m^{-2})	ρ (RA) (m^{-2})
Al-15 AR	3.2×10^{-4}	3.3×10^{9}	5.0×10^{11}
Al-15 AN	3.0×10^{-4}	3.2×10^{9}	6.6×10^{13}
Al-60 AR	3.2×10^{-2}	3.2×10^{11}	4.2×10^{15}

2.5 Conclusions

(1) Stress reduction transient creep experiments were used to explore the high temperature deformation of GlidCop Al-15 and Al-60, two dispersion strengthened copper alloys containing Al_2O_3 dispersoids. The transients following stress reductions exhibit a form that is similar to that observed for solid solution alloys, whereas the initial primary creep follows a form similar to that for pure metals. These results cannot be described by existing models for creep of dispersion strengthened alloys.

(2) An improved creep model has been formulated to describe the thermally activated detachment-controlled creep of dispersion-strengthened copper alloys and to predict a threshold stress. This model relies on data obtained from both steady state and constant structure (stress reduction) creep tests on extruded and annealed GlidCop Al-15 as well as extruded GlidCop Al-60 to determine the necessary parameters, thereby improving the accuracy of the predictions compared to the Rösler-Arzt model.

(3) The new model serves as a modification to the Rösler-Arzt model in that it takes into account the forces between the critical detaching dislocation and nearby dislocations. These forces are resolved into an effective forward stress that can be determined from the creep experiments. This modification is necessary to describe both the steady state and constant structure creep response following stress reductions. Unlike the original Rösler-Arzt model, the new model does not require an overly high mobile dislocation density to describe the data for GlidCop Al-15 and Al-60.

(4) This paper describes a robust way of measuring the operational activation area for dislocation glide under constant temperature and structure on a custom modified creep machine with excellent strain and time resolution. The operational activation areas for GlidCop obtained in this study are consistent with the value of $2\lambda b$, where 2λ is the interparticle spacing, thereby providing strong evidence that the rate-controlling deformation mechanism is indeed dislocations detaching from particles.

(5) The observation of a true threshold stress for creep in dispersion-strengthened materials is rationalized by the occurrence of thermodynamic back jumps of as-detached dislocations due to the attractive force emanating from the particle/matrix interface. The operational activation area is again used to compute the activation energy of back jumps (in which a dislocation moves back against the work done by the forward stress). When included in the thermally activated detachment model, this additional term leads to an accurate prediction of the threshold stress.

References

[1] J. Rösler, E. Arzt, Acta Metall. Mater. 38(4) (1990) 671-683.
[2] O.D. Sherby, P.M. Burke, Prog. Mater. Sci. 13 (1968) 323-390.
[3] J. Rösler, R. Joos, E. Arzt, Metall. Mater. Trans. A 23(5) (1992) 1521-1539.
[4] C. Zakine, C. Prioul, D. François, Creep behaviour of ODS steels, Mater. Sci. Eng., A 219(1) (1996) 102-108.
[5] S.E. Broyles, K.R. Anderson, J.R. Groza, J.C. Gibeling, Metall. Mater. Trans. A 27(5) (1996) 1217-1227.
[6] L. Shi, D.O. Northwood, J. Mater. Eng. Perform. 4(2) (1995) 196-211.
[7] M.W. Decker, J.R. Groza, J.C. Gibeling, Mater. Sci. Eng., A 369 (1-2) (2004) 101-111.
[8] A. Orlová, J. Čadek, Acta Metall. Mater. 40(8) (1992) 1865-1871.
[9] M. Heilmaier, H. Kestler, J.C. Gibeling, Zeitschrift für Metallkunde 93(7) (2002) 666-671.
[10] J.C. Gibeling, Interpretation of threshold stresses and obstacle strengths in creep of particle-strengthened materials, in: R.S. Mishra, A.K. Mukherjee, K.L. Murty (Eds.) Creep Behavior of Advanced Materials for the 21st Century, The Minerals, Metals & Materials Society, San Diego, CA, 1999, pp. 239-253.
[11] J.J. Stephens, R.J. Bourcier, F.J. Vigil, D.T. Schmale, Report No. SAND88-1351, Sandia National Laboratories, Albuquerque, NM, 1988.
[12] F. Ernst, P. Pirouz, A.H. Heuer, Phil. Mag. A 63(259-277) (1991).
[13] J.J. Stephens, J.A. Romero, C.R. Hills, Microsc. Sci. 16 (1988) 245-265.
[14] J. Groza, S. Farrens, Microsc. Sci. 19 (1992) 689-699.
[15] S.E. Broyles, M. Zhang, J.C. Gibeling Mater. Sci. and Eng. A 779 (2020) 139112.
[16] U.F. Kocks, A.S. Argon, M.F. Ashby, Prog. in Mater. Sci. 19 (1975) 1-281.
[17] M.J. Mills, J.C. Gibeling, W.D. Nix, Acta Metall. Mater. 33(8) (1985) 1503-1514.
[18] M. Biberger, J.C. Gibeling, Acta Metall. Mater. 43(9) (1995) 3247-3260.
[19] G.S. Nakayama, J.C. Gibeling, Acta Metall. Mater. 38(10) (1990) 2023-2030.
[20] S.E. Broyles, J.C. Gibeling, Scr. Metall. Mater. 33(5) (1995) 767-772.

[21] W. Blum, J. Hausselt, G. Konig, Acta Metall. Mater. 24(4) (1976) 293-297.
[22] M.Z. Butt, Philos. Mag. 87(24) (2007) 3595-3614.
[23] B.J. Diak, S. Saimoto, Mater. Sci. Eng., A 234-236 (1997) 1019-1022.
[24] Z.S. Basinski, Philos. Mag. 4(40) (1959) 393-432.
[25] E.N.D.C. Andrade, B. Chalmers, Proc. R. Soc. Lond. A 138(835) (1932) 348-374.
[26] J.C. Gibeling, W.D. Nix, Acta Metal. Mater. 29(10) (1981) 1769-1784.
[27] H.J. Frost, M.F. Ashby, Deformation Mechanism Maps: the Plasticity and Creep of Metals and Ceramics, Pergamon Press, Oxford, 1982, p. 166.
[28] J.C. Gibeling, Acta Metall. Mater. 37(12) (1989) 3183-3193.
[29] W. Blum, Mater. Sci. Eng., A 319-321 (2001) 8-15.
[30] J. Robles, K.R. Anderson, J.R. Groza, J.C. Gibeling, Metall. Mater. Trans. A 25(10) (1994) 2235-2245.
[31] J.C. Gibeling, W.D. Nix, Anomalous and constant structure creep transients in pure aluminum, in: R.C. Gifkins (Ed.) Proceedings of the 6th International Conference on the Strength of Metals and Alloys, Melbourne, Australia, 1982, pp. 16-20.
[32] W. Blum, S. Vogler, M. Biberger, A.K. Mukherjee, Mater. Sci. Eng., A 112 (1989) 93-106.
[33] Z. Sun, S. Van Petegem, A. Cervellino, W. Blum, H. Van Swygenhoven, Acta Mater. 119 (2016) 104-114.
[34] P. Yavari, T.G. Langdon, Acta Metall. Mater. 30(12) (1982) 2181-2196.
[35] C.N. Ahlquist, W.D. Nix, Acta Metall. Mater. 19(4) (1971) 373-385.
[36] R. Horiuchi, M. Otsuka, Trans. Jpn. Inst. Met. 13(4) (1972) 284-293.
[37] G.S. Nakayama, J.C. Gibeling, Modeling the Deformation of Crystalline Solids (1991) 589-600.
[38] W.F. Hosford, The Mechanics of Crystals and Textured Polycrystals, Oxford University Press, New York, 1993, pp. 75-81.
[39] S.E. Broyles, Ph.D. Dissertation, University of California, Davis (1995) 115.
[40] M.S. Nagorka, G.E. Lucas, C.G. Levi, Metall. Mater. Trans. A 26(4) (1995) 873-881.
[41] M. Praud, F. Mompiou, J. Malaplate, D. Caillard, J. Garnier, A. Steckmeyer, B. Fournier, J. Nucl. Mater. 428(1) (2012) 90-97.
[42] F.F. Lavrentev, Mater. Sci. Eng. 46(2) (1980) 191-208.
[43] R.D. Kane, L.J. Ebert, Metall. Mater. Trans. A 7(1) (1976) 133-137.
[44] Y.M. Wang, A.V. Hamza, E. Ma, Acta Mater. 54(10) (2006) 2715-2726.
[45] A.M. Jansen, D.C. Dunand, Acta Mater. 45(11) (1997) 4583-4592.
[46] M. Liu, J. Cowley, Scr. Metall. Mater. 28(3) (1993) 307-312.
[47] G.J. Lloyd, J.W. Martin, Mater. Sci. Eng. 46(1) (1980) 1-13.
[48] R.A. Stevens, P.E.J. Flewitt, Acta Metall. Mater. 29(5) (1981) 867-882.
[49] A.J.E. Foreman, M.J. Makin, Can. J. Phys. 45(2) (1967) 511-517.
[50] F. Dobeš, Scr. Metall. Mater. 27(10) (1992) 1435-1438.
[51] C.R. Barrett, O.D. Sherby, Trans. Metall. Soc. AIME 230(6) (1964) 1322-1327.
[52] S.V. Raj, T.G. Langdon, Acta Metall. Mater. 37(3) (1989) 843-852.
[53] M. Pahutová, J. Čadek, P. Ryš, Philos. Mag. 23(183) (1971) 509-517.
[54] B. Reppich, Acta Mater. 46(1) (1998) 61-67.
[55] W. Blum, B. Reppich, Creep of particle-strengthened alloys, Pineridge Press Ltd., Creep Behaviour of Crystalline Solids (1985) 83-135.

[56] D.J. Srolovitz, R.A. Petkovic-luton, M.J. Litton, Philos.Mag. A 48(5) (1983) 795-809.

Chapter 3 Understanding Creep Mechanisms of a Cu-Cr-Nb Alloy by Testing under Constant Structure Conditions[1]

3.1 Introduction

Development of creep resistant, high thermal conductivity alloys is crucial for actively cooled combustion chambers and nozzle liners on next generation space vehicles [1]. One candidate for such applications is Cu-8 at.%Cr-4 at.%Nb (GRCop-84), with ~14 vol% Cr_2Nb particles that enhance the creep strength of Cu. These particles are dispersed in a nearly pure Cu matrix so high thermal conductivity is retained [2].

Creep properties of GRCop-84 have been explored in previous studies [2-6], where phenomenological equations were provided to describe the steady-state creep rates. However, detailed understanding of its elevated temperature deformation mechanisms remains unsatisfactory. For example, the above studies concluded that the power-law model gives high stress exponents and activation energies that are hard to rationalize, and the Rösler-Arzt model of dislocation detachment from particles does not apply. Vettraino, *et al.* [7] discovered a bimodal distribution of particle sizes (averages of ~50 nm and ~230 nm), and concluded that the rate-determining mechanism is likely to be dislocations locally climbing over the smaller particles. However, this conclusion was only based on the fact that the climb resistance calculated from the observed threshold stress falls in the range for local climb derived from simplified models [8]. One challenge is that parameters derived from steady-state data alone are typically inadequate to

[1]Published as M. Zhang, J.C. Gibeling, *Scr. Mater*. **190** (2021) 131-135

describe the rate-controlling processes. Steady states across different stresses and temperaturecorrespond to different microstructures, the influence of which on creep rates and activation energies is often not treated with sufficient detail. Therefore, it is desirable to include creep data acquired at constant structure and temperature, where a change in rate is only a function of a change in stress. This condition is realized by conducting stress reduction tests, where the strain response to a decrease in stress is recorded within a short time during which the microstructure is assumed to be invariant. Constant-structure creep tests have been validated in previous creep studies of pure metals, solid solutions, and dispersion strengthened alloys [9-14].

The present study aims to provide a better understanding of kinetics of dislocation motion in GRCop-84 by presenting the results from constant-structure creep tests at 923 K and deriving the activation energy and the microstructural strength. A constitutive creep equation based on these parameters is developed to describe creep of GRCop-84.

3.2 Experimental

GRCop-84 was produced by argon gas atomization, extrusion, and rolling. The rolled sheets were then electrical discharge machined into flat specimens with a gauge section of 20.32(L) × 2.54(W) × 0.635(H) mm. A detailed description of the fabrication process and microstructure prior to testing is given in Refs. [3, 7], where this material is identified as GRCop-84 production sheet. Samples were hand polished using 400 and 600 grit SiC abrasives to minimize surface effects on the creep properties.

Tests were conducted in a constant-stress creep machine operating under vacuum ($\leq 2 \times 10^{-5}$ torr) following procedures described in previous studies [11, 12, 14]. The notation of stresses and strains at different creep stages follows that of Biberger and Gibeling [10]: specimens were loaded at constant initial stress, σ_{in}, to a steady state creep rate, $\dot{\epsilon}_A$, after which part of the load was rapidly removed. The instantaneous creep strain following the stress reduction, $\dot{\epsilon}_C$, was acquired at 10 Hz with a time resolution of 1 μs. The reduced stress, σ_{red}, was maintained until the second steady state creep rate, $\dot{\epsilon}_D$. The stress levels are listed in **Table 3-1.**

Table 3-1 Initial and reduced stresses used in the constant-structure creep tests on GRCop-84 at 923 K. Each creep sample was only subject to one stress reduction.

σ_{in} (MPa)	σ_{red} (MPa)
95	75, 65, 60, 55, 50
80	65, 60, 55, 50, 40
65	60, 55, 50, 40

Samples were furnace cooled under stress to preserve the dislocation substructure for electron microscopy. Transmission electron microscopy was performed using a Philips CM12 to examine dislocation substructure and possible dislocation-particle interactions. Sample preparation methods are given in Ref. [7].

3.3 Results and Discussion

Fig. 3-1a shows example creep curves for GRCop-84 at 923 K. Stress reductions from initial stresses of 95 and 80 MPa were initiated at a strain of ~9%, whereas those from an initial stress of 65 MPa occurred at ~5% strain to avoid reaching tertiary creep before the reduction. As reported in our previous paper [3], all curves exhibit normal primary creep, where the rates

decelerate to steady state. This effect is explained by decreasing mobile dislocation density due to formation and refinement of subgrains (illustrated in Ref. [7]) and dislocation pinning by particles. The same behavior was observed in a dispersion strengthened copper alloy, GlidCop ($Cu\text{-}Al_2O_3$), which has a similar microstructure despite having smaller particles [14].

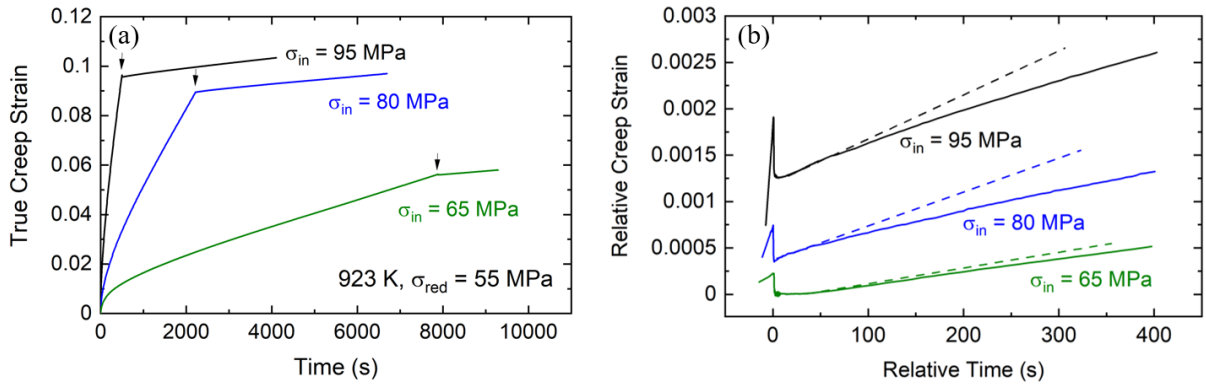

Fig. 3-1(a) Example creep curves for GRCop-84 samples crept at 923 K with an initial stress of 95, 80 and 65 MPa and a reduced stress of 55 MPa. The arrows indicate the onsets of the stress reductions that change the slopes of the curves; (b) an expanded view of the stress reduction transients within (a). The curves were shifted both vertically and horizontally for better comparison, so axes are relative. The dashed lines represent the creep rates of GRCop-84 immediately following the stress reductions, that is, the constant-structure creep rates, $\dot{\epsilon}_C$.

A detailed view of the stress reduction transients is presented in Fig. 3-1b; in all cases the constant-structure creep rates decelerate to the second steady state represented by the dashed lines; thus $\dot{\epsilon}_C > \dot{\epsilon}_D$. The characteristics shown in Fig. 3-1 are representative of all tests (both small and large stress reductions). This so-called "inverted" transient is not unexpected for particle-strengthened alloys. The same trend was observed in GlidCop under similar conditions [4, 14] for which higher $\dot{\epsilon}_C$ compared to $\dot{\epsilon}_D$ was explained by the dislocation detachment mechanism with a high dislocation density corresponding to σ_{in} in the pile-up near the particle exerting a forward stress on the ready-to-detach dislocation. Dislocation density then decreases with strain and the resistance from dislocation-dislocation interaction weakens as $\dot{\epsilon}_C$ decreases to $\dot{\epsilon}_D$. This explanation also applies to GRCop-84 even though deformation is not detachment controlled but is likely to be local climb controlled [3] because blocked dislocations on the approach side of the particles still pile up. Therefore, the nature of the near-particle dislocation-dislocation interactions is similar whether the rate-controlling dislocations are on the approach side or on the departure side of particles.

The constant-structure creep rate can be described by the kinetic law based on thermally activated dislocation motion [15]:

$$\dot{\epsilon}_C = \dot{\epsilon}_0 exp\left[-\frac{\Delta F}{k_B T}\left(1 - \frac{\sigma}{\hat{\sigma}}\right)\right] \tag{3.1}$$

where ΔF is the Helmholtz free energy of activation, k_B is the Boltzmann's constant, T is the temperature, σ is the applied stress, and $\hat{\sigma}$ is the microstructural strength of the rate-controlling obstacle (i.e. the flow stress at 0 K). Eqn. 3.1 was developed for glide-controlled motion, but can

be applied to climb-controlled creep by noting that the infinitesimal energy change dE for local climb depends on dislocation advancement in the glide direction dx and vertical displacement in the local climb direction dy is [8]:

$$dE = T_{el}dl - \tau bldx - \sigma_n bl_c dy - dE_{el} \tag{3.2}$$

where T_{el} is the line tension of the dislocation, dl is the line length increase for local climb, τ is the applied shear stress, b is the Burgers vector, l is the dislocation line length, σ_n is the normal Peach-Koehler component of applied stress, l_c is the dislocation line length that is attached to the particle, and dE_{el} is the change in the elastic interaction energy between the dislocation and the particle. The first term is the energy penalty for dislocation line length increase during local climb, which results in a back stress [16-18]. The second term is the work done by the applied stress to facilitate glide. The third term is the work done by the normal stress component to aid dislocation climb. This term can be neglected for GRCop-84 since $l >> l_c$, because the particle volume fraction is not high enough and the interparticle spacing is much larger than the particle size (530 nm versus 56 nm for small surmountable particles [19]). The last term can also be neglected because the previous Rösler-Arzt analysis of GRCop-84 [4] yields an interfacial relaxation parameter $k > 0.94$, meaning there is only a very weak attraction of the dislocation to the particle/matrix interface. Therefore, Eqn. 3.2 can be shortened to $dE = T_{el}dl - \tau bldx$, and the thermally activated analysis (Eqn. 3.1) can be applied to the local climb process as a one-step dislocation release event whose average time can be captured by the strain rate measured in constant-structure creep tests. Even though local climb consists of multiple steps and could be modeled in greater detail, the effort is unnecessary here because the climb process *per se* provides negligible strain.

The results of the constant-structure creep tests are shown in Fig. 3-2a on a semilogarithmic plot consistent with Eqn. 3.1. The coefficients of determination of all three linear fits are ~0.99, verifying the validity of Eqn. 3.1. High σ_{in} also gives high $\dot{\epsilon}_C$, indicating that the difference in σ_{in} creates a difference in the dislocation substructure prior to stress reduction, which exerts a different internal stress on dislocations.

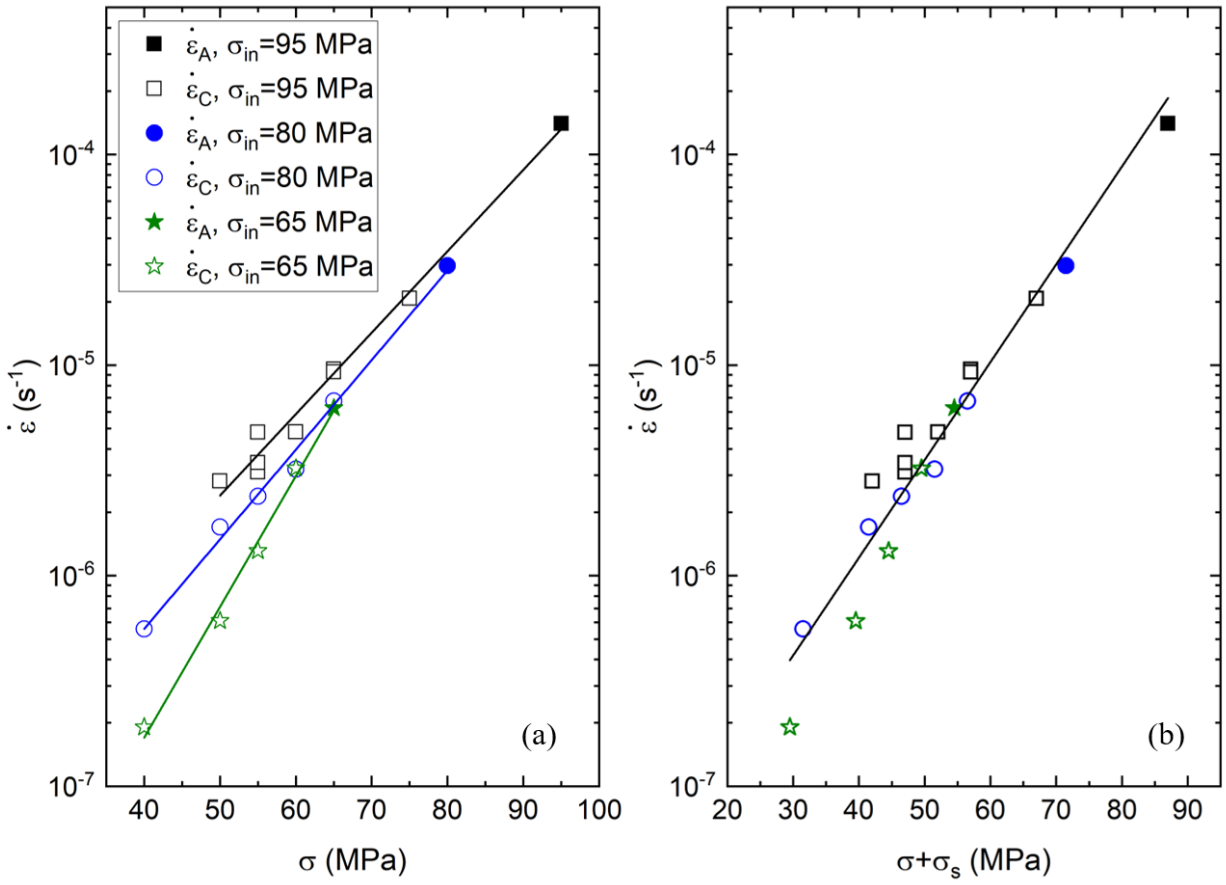

Fig. 3-2 (a) Semilogarithmic plot of constant-structure creep rate ($\dot{\epsilon}_C$) versus the applied stress for GRCop-84 with an initial stress of 95, 80 and 65 MPa. The solid symbols represent the steady state creep rates under the initial stress ($\dot{\epsilon}_A$). Since the microstructure corresponding to $\dot{\epsilon}_C$ is assumed to be identical to that of $\dot{\epsilon}_A$, $\dot{\epsilon}_A$ can be envisaged as a special form of $\dot{\epsilon}_C$ when the reduced stress is equal to the initial stress (i.e. no stress reduction); (b) Semilogarithmic plot of constant-structure creep rate versus the effective stress under the same test conditions as in (a).

Our previous study [14] provides a method to determine the internal stress, σ_s, from steady-state and constant-structure creep data. Assuming a squared stress dependence of mobile dislocation density,

$$\dot{\epsilon}_C = C\left(\frac{\sigma_{in}}{M\mu}\right)^2 exp\left[-\frac{\Delta F}{k_B T}\left(1-\frac{\sigma_{red}+\sigma_s}{\hat{\sigma}}\right)\right] \tag{3.3}$$

$$\dot{\epsilon}_D = C\left(\frac{\sigma_{red}}{M\mu}\right)^2 exp\left[-\frac{\Delta F}{k_B T}\left(1-\frac{\sigma_{red}+\sigma_s}{\hat{\sigma}}\right)\right] \tag{3.4}$$

where C is a constant, M is the Taylor factor, and μ is the shear modulus. The difference between $\dot{\epsilon}_C$ and $\dot{\epsilon}_D$ is associated with different mobile dislocation densities of the substructures corresponding to σ_{in} and σ_{red}. ΔF remains the same because there is no change in the energetics of dislocation-particle interaction before and after the stress reduction. From Eqns. 3.3 and 3.4, the difference between the stress exponents of steady state and constant-structure creep, $n_D - n_C = \frac{\partial ln\dot{\epsilon}_D}{\partial \ln(\sigma_{red}+\sigma_s)} - \frac{\partial ln\dot{\epsilon}_C}{\partial ln(\sigma_{red}+\sigma_s)}$, should take the exact value of 2. Therefore, σ_s can be determined from linear fits of $ln\dot{\epsilon}_C$ and $ln\dot{\epsilon}_D$ versus $\ln(\sigma+\sigma_s)$ with this constraint. The σ_s values are given in **Table 3-2**, and Fig. 3-2a maps to Fig. 3-2b when the applied stress is replaced by the effective stress. Thus, the constant-structure creep data collapse to the same line, which justifies that the σ_{in} dependence of $\dot{\epsilon}_C$ is eliminated by accounting for the appropriate values of σ_s. Two conclusions result: i) σ_s is negative for GRCop-84, which justifies the back stress acting on rate-controlling dislocations mentioned above. Operationally, $\sigma+\sigma_s$ is equivalent to $\sigma-\sigma_B$, where σ_B is the commonly-used (positive) back stress. This observation supports the assertion that the controlling deformation mechanism in GRCop-84 is local climb, because dislocation detachment gives a positive σ_s [14]; ii). σ_s is less negative for high σ_{in},

which supports the hypothesis that a high σ_{in} results in more dislocations in the pile-up, thereby providing a high forward stress and canceling a large part of the back stress. Nonetheless, only a weak dependence of σ_s on σ_{in} is shown, implying that the forward stress created by dislocation pile-ups is small compared to the back stress. Microscopically, local climb is captured by TEM analysis. Arrows in Fig. 3-3 show examples of the dislocations climbing over small particles in a deformed sample. The larger particles (~230 nm) are insurmountable and do not control the rate, which agrees well with the conclusion in Ref. [3].

Table 3-2 Parameters for the constitutive creep equation that describes the constant-structure creep behavior of GRCop-84 (Eqn. 3.3)

σ_{in} (MPa)	σ_s (MPa)	$\hat{\sigma}$ (MPa)	ΔF (kJ/mol)
95	-8	250±2	184.7±0.9
80	-8.5		
65	-10.5		

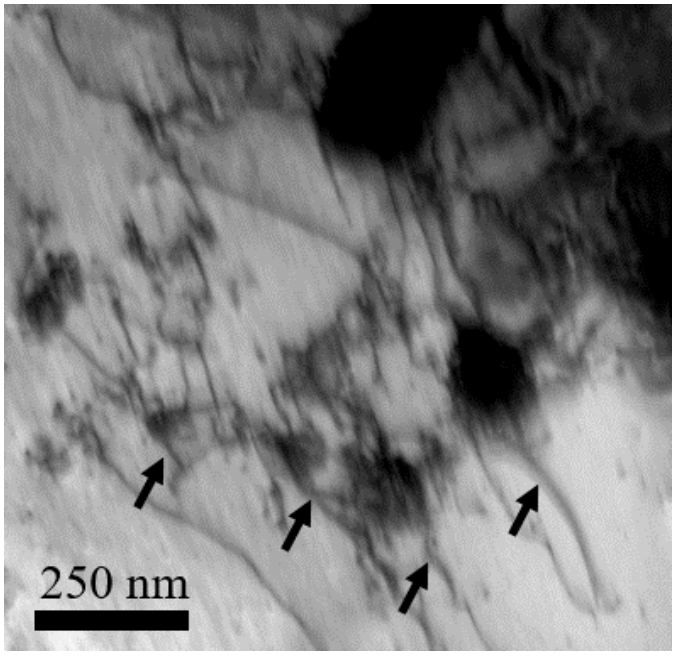

Fig. 3-3 TEM micrograph of GRCop-84 showing dislocation-particle interactions. The arrows identify dislocations that have locally climbed on the particles.

The data in Fig. 3-2b can be utilized to compute $\hat{\sigma}$ and ΔF by a multiple regression after substituting $\sigma + \sigma_s$ for σ in Eqn. 3.1. The values of $\hat{\sigma}$ and ΔF are listed in **Table 3-2**. $\hat{\sigma}$ for GRCop-84 is much higher than that for pure Cu (~33 MPa [12]) and differs from that of GlidCop (~100 MPa for Al-15 and ~160 MPa for Al-60 [14]). This difference agrees with the fact that local climb is mechanically difficult, and a large external stress is needed to provide sufficient climb force to move the dislocation without the aid of thermal activation. In addition, ΔF for GRCop-84 closely resembles the activation energy for self-diffusion in Cu (~197 kJ/mol [20]), further validating the local climb mechanism and indicating that the deformation mechanisms for the two materials are thermodynamically similar. Indeed, creep in pure Cu in the power law region is often considered to be climb controlled [21]. The validity of ΔF and $\hat{\sigma}$ is verified by the fact that both have physically reasonable values, although the small standard error of regression suggests some overfitting due to the relatively small data set.

The thermally activated glide analysis also provides the operational activation area, $\Delta a''$, which describes the length scale of the thermal activation events that control the deformation rate (see Ref. [14] for a more detailed description):

$$\Delta a'' = \frac{M k_B T}{b} \cdot \left. \frac{\partial ln \dot{\epsilon}_C}{\partial \sigma} \right|_{T,\hat{\sigma}} \tag{3.5}$$

Eqn. 3.5 suggests that $\Delta a''$ must be determined at constant temperature and microstructure. Accordingly, values can be determined from the slope of the constant structure data in Fig. 3-2a using Eqn. 3.2, and the result is given in **Table 3-3** along with the size of the Cr_2Nb particles, $2r$, and the interparticle spacing, 2λ. The results demonstrate that $\Delta a''$ is on the same order as $2rb$ for small particles, suggesting localized activation events at the small particles. However, caution

must be taken while interpreting $\Delta a''$ because it is not the true activation area. In fact, understanding the physical meaning of $\Delta a''$ is difficult because local dislocation climb is a multi-step process requiring many coordinated thermodynamic events. In addition, the inhomogeneous distribution of the size and locations of the particles and the non-uniform stress distribution within the material resulting from load-shedding to the large particles further complicate the case. Assuming that $\Delta a''$ does not deviate much from the true activation area, the result suggests that dislocation detachment or general climb are not controlling the creep rate since $\Delta a'' \ll 2\lambda b$.

Table 3-3 The operational activation area for GRCop-84 resolved in b^2 in comparison with the diameter ($2r$) of both small and large Cr_2Nb particles and the interparticle spacing (2λ).

$\Delta a''$	$2r$ (small particles) [7]	$2r$ (large particles) [7]	2λ [7]
250 b^2	220 b	900 b	2080 b

Eqn. 3.4 can be applied to describe steady-state creep of GRCop-84, assuming that the difference in creep rates across different steady states can be attributed to the difference in mobile dislocation densities. The same equation also considers the internal stress acting on the rate-determining dislocations, σ_s, as a sum of the back stress resulting from dislocation-particle interactions and the forward stress caused by dislocation-dislocation interactions. Since σ_s only depends weakly on applied stress and the exact dependence is unknown, as a first approximation, the creep equation takes the average of the three σ_s values from **Table 3-2, -**9 MPa. As the creep equation is very similar to that constructed in Ref. [14] for GlidCop despite different $\hat{\sigma}$ and ΔF values, other details and limitations of this approach are not described here. Fig. 3-4 shows the model fit of the steady-state data from both the present investigation and previous studies [3]. A satisfactory fit of the data is achieved.

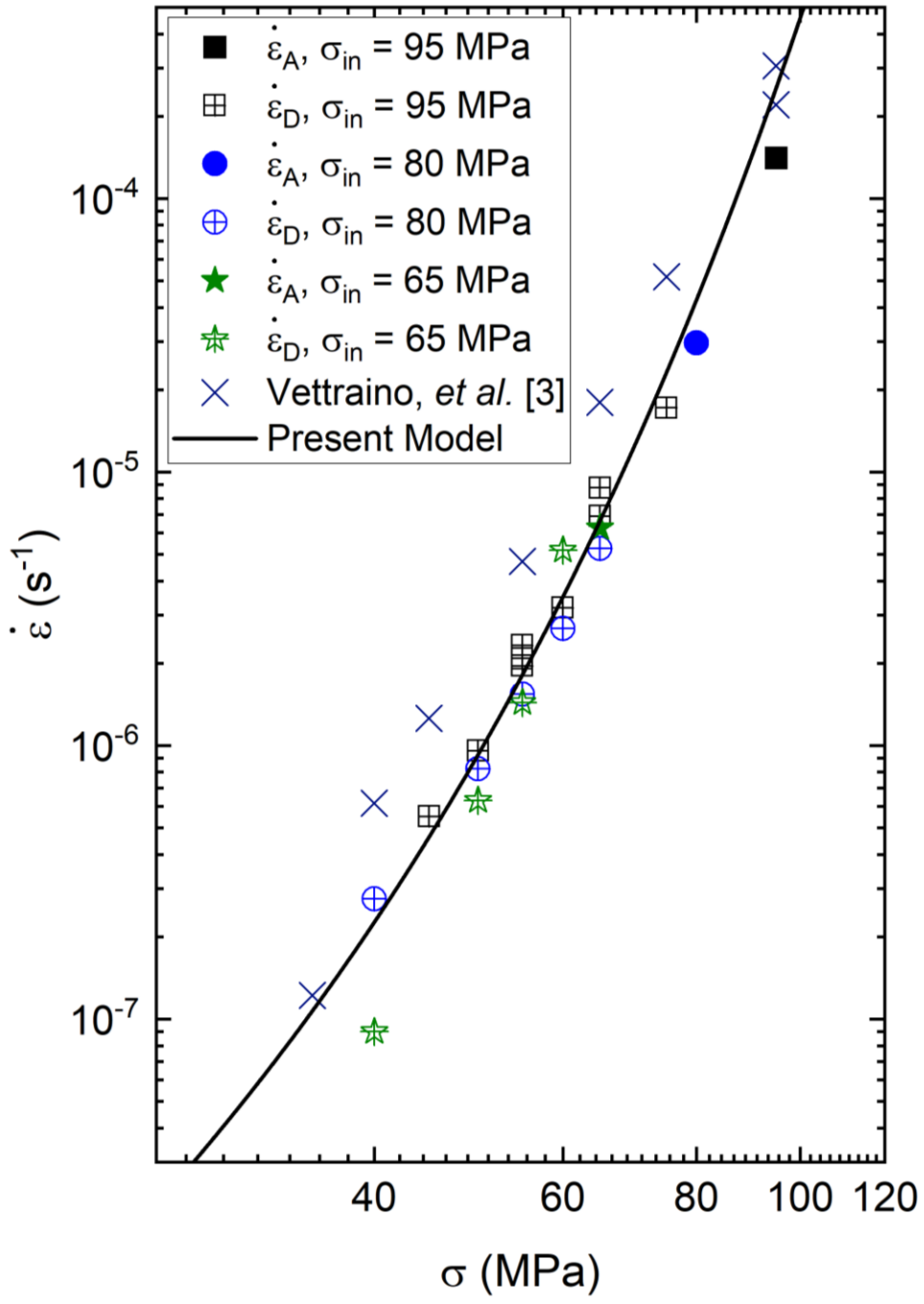

Fig. 3-4 Double logarithmic plots of steady state creep rate versus applied stress for GPCop-84 crept at 923 K. The steady state creep rates under the initial stresses ($\dot{\epsilon}_A$) are demonstrated by the solid symbols, and the open symbols with plus signs represent the steady state creep rates under the reduced stresses ($\dot{\epsilon}_D$). The creep data from Ref. [3] are also included. The solid line shows the model fit (Eqn. 3.4) to the creep data for the present approach.

3.4 Conclusions

The results of the constant-structure creep tests on GRCop-84 at 923 K demonstrate that:

The creep mechanism is confirmed to be local dislocation climb. The mechanical strength of the obstacles is 250 MPa, and the activation energy follows that of self-diffusion in Cu.

The operational activation area was determined to be $250b^2$, which is much smaller than the interparticle spacing 2λ times b. This finding supports the interpretation that the rate-controlling deformation mechanism is local climb at the smaller particles instead of dislocation detachment or general climb. The back stress acting on the ready-to-climb dislocations was measured to be approximately -9 MPa. The steady-state creep behavior of GRCop-84 can be described by substituting the effective stress for the applied stress in a thermally activated creep model.

Acknowledgements

This work was funded by the National Aeronautics and Space Administration Glenn Research Center at Lewis Field (NASA GRC, Cleveland, Ohio) under grant NCC3-859. The authors are especially grateful for the help given by Drs. D.L. Ellis and M.V. Nathal of NASA GRC towards a better understanding of the GRCop-84 material.

References

[1] J.R. Groza, J.C. Gibeling, Mater. Sci. Eng., A 171(1) (1993) 115-125.

[2] D.L. Ellis, Report No. NASA/TM-2005-213566, NASA Glenn Research Center, Cleveland, OH, 2005.

[3] L.G. Vettraino, M. Zhang, J.L.W. Carter, J.R. Groza, J.C. Gibeling, Mater. Sci. Eng., A 756 (2019) 538-544.

[4] M.W. Decker, J.R. Groza, J.C. Gibeling, Mater. Sci. Eng., A 369(1-2) (2004) 101-111.

[5] D.L. Ellis, J.L.W. Carter, M.H. Ferry, Mater. Sci. Eng., A 640 (2015) 1-15.

[6] H.C. de Groh, D.L. Ellis, W.S. Loewenthal, J. Mater. Eng. Perform. 17(4) (2008) 594-606.

[7] L.G. Vettraino, J.L. Heelan, C.A. Faconti, J.L. Walley, A. Garg, J.R. Groza, J.C. Gibeling, J. Mater. Sci. 43(19) (2008) 6546-6555.
[8] W. Blum, B. Reppich, Creep of particle-strengthened alloys, Pineridge Press Ltd., , Swansea, 1985.
[9] J.C. Gibeling, W.D. Nix, Acta Metall. 29(10) (1981) 1769-1784.
[10] M. Biberger, J.C. Gibeling, Acta Metall. Mater. 43(9) (1995) 3247-3260.
[11] G.S. Nakayama, J.C. Gibeling, Acta Metall. Mater. 38(10) (1990) 2023-2030.
[12] S.E. Broyles, J.C. Gibeling, Scr. Metall. Mater. 33(5) (1995) 767-772.
[13] M. Heilmaier, H. Kestler, J.C. Gibeling, Zeitschrift für Metallkunde 93(7) (2002) 666-671.
[14] M. Zhang, S.E. Broyles, J.C. Gibeling, Acta Mater. 196 (2020) 384-395.
[15] U.F. Kocks, A.S. Argon, M.F. Ashby, Prog. Mater. Sci. 19 (1975) 1-281.
[16] R. Lagneborg, Scr. Metall. 7(6) (1973) 605-613.
[17] E. Arzt, J. Rösler, Acta Metall. 36(4) (1988) 1053-1060.
[18] L.M. Brown, R.K. Ham, Dislocation-particle interactions, in: A. Kelly, R.B. Nicholson (Eds.) Strengthening methods in crystals, Amsterdam, 1971, pp. 9-135.
[19] J.L. Walley, J.L. Heelan, L.G. Vettraino, J.R. Groza, J.C. Gibeling, Mater. Sci. Eng., A 527(26) (2010) 6956-6962.
[20] H.J. Frost, M.F. Ashby, Deformation Mechanism Maps: the Plasticity and Creep of Metals and Ceramics, Pergamon Press, Oxford, 1982.
[21] O.D. Sherby, P.M. Burke, Prog. Mater. Sci. 13 (1968) 323-390.

Chapter 4 Mechanisms of Creep Deformation in a Rapidly Solidified Al-Fe-V-Si Alloy[1]

4.1 Introduction

The success of any new high temperature aluminum alloy is contingent upon its ability to withstand significant loads in an elevated temperature environment. In particular, this requirement must be met when designing various aerospace components and energy conversion structures. Some examples of alloys that have been proposed for such applications include the Al-Fe-Ce and Al-Fe-Ni systems, and oxide dispersion-strengthened (ODS) aluminum [1-4]. Ultimately, the goal of developing these high temperature aluminum alloys is to extend their maximum service temperature to three quarters of the melting temperature, or 700 K.

One particular class of alloys that has shown promise for elevated temperature applications is the rapidly solidified Al-8.5 wt% Fe-1.3 wt% V-1.7 wt% Si alloy (FVS0812) developed by Allied Signal Metals and Ceramics Laboratory [5]. This processing method provides the material with an extremely fine scale microstructure of approximately 27 volume percent $Al_{13}(Fe,V)_3Si$ dispersoids uniformly distributed throughout the aluminum matrix [6-10]. The substitution of V for Fe in the silicide phase has been found to stabilize its body centered cubic structure to temperatures approaching 800 K [5]. This high temperature stability provides an explanation of how these alloys retain such a high percentage of their room temperature strengths at elevated temperatures. Because this alloy was designed for rapid solidification processing, it is also an excellent candidate for

[1]Published as M. Zhang, R.J. Lewis, J.C. Gibeling, *Mater. Sci. Eng., A* **805** (2021) 140796

additive manufacturing, which also involves very high cooling rates. Recently, this material has received renewed attention for its potential to be manufactured by selective laser melting andelectron beam melting, especially because it has been proven that the same uniform distribution of the particles can be achieved [11, 12].

Even though the steady-state creep behavior of FVS0812 has been studied by various researchers [8, 10, 13-16], a satisfactory physical description of the creep mechanism has not been reached. Abnormally high stress exponents and activation energies compared to those of pure metals and solid solution alloys were observed and rationalized using a phenomenological threshold stress approach, which relies on a threshold stress that is subtracted from the applied stress [8, 10, 13-15]. However, the physical origin of this threshold stress is still not known. One possibility is to attribute the threshold stress to the increase of dislocation line length during local climb or general climb over the particles, but they have not been proven to be the rate-controlling deformation mechanism. Alternatively, the physics-based Rösler-Arzt (RA) model [17] that is based upon the thermally activated detachment of dislocations from particles was applied in some of these previous studies. However, rather poor fitting was obtained despite extensive efforts, indicating that the basic hypothesis of dislocation detachment control of creep is not consistent with the data. In fact, the reason the RA model does not work for FVS0812 is that the particle/matrix interface is coherent, yet the RA model can only describe creep in DS alloys with incoherent interfaces. Therefore, it is highly desirable to mechanically determine the rate-determining creep mechanism for FVS0812 before a physically justified creep equation can be applied to describe this material.

The above research goal can be achieved by including a set of stress change creep experiments that mechanically probe the material's strain response to a sudden stress change within a very short amount of time, during which the creep microstructure can be assumed to be constant. These so-called constant structure creep tests have been proven to be capable of revealing the rate-controlling deformation mechanisms and applied to several dispersion-strengthened (DS) copper alloys with success in our recent studies [18, 19].

In the present study, the constant stress creep behavior of FVS0812 is examined, and its deformation resistance is compared to other high temperature aluminum alloys. In addition, the effect of aging on creep of the Al-Fe-V-Si alloy is investigated to examine the thermal stability of the microstructure and provide insight as to the suitability of the material in various elevated temperature applications. Finally, the operating deformation mechanisms are probed by performing stress reduction creep experiments to determine creep rates under constant microstructural conditions.

4.2 Experimental

An Al-8.5 wt% Fe-1.3 wt% V-1.7 wt% Si alloy (designated FVS0812 and also known as alloy 8009) was prepared by the rapid solidification/powder metallurgy techniques developed at Allied Signal Metals and Ceramics Laboratory. The alloy was first heated into molten state in a planar flow casting system and then rapidly solidified into thin ribbons at a quench rate of at least ~10^5-10^7 K/s. The ribbons were converted to powder by a comminution process and then degassed and hot pressed in vacuum at 623 K to form billets. The billets were further consolidated by conventional hot extrusion at 673 K [20, 21]. A more detailed description of the processing history can be found in Carreño and Ruano [16]. This processing route produces ~27 vol% of a coherent, metastable $Al_{13}(Fe,V)_3Si$

dispersoid phase (40-80 nm radius) [7] that is uniformly distributed throughout the grain boundaries and grain interiors (grain diameter ~ 500 nm) [22] of the Al matrix. Creep specimens of 35.56 mm gauge length were machined from 1 mm sheets and polished using 240 to 600 grit silicon carbide paper to produce a smooth, uniform surface. Unaged specimens (designated UA) were then annealed in nitrogen for one hour at 673 K to relieve any internal stresses remaining from the machining process. Medium temperature aged (MTA) specimens were annealed in nitrogen for 200 hours at 698 K and high temperature aged (HTA) specimens were annealed in nitrogen for 200 hours at 798 K. All specimens were water quenched to room temperature following the annealing process.

Tensile creep tests were performed on a constant true stress vacuum creep machine at test temperatures ranging from 573 to 823 K at temperature intervals of 50 K and test pressures equal to or lower than 4 x 10^{-3} Pa. The strain was measured by a Schaevitz 200 HR linear variable differential transformer (LVDT) attached to the load train outside the furnace. Stress reduction creep tests were conducted at 573 K from initial stresses (σ_{in}) of 207 MPa and 186 MPa and at 673 K from a σ_{in} of 136 MPa to reduced stresses (σ_{red}) that correspond to 10%, 25% and 35% stress reductions. The details of the test conditions of stress reduction creep experiments are shown in **Table 4-1**. Those tests were performed on the same machine by rapidly removing part of the load at ~10% creep strain after secondary creep was reached under the initial stress. The error on the applied stress associated with the creep load and the lever arm is within 2%. Here we use the notation from Biberger and Gibeling [23] to describe the creep rates at different stages. The steady-state creep rate that corresponds to the initial stress is denoted $\dot{\epsilon}_A$. The immediate strain rate response to the stress reduction at constant creep microstructure was recorded as the constant-structure creep rate, $\dot{\epsilon}_C$. Therefore, $\dot{\epsilon}_C$ represents the rate of deformation under the reduced stress acting upon the microstructure established by the initial stress. The specimens were then allowed to deform under

the reduced stress to the new steady state, where the steady-state creep rate that corresponds to the reduced stress, $\dot{\epsilon}_D$, was also recorded and compared to $\dot{\epsilon}_C$. Only one stress reduction was performed for each specimen.

Transmission electron microscopy was performed on a Philips EM-400 TEM to investigate the probable change in particle size and distribution after aging. Traditional mechanical sample preparation methods were utilized in which the samples were ground and polished to ~100 μm, dimpled to ~25 μm and finally ion milled for 40–100 hours.

Table 4-1 Initial and reduced stresses used in the stress reduction creep tests on FVS0812 at 573 K and 673 K.

T (K)	σ_{in} (MPa)	σ_{red} (MPa)
573	207	186, 155, 134
573	186	167, 138, 121
673	136	122, 102, 89

4.3 Results and Discussion

4.3.1 Creep Curves and Steady-State Creep Properties

Fig. 4-1 shows two example creep curves of FVS0812 deformed at 673 K under stresses of 110 MPa and 97 MPa. Classic primary, secondary and tertiary regimes are observed. The creep curves are typical for all creep tests performed in the current investigation. Normal primary creep (creep rate decelerates to steady state) is present for FVS0812, which was also observed in two other studies [9, 15]. The normal primary was attributed to the reduction in mobile dislocation density caused by subgrain boundary formation and dislocation pinning by particles in recent observations of DS-Cu alloys [18, 19]. These features were also observed in a microstructural study on creep in FVS0812 provided by Peng, *et al.* [10]. The creep ductility is generally good for FVS0812 at ~10%

for temperatures below 773 K and ~25% at 773K and 823 K. The increase in creep ductility may be accompanied with particle coarsening at high temperatures, which is discussed in detail in the next section.

The steady-state creep rates of FVS0812 over a wide range of temperatures and stresses are shown in Fig. 4-2. For comparison, the data of Oliver and Nix [24] for an extruded Al-0.53 wt% C-1.5 wt% O- 0.09 wt% Fe alloy (ODS Al, ~4 vol% Al_2O_3, grain diameter unreported), the data of Yaney and Nix [1] for an extruded Al-8.4 wt% Fe-3.6 wt% Ce alloy (20 vol% $Al_{13}Fe_4$, fine grain size as described), and the data of Carreño and Ruano for an extruded Al - 11.7 wt% Fe - 1.15 wt% V - 2.4 wt% Si alloy (FVS1212, 36 vol% $Al_{13}(Fe,V)_3Si$, grain diameter ~ 500 nm) [25] are shown at overlapping stresses and temperatures in the same plot. In general, the FVS0812 alloy exhibits superior creep strength compared to ODS Al and the Al-Fe-Ce alloy except for 773 K where Oliver and Nix [24] reported threshold behavior under the two stresses tested, resulting in a dramatic decrease in creep rate (the original paper plotted all data together with modulus compensated stress and the two data points at 773 K showed threshold behavior that is not apparent in Fig. 4-2). However, threshold behavior was not observed for FVS0812 in this study. On the other hand, the creep strength of FVS1212 is superior to FVS0812 over all tested stresses and temperatures as expected due to its higher volume fraction of particles. The creep rates obtained in this study compare favorably to the results of previous studies [8, 10, 13] for the same material, albeit some of the present creep rates are lower than in other studies. This slightly greater creep resistance can be attributed to the fact that the initial heat treatment at 673 K (absent in other studies) alleviated the undesirable effects caused by the internal stresses from powder metallurgy and machining process, and that a test temperature of 573 K was not high enough to produce the same stress relief effect. Nonetheless, annealing the

material at an even higher temperature is not advisable because it might cause particle coarsening and thus loss of strength, as discussed in detail below.

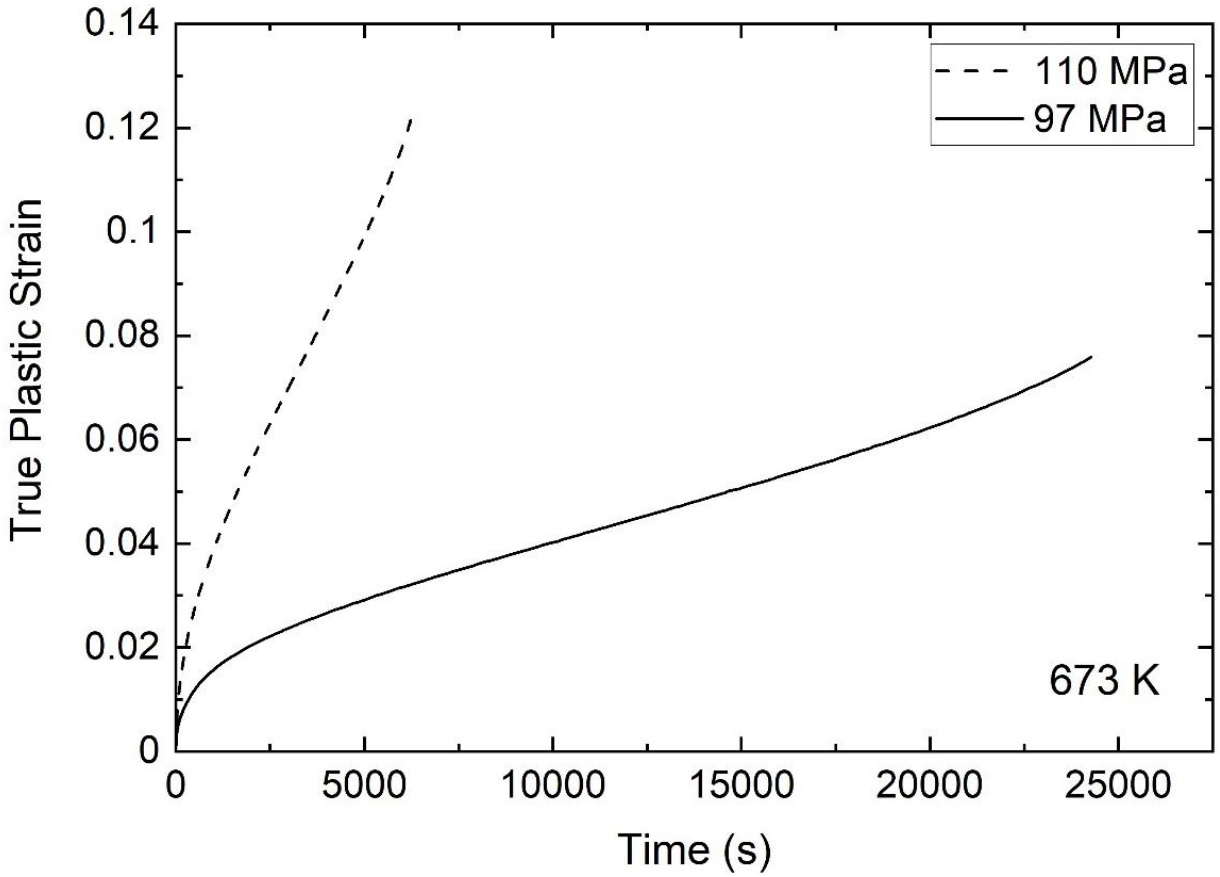

Fig. 4-1 Example creep curves of FVS0812 deformed at 673 K under applied stresses of 110 MPa and 97 MPa showing classic primary, secondary and tertiary regimes.

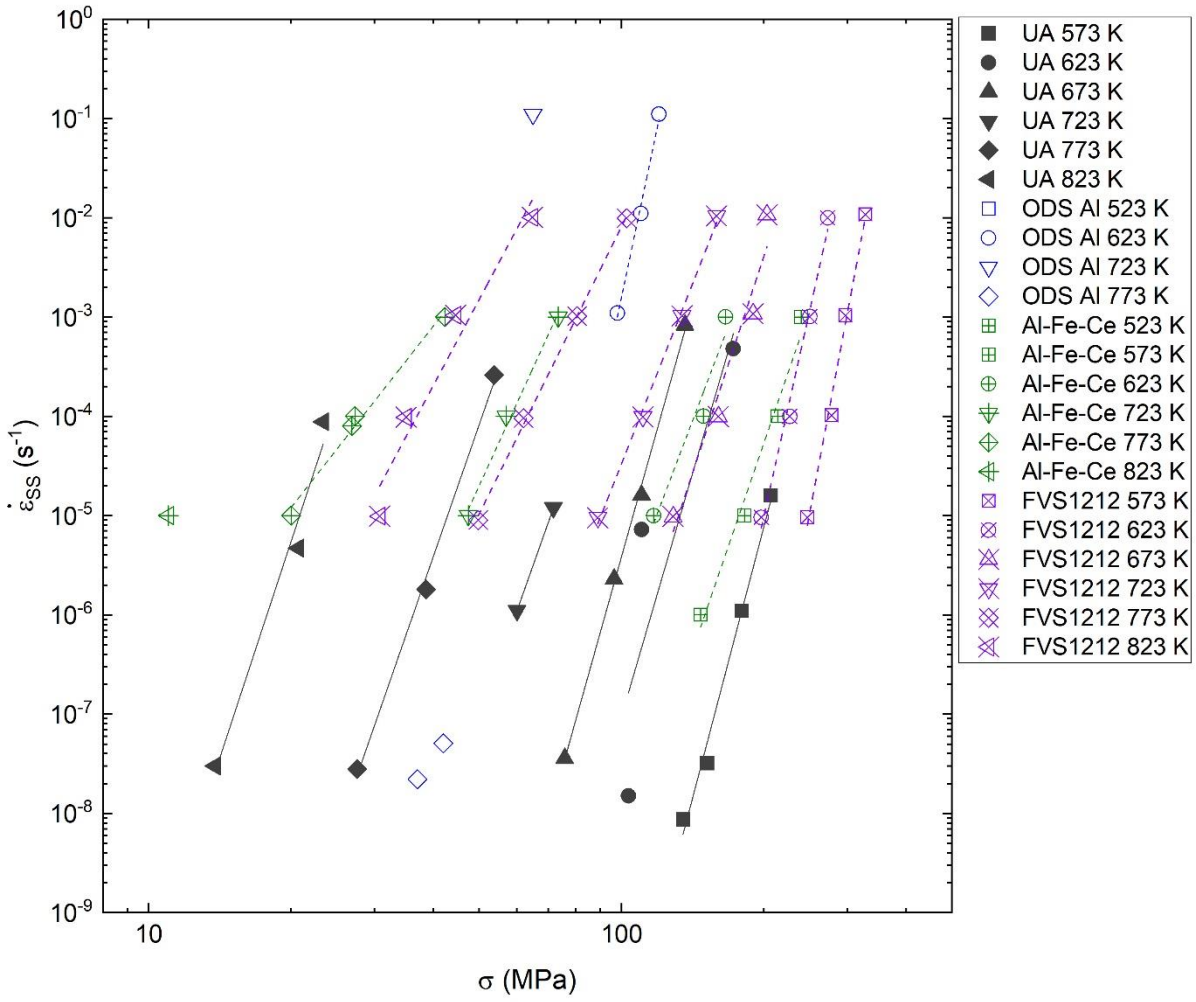

Fig. 4-2 Double Logarithmic plot of steady state strain rate versus true stress for FVS0812 determined in the present study (solid symbols), ODS Al [24] (open symbols), Al-Fe-Ce [1] (open symbols with plus sign), and FVS1212 [25] (open symbols with cross sign).

The simplest form of the power-law relationship between creep rate and stress is given by [26]:

$$\dot{\epsilon}_{SS} = A\sigma^n exp\left(-\frac{Q_c}{RT}\right) \quad (4.1)$$

where $\dot{\epsilon}_{SS}$ is the steady-state creep rate, A is a material constant, σ is the applied stress, Q_c is the apparent activation energy for creep, *R* represents the gas constant, and *T* is the absolute temperature. The stress exponent, n, for dislocation creep is usually in the range of 3 to 8 or for diffusional creep is in the range of 1 to 2 and can be explained by well-understood creep mechanisms [26, 27]. However, much higher stress exponents shown in **Table 4-2** have been found for the FVS0812 alloy, so the simple power-law is not able to rationalize the underlying creep behavior. The n values obtained in this study are consistent with those in multiple other studies [8-10, 13] of FVS0812 and those for a rapidly solidified FVS1212 alloy reported by Pharr, *et al.* [22]. The activation energies were calculated from the creep data between two neighboring isotherms, and an average activation energy equal to 365 ± 44 kJ/mol was identified. This number is also in reasonable agreement with several other studies [8-10, 13, 15]. Q_c is much higher than the activation energy of self-diffusion in aluminum (142 kJ/mol) and still larger than that for diffusion of any of the alloying elements: Fe, V, Si, in Al [28-30], suggesting that creep deformation is not diffusion-controlled. The observed high n and high Q_c is a common trait for DS alloys, and as mentioned in the Introduction, limited success has been obtained in rationalizing them using the threshold stress approach or the RA approach. A more detailed discussion is given in **Section 3.3** by including constant structure creep results.

Table 4-2 Stress exponents, n, in the power-law equation of creep for unaged FVS0812 and the coefficient of determination, R^2, of the linear fit in the power-law model.

Temperature (K)	n	R^2
573	18	0.99
623	16	0.76
673	17	0.99
723	13	1.00
773	14	0.99
823	14	0.98

4.3.2 Aging Effects on Creep

The effect of aging on the creep behavior of FVS0812 is shown in Fig. 4-3. The results of creep experiments on the MTA specimens reveal that the effect of a static anneal at 698K on the creep performance of FVS0812 is negligible, in agreement with an earlier study on FVS1212 which showed that rapidly solidified Al-Fe-V-Si is stable both in microstructure and room temperature mechanical properties for moderate annealing times at temperatures up to 773 K [31]. On the other hand, the current results show that aging at 798 K leads to a severe reduction in the creep resistance of the FVS0812 alloy in that the steady-state strain rate of the HTA specimens is nearly 10 times that of their unaged counterparts at equivalent test stresses and temperatures. The major reason for the degradation is shown qualitatively in Fig. 4-4, where the particles significantly coarsened after HTA but underwent no noticeable change after MTA compared to the UA condition. Other effects such as the coarsening of grains have been shown to have limited effects on the mechanical properties of FVS0812 [32, 33]. Since it is clear that microstructural and mechanical transition takes place when the Al-Fe-V-Si alloys are exposed to temperatures near 800K, caution is warranted for long-term services at such high temperatures.

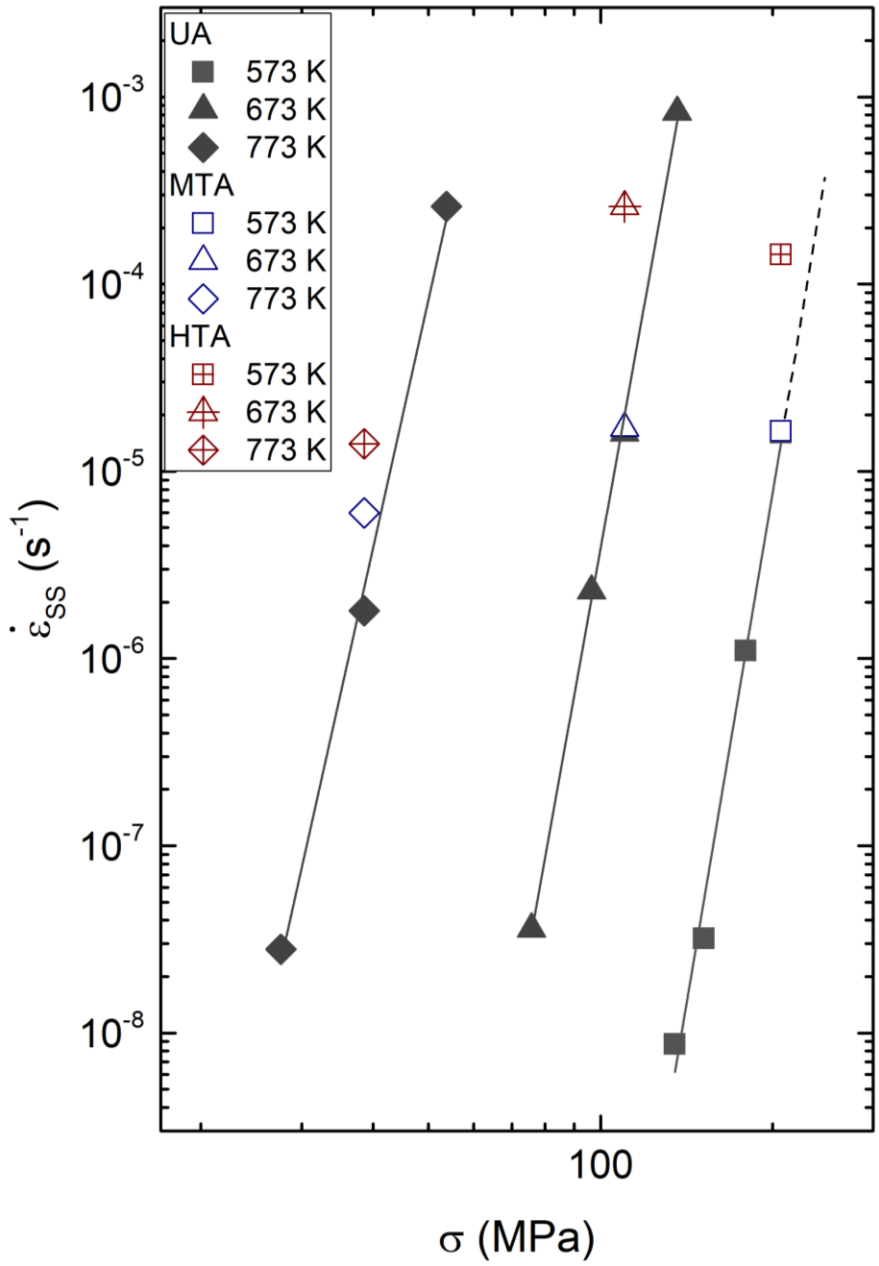

Fig. 4-3 Comparison of the steady state creep rates of UA FVS0812 (solid symbols) to their medium temperature aged (MTA, empty symbols) and high temperature aged (HTA, empty symbols with plus sign) counterparts.

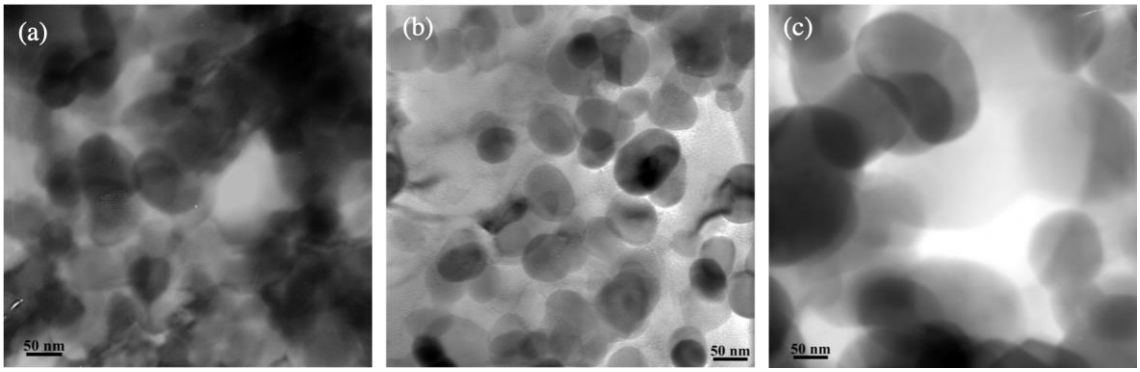

Fig. 4-4 TEM images revealing $Al_{13}(Fe,V)_3Si$ dispersoids in (a) UA; (b) MTA; and (c) HTA FVS0812.

4.3.3 Constant Structure Creep Properties

Recent work on dispersion-strengthened copper alloys has shown that the results of stress reduction tests during creep reveal important mechanistic information about creep behavior in these systems [18, 19]. Such tests capture the instantaneous strain rate response of the material to a sudden stress change, which reflects the dislocation kinetics of the rate-controlling deformation mechanism within the material. For the DS-Cu alloys, $\dot{\epsilon}_C$ is found to be greater than $\dot{\epsilon}_D$ at the same reduced stress, which means that the creep rate immediately after the stress reduction will reduce to the new steady-state value as the microstructure evolves following the stress reduction. This behavior is attributed to the decrease in the dislocation density between the particles and the weakening of dislocation pile-ups in front of the particles which aid forward dislocation motion. An important question is whether similar behavior is observed in DS alloys systems based on other matrix metals. In order to further understand the deformation mechanisms in FVS0812, stress reduction creep tests were conducted at 573 K and 673 K and an example creep curve of the stress reduction strain transient is given in Fig. 4-5.

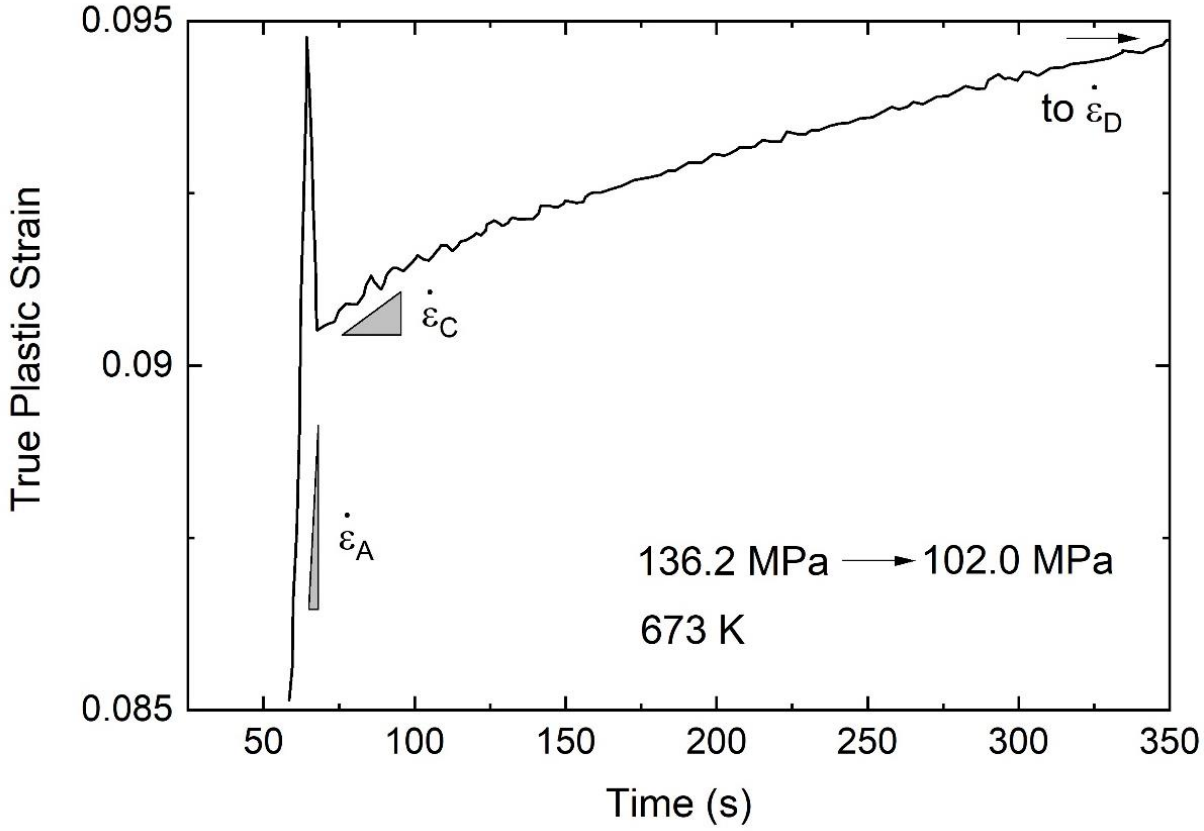

Fig. 4-5 An example creep curve that shows the stress reduction transient of a FVS0812 specimen crept at 673 K with an initial stress of 136 MPa and a reduced stress of 102 MPa. The slopes that correspond to the steady-state creep rate under the initial stress, $\dot{\epsilon}_A$, and the constant-structure creep rate, $\dot{\epsilon}_C$, are indicated in the plot. The arrow shows that the sample will creep onwards and reach a new steady state with a creep rate of $\dot{\epsilon}_D$.

The figure clearly shows that after the stress reduction, $\dot{\epsilon}_C$ is greater than and will decrease to $\dot{\epsilon}_D$. This trend for the stress reduction transients is representative for all experiments. This behavior closely resembles that of two DS-Cu alloys, GlidCop (a Cu alloy strengthened by Al_2O_3 dispersoids) and GRCop-84 (a Cu alloy strengthened by Cr_2Nb particles), as our recent studies find the exact same trends in stress reduction transients [18, 19]. For GlidCop, the constant structure and steady-state creep are controlled by a synergistic effect between near-particle dislocation-dislocation interactions and dislocation detachment from particles. For GRCop-84, the creep rates are controlled by near-particle dislocation-dislocation interactions and local climb.

In order to determine the rate-controlling mechanism in FVS0812, the activation area, $\Delta a''$, is derived from the constant-structure creep results. In the thermally activated dislocation glide framework, the activation area is related to the strain rate and the applied stress as:

$$\dot{\epsilon} = \dot{\epsilon}_0 \, exp\left(-\frac{\Delta G}{k_B T}\right) = \dot{\epsilon}_0 \, exp\left(-\frac{\Delta F - \sigma b \Delta a''/M}{k_B T}\right) \tag{4.2}$$

where $\dot{\epsilon}_0$ is the reference strain rate, k_B is the Boltzmann constant, and ΔG is the Gibbs free energy of activation. ΔG is the thermal energy needed for the dislocations to overcome the barrier, and can be written as the total activation barrier energy, ΔF (also called the Helmholtz free energy of activation), reduced by the external work done by the applied stress, $\sigma b \Delta a''/M$, where b is the Burgers vector and M is the Taylor factor. Here, b is 0.286 nm for Al and M is 3.06 for a randomly oriented FCC crystal. Physically, $\Delta a''$ describes the area swept by the dislocation during the activation event, and thus $\Delta a''$ should be close to the separation of the rate-controlling obstacles

times b. Operationally, $\Delta a''$ can be determined by taking the derivative of $ln\dot{\epsilon}_C$ with respect to σ in Eqn. 4.2:

$$\Delta a'' = \frac{Mk_BT}{b} \cdot \frac{\partial ln\dot{\epsilon}_C}{\partial \sigma}\Big|_{T,\hat{\sigma}_i} \tag{4.3}$$

where $\hat{\sigma}_i$ describes the flow strengths provided by the microstructural features (e.g. subgrains, dislocation forests, particles). Since this derivative is evaluated at constant T and $\hat{\sigma}_i$, it is necessary to use the constant structure creep rates obtained by a set of stress reduction creep tests conducted at a constant temperature. Using the steady-state creep rates to determine $\Delta a''$ will not be meaningful because the microstructure is different across different steady states.

Caution must be taken before applying Eqn. 4.3 in that FVS0812 features a high volume fraction of relatively large particles and must be treated as a composite. The actual stress acting on the dislocations in the matrix needs to take into account the load transfer from the matrix to the particles to obtain accurate results for $\Delta a''$. Since TEM studies of dislocation-particle interactions in creep of FVS0812 do not reveal shearing of particles and creation of antiphase boundaries [9, 10, 15], here we adopt the expression of Hong, *et al.* [34] for composites strengthened by non-deformable particulates, which is a simplified version of the original model from Nardone and Prewo [35]:

$$\sigma_{eff} = \sigma \left[1 - \frac{f \cdot \left(\frac{S}{2} + 1\right)}{f \cdot \left(\frac{S}{2} + 1\right) + (1 - f)} \right] \tag{4.4}$$

where σ_{eff} is the effective stress on the matrix after accounting for load transfer, f is the volume fraction of the particles, and S = 1 is the aspect ratio of the particles. We note that σ_{eff} is linearly

proportional to σ and the proportionality is only a function of f and S, which are constants since only one material is under consideration. Therefore, this correction of the applied stress only shifts the data on the double logarithmic strain rate-stress plot horizontally to the left and does not affect the stress exponent and the apparent activation energy determined earlier. Nevertheless, the amount of load transferred to the particles was calculated to be 36% of the applied load, which is certainly too large to ignore in the calculation of $\Delta a''$.

The results of the stress reduction creep experiments are given in Fig. 4-6, where σ_{eff} is taken to be 64% of the applied stress in all cases. Again, the relation of $\dot{\epsilon}_C > \dot{\epsilon}_D$ is universal among all tests. The activation areas derived from Eqn. 4.3 with corrected σ_{eff} are given in **Table 4-3**. It appears that $\Delta a''$ for FVS0812 at 573 K is fairly low at ~$40b^2$ and at 673 K is ~$175b^2$, both of which are significantly less than the average interparticle spacing, 2λ, times b and the average particle size, $2r$, times b. The values of 2λ and $2r$ were determined by Peng, *et al.* [10] to be 131 nm and 47 nm, respectively. It has been noted that $\Delta a''$ for the dislocation detachment mechanism is approximately equal to $2\lambda b$ [18], and $\Delta a''$ for the local climb mechanism is close to $2rb$ [19]. In both cases $\Delta a''$ correlates well with the length scale of their respective obstacles. For general climb, $\Delta a''$ should also be ~$2\lambda b$ in theory. In addition, the theoretical threshold stress associated with general climb [36] is on the order of 0.002-0.04 times the Orowan stress (150-220 MPa for FVS0812 in this study and refs. [10, 13, 14]). However, the threshold stresses measured in refs. [10, 13, 14] are in the range of 50-110 MPa, which are much higher than those for general climb. Therefore, the rate-determining deformation mechanism in FVS0812 is unrelated to these three specific types of dislocation-particle interactions and appears to operate on a smaller length scale.

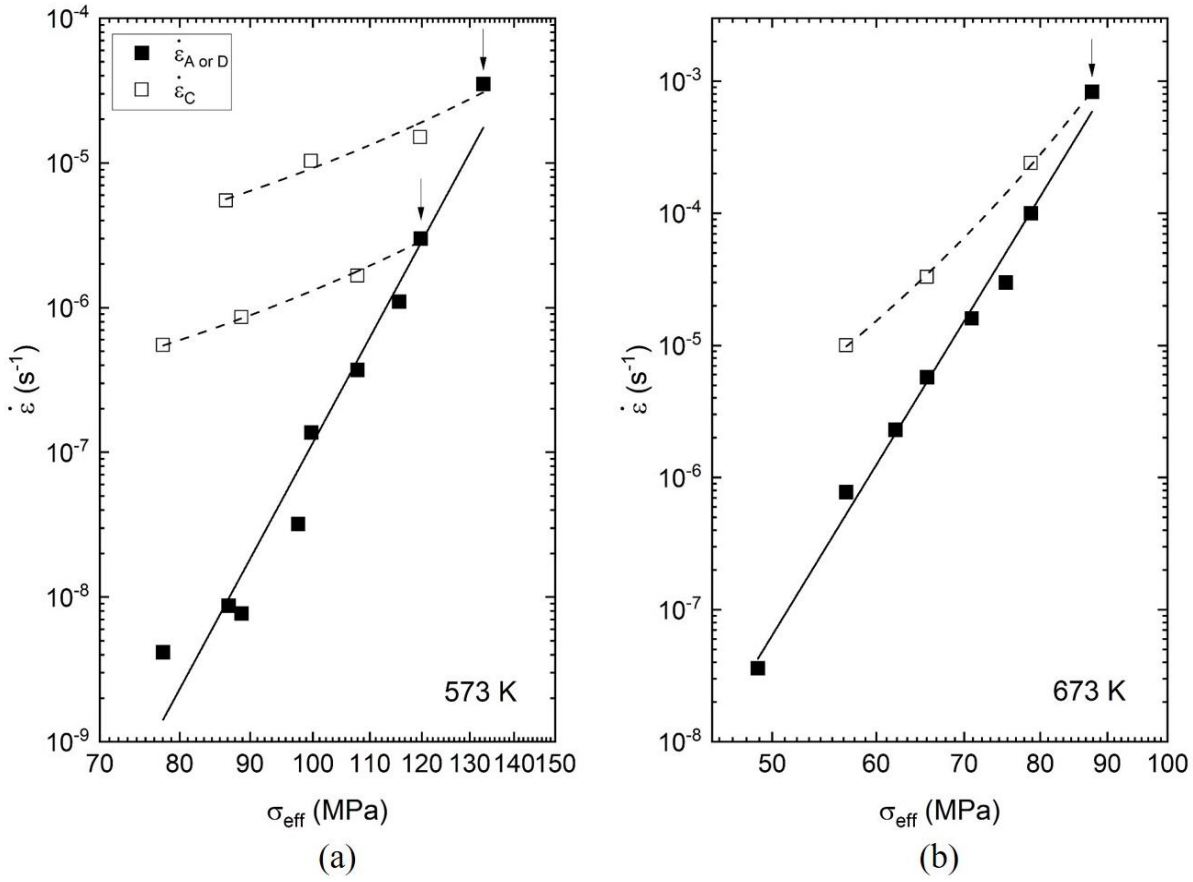

Fig. 4-6 Double logarithmic plots of both constant structure and steady-state creep rates versus true applied stress for FVS0812 at (a) 573 K; and (b) 673 K. The black arrows indicate the initial stress before stress reduction. The solid lines represent the linear fit for $\dot{\epsilon}_{SS}$ on a double logarithmic scale that describes the power-law relation given in Eqn. 4.1. The dashed lines exhibit the linear fits for $\dot{\epsilon}_{CS}$ on a semilogarithmic scale (curved in the current double logarithmic plots) that describes the exponential relation given in Eqn. 4.2.

Table 4-3 The operational activation areas for FVS0812 resolved in b^2 determined from two sets of stress reduction creep experiments. A comparison with the average interdislocation spacing (l), particle size ($2r$), and interparticle spacing (2λ) is also provided.

$\Delta a''$	T (K)	σ_{in} (MPa)	σ_{eff} (MPa)	l	$2r$	2λ
38 b^2	573	207	133	130 b	329 b	458 b
41 b^2	573	186	120	145 b	329 b	458 b
176 b^2	673	136	88	186 b	329 b	458 b

Since neither the dislocation detachment nor climb models are relevant to FVS0812, the rate-controlling deformation mechanism should alternatively be focused on the dislocation network between the particles. As a first approximation, we assume the average inter-dislocation spacing, l, to follow the Taylor hardening equation:

$$l = \frac{M\alpha\mu b}{\sigma} \tag{4.5}$$

where α is the Taylor hardening constant and is equal to 0.2 for Al [37], and the shear modulus μ for FVS0812 is taken from Pickens [38]. The temperature dependence of μ is assumed to be similar to that of Al [27]. The resulting values are given in **Table 4-3**. It is evident that $\Delta a''$ is much closer to lb than to the two particle parameters ($2rb$ and $2\lambda b$). More importantly, $\Delta a''$ captures a stress dependence similar to that of l, which serves as strong evidence that dislocation-dislocation interactions are the rate-determining deformation mechanism. Microscopically, high-density dislocation networks have been observed in dispersoid-sparse regions in FVS0812 [10]. We further note that unlike GlidCop that has a virtually pure Cu matrix, the matrix of FVS0812 is an Al-0.5 at. % Fe supersaturated solid solution [39] (resulting from rapid solidification) so that the additional pinning and unpinning of mobile dislocations by solutes (not to be confused with solute drag) can also be relevant. In fact, another study on Al solid solutions has shown that activation areas for solute control is on the order of 100 b^2 [40], which is similar to what has been determined for FVS0812.

Decoupling the contributions of the two interactions requires extensive efforts of stress reduction creep tests carried out from a variety of initial stresses to generate a Haasen plot for this material, which is beyond the scope of the present paper.

Identification of the creep mechanism immediately leads to two questions. The first question is related to the unsolved problem of rationalizing the high stress exponent and apparent activation energy. If the threshold stress model were to be used, how could a threshold stress be justified if none of the Orowan bowing mechanism, climb mechanisms, or dislocation detachment mechanism is controlling the rate? The second question is related to the observed form of the stress reduction transients in particle-strengthened metals. Why does FVS0812 exhibit the same stress reduction transients ($\dot{\epsilon}_{CS} > \dot{\epsilon}_{SS}$) as those observed in DS-Cu alloys, where the creep rate is controlled by dislocation-particle interactions? And why does FVS0812 not show the opposite stress reduction transient ($\dot{\epsilon}_{CS} < \dot{\epsilon}_{SS}$) that is widely observed in pure metals and class M alloys, where the creep rate is controlled by forest dislocations [41-43]?

The first question can be answered by considering the role that the particles play in this material. Besides being load carriers, they are also physical barriers that obstruct dislocation motion, which could lead to long-range back stresses on the dislocations in the network. In fact, Carreño and Ruano [16] phenomenologically separated the contribution of the matrix and the particles to creep deformation, and they determined a stress exponent of 8 for the matrix, which corresponds to a dislocation creep mechanism without subgrain coarsening. However, the physical origin of the stress dependence of creep caused by the particles still remains unclear. A possible mechanism is provided as follows: when dislocations approach the particles that have a much greater shear modulus than

the matrix, they are subject to repulsion because of the significant difference of shear moduli between the matrix and the particles. A coherent particle/matrix interface is not likely to relax the repulsive force by diffusion or slip. However, this argument remains speculative so far because quantitatively measuring or modeling this back stress is difficult in that the temperature-dependent shear modulus and the Poisson's ratio of the precipitate are unknown. Future work is needed to provide this information by either experiment or simulation.

The second question can be answered by another important role that the particles play in FVS0812. The increasing creep rate after stress reduction observed in pure metals and class M alloys is ascribed to the coarsening of subgrains so that the obstruction of dislocation glide is reduced until the substructure reaches a strength that is appropriate for the reduced stress. This effect overwhelms the excess dynamic recovery of mobile dislocation density caused by the stress reduction that will otherwise decrease the creep rate. However, since the coarsening process is inhibited by the presence of the particles in FVS0812, a decreasing creep rate from the constant-structure regime to the new steady-state regime is indeed expected in this material as previously observed in two particle strengthened copper alloys [18, 19]

4.4 Conclusions

The results presented in this work show that FVS0812 exhibits superior creep resistance compared to ODS Al and Al-Fe-Ce at high stresses and temperatures below 773 K. However, ODS Al is superior to FVS0812 when the test temperature reaches 773 K. The present data demonstrate that the activation energy for creep in this alloy is 365 ± 44 kJ/mol, a value similar to that obtained for a related alloy, FVS1212. This large activation energy, along with stress exponents of 13 and above,

indicates that creep does not occur by a simple diffusion-controlled power-law mechanism. In addition, the effort in fitting the creep data to the Rösler-Arzt model has also not been satisfactory, suggesting that the actual controlling mechanism is not the dislocation detachment process.

The operational activation areas for FVS0812 determined by stress reduction creep experiments and thermally activated glide analysis are ~40 b^2 at 573 K and ~175 b^2 at 673 K, which are much lower than the average interparticle spacing or the particle size times the Burgers vector. Instead, the activation areas are similar to those of dislocation-dislocation and dislocation-solute interactions, suggesting that these mechanisms control creep deformation of FVS0812 and that the particles play an indirect role. Finally, aging for 200 hours at 698 K has little or no effect on creep performance of the Al-Fe-V-Si alloy. In contrast, a reduction in creep resistance was observed in the samples that were aged for 200 hours at 798 K due to particle coarsening.

Acknowledgements

The initial creep experiments were conducted under the sponsorship of the Air Force Office of Scientific Research grant AFOSR 86-0091. The authors wish to thank Dr. Paul S. Gilman, formerly of the Alloys Department, Allied-Signal, Inc., for providing the material for testing. The generous contribution from A.M. Jenderseck to the experimental portion of this investigation is also gratefully acknowledged.

References

[1] D.L. Yaney, W.D. Nix, Metall. Mater. Trans. A 18(5) (1987) 893-902.
[2] F. Průša, D. Vojtěch, A. Michalcová, I. Marek, Mater. Sci. Eng., A 603 (2014) 141-149.
[3] A.H. Clauer, N. Hansen, Acta Metall. 32(2) (1984) 269-278.
[4] A.H. Monazzah, A. Simchi, S.M.S. Reihani, Mater. Sci. Eng., A 527(10) (2010) 2567-2571

[5] D.J. Skinner, R.L. Bye, D. Raybould, A.M. Brown, Scr. Metall. 20(6) (1986) 867-872.
[6] Allied-Signal High Temperature Al-Fe-V-Si Alloys Data Sheet, Morristown, NJ, 07960.
[7] D.J. Skinner, The Physical Metallurgy of Dispersion Strengthened Al-Fe-V-Si Alloys, in: Y.M. Kim, W.M. Griffith (Eds.) Dispersion Strengthened Aluminum Alloys, The Minerals, Metals and Materials Society, Phoenix, AZ, 1988, pp. 181-198.
[8] F. Carreño, G. González-Doncel, O.A. Ruano, Mater. Sci. Eng., A 164(1) (1993) 216-219.
[9] S.C. Khatri, A. Lawley, M.J. Koczak, K.G. Grassett, Mater. Sci. Eng., A 167(1) (1993) 11-21.
[10] L.M. Peng, S.J. Zhu, Z.Y. Ma, J. Bi, H.R. Chen, F.G. Wang, Mater. Sci. Eng., A 259(1) (1999) 25-33.
[11] S. Sun, L. Zheng, Y. Liu, J. Liu, H. Zhang, J. Mater. Res. 30(10) (2015) 1661-1669.
[12] S.B. Sun, L.J. Zheng, H. Peng, H. Zhang, Mater. Sci. Eng., A 659 (2016) 207-214.
[13] S.J. Zhu, K. Kuchařová, J. Čadek, Metall. Mater. Trans. A 31(9) (2000) 2229-2237.
[14] Z.Y. Ma, S.C. Tjong, Mater. Sci. Eng., A 278(1-2) (2000) 5-15.
[15] S. Mitra, Metall. Mater. Trans. A 27(12) (1996) 3913-3923.
[16] F. Carreño, O.A. Ruano, Acta Mater. 46(1) (1998) 159-167.
[17] J. Rösler, E. Arzt, Acta. Metall. Mater. 38(4) (1990) 671-683.
[18] M. Zhang, S.E. Broyles, J.C. Gibeling, Acta Mater. 196 (2020) 384-395.
[19] M. Zhang, J.C. Gibeling, Scr. Mater. 190 (2021) 131-135.
[20] D.J. Skinner, Rapidly solidified aluminum based alloys containing silicon for elevated temperature applications, Allied Corporation, United States Patent US4729790A, 1988.
[21] S.K. Das, R.L. Bye, P.S. Gilman, Mater. Sci. Eng., A 134 (1991) 1103-1106.
[22] G.M. Pharr, M.S. Zedalis, D.J. Skinner, P.S. Gilman, High Temperature Creep Deformation of a Rapidly Solidified Al-Fe-V-Si Alloy, in: Y.M. Kim, W.M. Griffith (Eds.) Dispersion Strengthened Aluminum Alloys, The Minerals, Metals and Materials Society, Phoenix, AZ, 1988, pp. 309-322.
[23] M. Biberger, J.C. Gibeling, Acta. Metall. Mater. 43(9) (1995) 3247-3260.
[24] W.C. Oliver, W.D. Nix, Acta. Metall. 30(7) (1982) 1335-1347.
[25] F. Carreño, O.A. Ruano, Mater. Sci. Tech.-Lond. 14(4) (1998) 322-327.
[26] O.D. Sherby, P.M. Burke, Prog. Mater. Sci. 13 (1968) 323-390.
[27] H.J. Frost, M.F. Ashby, Deformation mechanism maps: the plasticity and creep of metals and ceramics, Pergamon Press, Oxford, 1982.
[28] K. Sørensen, G. Trumpy, Phys Rev B 7(5) (1973) 1791-1797.
[29] S.P. Murarka, M.S. Anand, R.P. Agarwala, Acta Metall. 16(1) (1968) 69-72.
[30] S.-i. Fujikawa, K.-i. Hirano, Y. Fukushima, Metall. Trans. A 9(12) (1978) 1811-1815.
[31] R.E. Franck, J.A. Hawk, Scr. Metall. 23(1) (1989) 113-118.
[32] J. Benci, W. Frazier, Microstructural stability and creep response of a new Al-Fe-W-Si alloy, NADC-91030-60, Naval Air Development Center, Warminster, PA 1991.
[33] D.Y. Lee, D.E. Zupon, High Temperature Performance of Dispersion Strengthened P/M Aluminum Alloys, in: Y.M. Kim, W.M. Griffith (Eds.) Dispersion Strengthened Aluminum Alloys, The Minerals, Metals and Materials Society, Phoenix, AZ, 1988, pp. 265-282.
[34] S.H. Hong, K.H. Chung, Key Eng. Mater. 104-107 (1995) 757-764.
[35] V.C. Nardone, K.M. Prewo, Scr. Metall. Mater. 20(1) (1986) 43-48.

[36] W. Blum, B. Reppich, Pineridge Press Ltd., Creep Behaviour of Crystalline Solids (1985) 83-135.
[37] M.E. Kassner, K. Kyle, in: M.A. Meyers, R.O. Ritchie, M. Sarikaya (Eds.), Nano and Microstructural Design of Advanced Materials, Elsevier Science Ltd, Oxford, 2003, pp. 255-271.
[38] J.R. Pickens, High-Strength Aluminum Powder Metallurgy Alloys, in: A.S.M. Handbook Committee (Ed.) Properties and Selection: Nonferrous Alloys and Special-Purpose Materials, ASM International, 1990.
[39] D.J. Skinner, M.S. Zedalis, P. Gilman, Mater. Sci. Eng., A 119 (1989) 81-86.
[40] B.J. Diak, S. Saimoto, Mater. Sci. Eng., A 234-236 (1997) 1019-1022.
[41] B. Wilshire, M. Willis, Metall. Mater. Trans. A 35(2) (2004) 563-571.
[42] G.S. Nakayama, J.C. Gibeling, Acta. Metall. Mater. 38(10) (1990) 2023-2030.
[43] S.E. Broyles, J.C. Gibeling, Scr. Metall. Mater. 33(5) (1995) 767-77

Chapter 5 Tensile Creep Properties of a CrMnFeCoNi High-Entropy Alloy[1]

5.1 Introduction

In recent years, the advent of high-entropy alloys (HEAs) and multi-principal element alloys (MPEAs) has brought forth new opportunities to discover and design structural materials with attractive mechanical properties [1, 2]. One of the most studied candidates is equiatomic CrMnFeCoNi, which features a uniform FCC single phase over a wide range of temperatures [3, 4]. Several studies suggest that this alloy possesses a good combination of strength and ductility, especially at lower temperatures [5-7]. The simplicity of its structure combined with a distribution of atomic species also make CrMnFeCoNi an excellent candidate for the matrix of an oxide-dispersion-strengthened (ODS) alloy or a metal matrix composite (MMC) for high temperature applications. For example, Dobeš, *et al.* [8] described an yttrium oxide strengthened CrMnFeCoNi alloy, which has superior creep strength over conventional ODS alloys based on pure metal or dilute alloy matrices (e.g. ODS-Cu [9], ODS-Fe-Cr [10]). To further explore the promises of creep-resistant alloys based on CrMnFeCoNi, it is essential to have a fundamental understanding of the creep properties and underlying deformation mechanisms of this matrix alloy.

Several researchers have examined the deformation behavior of CrMnFeCoNi at elevated temperatures: Cao, *et al.* [11] and Kang, *et al.* [12] investigated tensile creep behavior of CrMnFeCoNi at intermediate temperatures (773 K - 923 K) and discovered a transition of

[1]Published as M. Zhang, E.P. George, J.C. Gibeling, *Scr. Mater.* **194** (2021) 113633

mechanisms from dislocation climb to viscous glide, and then to power-law breakdown. However, the formation of second phases (e.g. Cr-rich σ phase [13, 14]) at such temperatures can add ambiguity to the interpretation of the creep results as evidence shows that dislocations readily interact with these precipitates [15]. Dobeš, *et al.* [8] studied the compressive creep behavior of an ultrafine-grained version of the alloy (~0.8 μm in size) at higher temperatures (973 K – 1073 K) and reported a stress exponent of 6 which seems to indicate dislocation climb as the rate-controlling mechanism. Nonetheless, the small grain size can obscure the comparison of the stress exponent with conventional alloys, for which creep tests are normally done on coarser-grained materials [16]. He, *et al.* [17] carried out high temperature tensile tests (1023 K – 1123 K) and found a dependence of strain rate on flow stress with a stress exponent of 3 over the same stress range as Dobeš, *et al.* [8], suggesting glide-controlled creep. Under higher stresses, a transition to five-power-law creep was observed. However, there are challenges in obtaining creep correlations from displacement-controlled tensile tests at elevated temperatures related to uncertainty as to whether steady state flow is achieved.

In the present study, we report on the tensile creep properties of CrMnFeCoNi with an intermediate grain size in the high temperature regime (1023 K – 1173 K) under constant true stress conditions. In addition, we provide insights into the rate-controlling deformation mechanism(s) for CrMnFeCoNi through analyses of creep data and characterizations of steady-state creep microstructure.

5.2 Experimental

Equiatomic CrMnFeCoNi used in this study was produced by arc-melting and drop casting using the procedures described in Ref. [18]. The as-cast material was homogenized in vacuum at 1473 K for 24 hours and rolled at room temperature to a thickness of ~1 mm (~95% thickness reduction). Flat creep specimens with a gauge section having dimensions of 35.56(L) × 2.54(W) × 1.00(H) mm were electrical discharge machined from the cold-rolled sheets. The specimens were annealed in a vacuum furnace at 1173 K for 1 hour for complete recrystallization. Before creep testing, samples were polished by 400 and 600 grit SiC abrasives to reduce the potential influence of surface effects on the creep properties.

Tensile creep tests were performed at constant true stress under vacuum ($\leq 2 \times 10^{-5}$ torr) following the procedures used in our previous studies [19-21]. Test temperatures were chosen from 1023 K to 1173 K at 50 K intervals, where formation of second phases is negligible throughout the time frame of creep testing [3, 13]. Most tests were conducted to tertiary stage to ensure that steady state rates could be measured, although selected tests were interrupted at steady state and specimens were furnace cooled under stress to preserve the deformed microstructure for further microstructural investigations.

Scanning electron microscopy was conducted on a FEI Scios Dualbeam FIB SEM to investigate the grain characteristics of CrMnFeCoNi before and after testing. The initial grain size was measured by the line intercept method that conforms to ASTM E1382-97 [22] on micrographs showing electron channeling contrast. Selected creep specimens were then characterized by electron backscatter diffraction (EBSD) at an operating voltage of 15 kV and the EBSD data

were post-processed by an open source toolbox MTEX (version 5.4.0) on Matlab [23] following the same procedures as in [21]. All SEM samples were prepared by grinding and polishing down to 0.3 μm alumina and then vibropolishing with 0.05 μm colloidal silica for up to 4 hours.

Transmission electron microscopy was performed on a JEOL 2100F-AC TEM at an accelerating voltage of 200 kV to examine the dislocation substructure formed under creep deformation. Conventional mechanical pre-thinning methods were used for sample preparation, which include grinding, 3 mm disc punching, polishing and dimpling. The discs were then perforated by a Fischione 1050 TEM ion mill at 5kV, followed by a final polishing at 1 kV for 30 minutes and 0.5 kV for an hour to alleviate ion beam damage.

5.3 Results and Discussion

Fig. 5-1 illustrates the microstructure of the creep specimens prior to testing. The grains are fully recrystallized and equiaxed after the annealing treatment with an average size of 24 ± 12 μm as shown in the histogram. The annealing conditions were tailored to produce an intermediate grain size for two reasons: i) the grain size should be coarse enough to avoid grain boundary sliding; and ii) the grain size should be fine enough in the thickness direction to ensure that polycrystalline behavior is measured. The material consists of a pure (single) FCC phase that is precipitate-free despite some sparsely distributed oxide inclusions. The initial microstructure of the material is consistent with that in Ref. [24], which provides a more detailed description of thermomechanical processing of cold rolled CrMnFeCoNi.

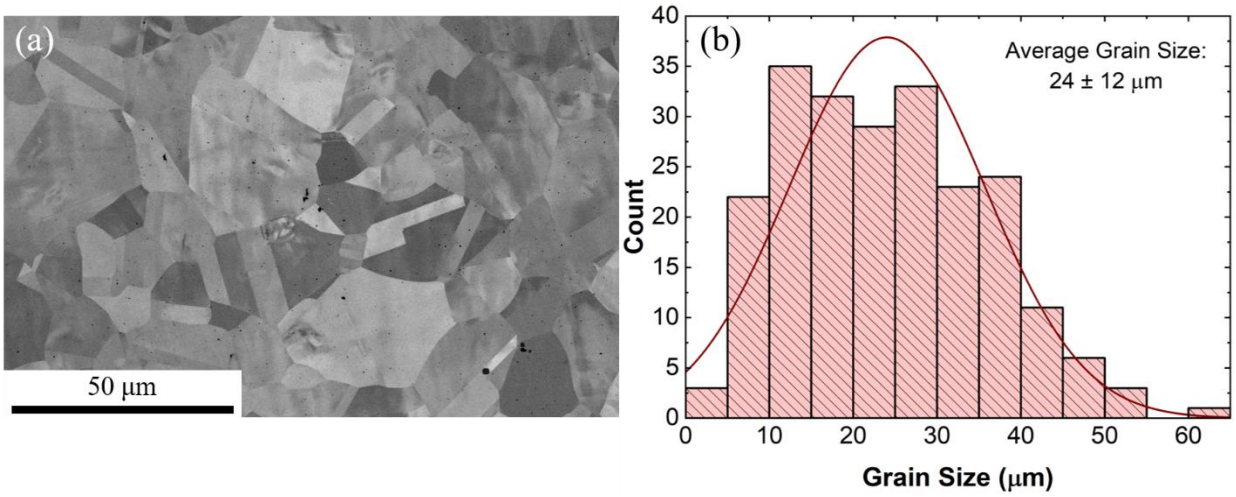

Fig. 5-1(a) Backscattered electron micrograph of the microstructure of CrMnFeCoNi after annealing at 1173 K for 1 hour; (b) Histogram of the grain sizes measured by the line intercept method. The red curve shows the Gaussian fit to the histogram.

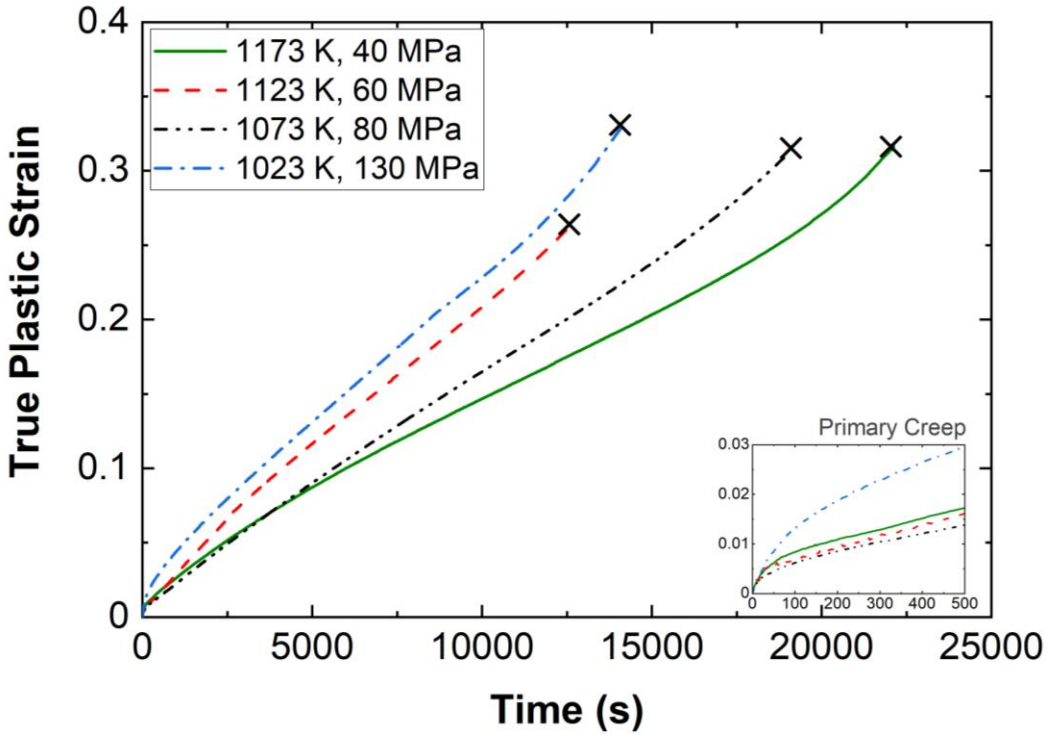

Fig. 5-2 Example tensile creep curves for CrMnFeCoNi samples crept at 1023 K – 1173 K with selected stresses that result in similar creep rates. The "×" sign indicates fracture of the creep sample. The inset provides an expanded view of the primary creep region.

Example creep curves obtained from the creep experiments on CrMnFeCoNi are shown in Fig. 5-2 and feature classic primary, secondary and tertiary regions. Secondary creep lasts for reasonably long periods for this HEA and the creep rates in this region are truly steady-state creep rates. These trends are representative for all tests performed in this study. Normal primary creep serves as an indication of a decrease in mobile dislocation density before reaching steady state, which is typically dominated by the formation of subgrain boundaries in pure metals and class M alloys [25].

The relationship between steady-state creep rate, $\dot{\epsilon}_{SS}$, and applied stress, σ, is shown in Fig. 5-3a, which follows the phenomenological power law equation [16]:

$$\dot{\epsilon}_{SS} = A\sigma^{n} exp\left(-\frac{Q_c}{RT}\right) \tag{5.1}$$

where A is a material constant, n is the stress exponent, Q_c is the apparent activation energy of creep, R is the ideal gas constant, and T is the absolute temperature. Q_c is obtained via the slope of the Arrhenius plot given in Fig. 5-3b. The fitted values of n and Q_c and their standard deviations are summarized in **Table 5-1**. An almost perfect power-law relation holds between $\dot{\epsilon}_{SS}$ and σ and gives very consistent stress exponents, n = 3.7±0.1, across all four temperatures. No obvious transitions between different mechanisms were observed within the temperature and stress ranges tested in this investigation. However, the n values are below the commonly observed values (4 – 7) for dislocation climb-controlled creep [16] but above that (~3) for viscous glide-controlled creep [26]. In terms of Q_c, the obtained values are slightly lower than the activation energies of tracer diffusion in the CrMnFeCoNi matrix (272 – 313 kJ/mol for the five elements [27]). Combined with

the fact that Q_c decreases with increasing applied stress, the activation energies of creep in CrMnFeCoNi clearly indicate the creep mechanism is a stress-assisted, thermally activated process. The above evidence suggests that creep of CrMnFeCoNi at high temperatures is co-determined by dislocation-dislocation interactions and dislocation-lattice interactions without a clear transition between mechanisms.

Table 5-1 Calculated power-law model parameters, n, Q_c and their respective coefficients of determination R^2.

T (K)	n	R^2
1173	3.6 ± 0.1	0.997
1123	3.7 ± 0.1	0.999
1073	3.8 ± 0.1	0.999
1023	3.6 ± 0.1	0.995

σ (MPa)	Q_c (kJ/mol)	R^2
80	218.7 ± 15.9	0.990
60	225.1 ± 10.1	0.996
40	235.9 ± 10.2	0.996

A comparison of the essential creep parameters between our study and previous studies is included in **Table 5-2**. In studies at intermediate temperatures [11, 12], glide control of dislocation motion was ascribed to the drag force created by nanoscale segregations of certain species to create clusters and/or short-range order (SRO) at dislocation cores. At high temperatures as in the present study, the extent of such clustering diminishes because disordering becomes more thermodynamically favored, weakening the drag force. In addition, the drag force can be more easily overcome at these temperatures due to greater available thermal energy. However, the amount of glide resistance does not seem to become completely negligible, as the stress exponent remains relatively low. On the other hand, the power-law breakdown behavior observed at intermediate temperatures was absent in our study. This may be attributable to the fact that the large stress necessary to enable power-law breakdown exceeds the range of the test system.

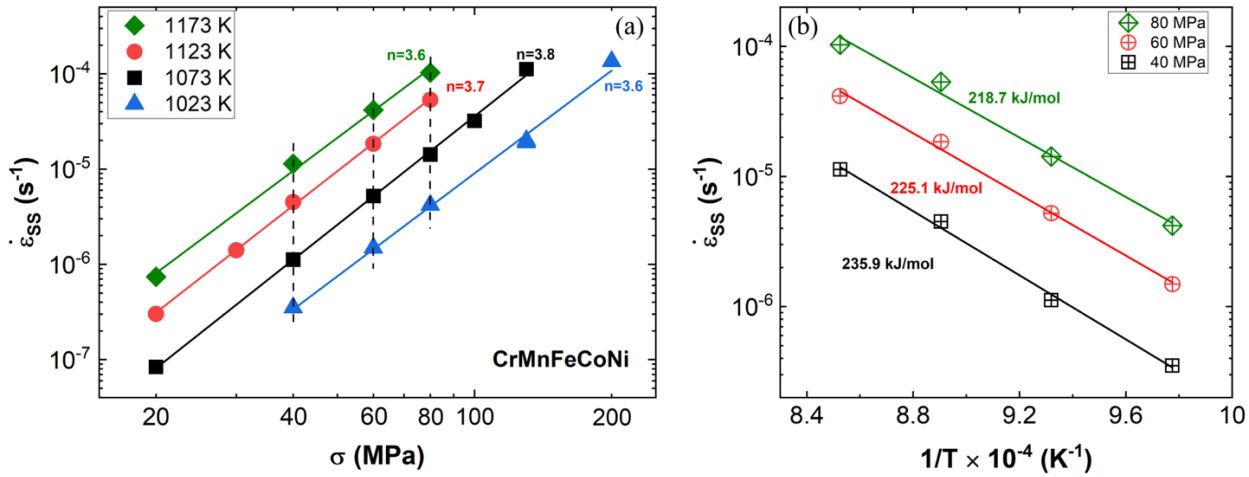

Fig. 5-3(a) Double logarithmic plot of steady-state creep rate versus applied stress for CrMnFeCoNi tested from 1023 K to 1173 K at 50 K intervals; (b) Arrhenius plot that shows the temperature dependence of steady-state creep rate at three isostresses of 80, 60 and 40 MPa. The calculated activation energies of creep are also labeled on the plot.

Table 5-2 A comparison of existing creep data for CrMnFeCoNi.

Studies	n	Q_c (kJ/mol)	T range (K)	σ range (MPa)
This study	~3.7	~230	1023 - 1173	20 - 200
Dobeš, *et al.* [8]	~6.3	246 704	973 - 1023 1023 - 1073	10 - 85
He, *et al.* [17] (High T tensile test)	~3 (low σ) ~5 (high σ)	284 333	1023 - 1123	~7 - 300
Cao, *et al.* [11]	~5.5 (medium high σ) >8 (high σ)	~270 ~400	773 - 873	130 - 400
Kang, *et al.* [12]	~6 (low σ) ~3 (medium low σ)	~310 ~250	808 - 923	20 - 100

Interestingly, our results show disagreement when compared to existing studies performed at comparable temperatures. He, *et al.* [17] conducted high temperature tensile tests and reported the transition from viscous glide to dislocation climb using a CrMnFeCoNi alloy that has a similar grain size (12 – 32 μm) and was tested under similar conditions. Dobeš, *et al.* [8] discovered a uniform but higher stress exponent ~6.3 in compression creep tests of an ultrafine-grained CrMnFeCoNi. Both studies performed several stress (or strain rate) jumps in each test and obtained multiple steady-state values. Load history and insufficient strain to reach a true steady state may affect the reported values. The results of He, *et al.* are further complicated by the fact that oxygen was transported through surface cracks in the later stages of creep, resulting in the formation of oxide particles within the material. These difficulties were avoided in our study, since only one stress was applied for each sample and tests were conducted in vacuum to tertiary creep.

In order to explore the possible causes and implications of the above interpretation, a characterization of steady-state creep microstructure is provided in the current investigation. Figure 4(a) shows the EBSD inverse pole figure (IPF) map of a sample crept at 1073 K and 100 MPa and interrupted at steady state. No obvious change in grain size was observed compared to the undeformed state shown in Figure 1(a). The orientation distribution of pixels is displayed in the color key, which demonstrates that the extent of texture formation during creep is very small. A smaller area was scanned using a finer step size (~0.2 μm), and the resulting IPF map and its corresponding kernel average misorientation (KAM) map are shown in Figure 4(b) and (c). The KAM map shows that, within the grains, most regions have misorientations <0.3°. Few boundary-like contrasts in the interior of grains are visible with a misorientation of ~0.7°, which is well below the >1.5° misorientation for well-defined subgrains reported during creep of class M and ODS metals [21, 28, 29]. It is also questionable whether they are subgrain boundaries because the misorientation is too small to be considered accurate for conventional EBSD technique that typically has an angular resolution ~0.5° [30]. This observation supports our earlier hypothesis that creep is partially controlled by lattice glide resistance, where subgrain boundaries are difficult to form due to slow recovery [31, 32].

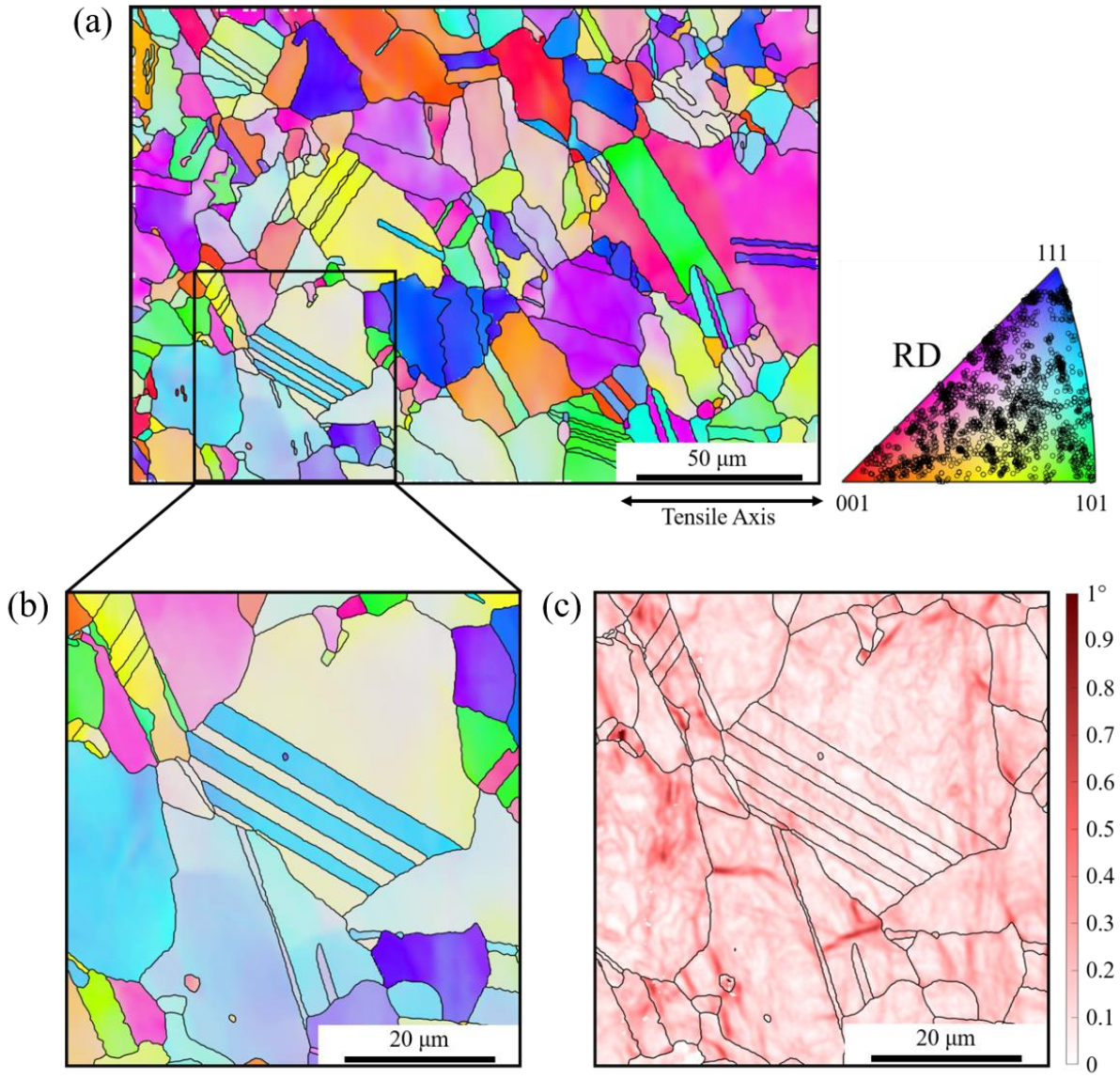

Fig. 5-4(a) EBSD IPF map (referenced to the rolling direction) of CrMnFeCoNi crept at 1073 K and 100 MPa taken at a step size of 0.8 µm. The tensile axis of creep is horizontal in this figure. The circle markers on the IPF color key give the distribution of the orientations of pixels; (b) an expanded view of a small region in (a) with a finer step size ~0.2 µm to characterize the misorientation in grain interiors; and (c) the KAM map for (b).

A further verification was carried out by TEM on the same sample in which no subgrain boundary formation was observed. Fig. 5-5a shows high dislocation density and severe entanglement within the grain interior, and the $(\bar{1}11)$ slip trace is visible, signifying easy dislocation glide. The dislocation substructure closely resembles that of low and room temperature deformation under similar plastic strain [33], although stacking faults and deformation twins were not observed here. In addition, the dislocation substructure is similar to that during creep at intermediate temperatures (773-873 K) [11], despite being less curved and more entangled, indicating a lesser extent of dislocation-lattice interaction and a greater extent of dislocation-dislocation interaction, which is a natural result of increasing temperature. We examined multiple grains, and these observations are representative. With reference to the normal primary region observed for CrMnFeCoNi, the absence of subgrain boundaries suggests that the decrease in mobile dislocation density during primary creep represents the formation of dislocation forests or dynamic recovery, or a combination of both.

It is interesting to compare the primary creep of CrMnFeCoNi with conventional class A alloys (e.g. Al-Mg alloys), in which subgrains do not form either. Class A alloys show an "inverted" primary creep, where the creep rate accelerates to steady state by the increase of mobile dislocation density under stress. It appears that the dislocation density in CrMnFeCoNi is much higher than in Al-Mg alloys under a similar modulus compensated applied stress, as the dislocations in the latter feature a random distribution with little entanglement [34, 35]. Therefore, it can be concluded that dislocation multiplication in CrMnFeCoNi is more rapid than in class A alloys during primary creep, while dislocation rearrangement in CrMnFeCoNi is more restricted than in class M alloys, as the subgrains do not form.

Fig. 5b shows a low dislocation density region of the same creep specimen, where various dislocation configurations can be found. The arrows indicate a dislocation multijunction (arrow 1), and jogs with small (arrows 2) and large (arrows 3) step sizes. These features suggest multiple other possible deformation mechanisms than dislocation-lattice interaction and forest dislocation cutting such as unzipping of multijunctions and dragging of jogs.

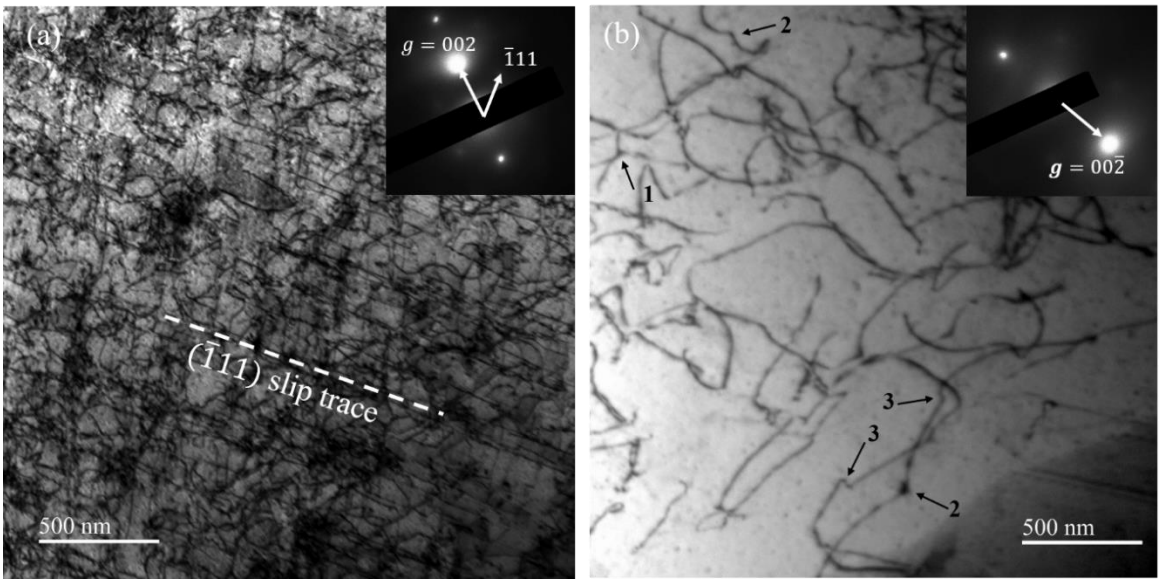

Fig. 5-5 TEM micrographs showing the steady-state dislocation substructures of CrMnFeCoNi crept at 1073 K and 100 MPa: (a) high density dislocation forest within the grain interior, where $(\bar{1}11)$ slip trace is also visible; and (b) a low dislocation density region in the same specimen exhibiting various dislocation configurations, which are as indicated by the black arrows — arrow 1: a dislocation multijunction; arrows 2: small jogs; and arrows 3: large jogs. The sample was aligned to [110] zone axis and tilted to two-beam conditions described by the g vectors shown in the selected area diffraction patterns.

The findings in our study provide important information and raise important questions with implications for understanding creep of MPEAs. Since CrMnFeCoNi exhibits characteristics of dislocation-lattice and dislocation-dislocation interactions and these mechanisms cannot be separated at high temperatures by constant stress creep tests, additional efforts are needed to decouple them and quantitatively describe their contributions. One promising way is to conduct stress reduction creep tests and study the stress dependence of the activation area. In addition, the origin of dislocation-lattice interactions remains unknown, as solute atmospheres do not exist in the current MPEA. Beyond speculation of dislocations directly interacting with SRO or nanoclusters, another important feature of MPEAs may also play an important role: Ding, *et al.* [36] showed a wide fluctuation of the stacking fault energies on the glide plane due to local ordering, and therefore sites with low stacking fault energies may become pinning sites. Furthermore, the similarity of room temperature and elevated temperature dislocation arrangements suggest that other strengthening effects caused by the compositional complexity and atomic randomness of the MPEAs as described recently by Basu and De Hosson and George *et al*. may contribute to the deformation at high temperatures [37, 38]. Therefore, a significant amount of future work should be directed to uncovering the origin of dislocation-lattice interactions, since this mechanism remains important from room to high temperatures.

5.4 Conclusions

To conclude, by performing tensile creep tests on CrMnFeCoNi at 1023-1173 K, we obtained consistent stress exponents (~3.7) and apparent activation energies (~230 kJ/mol) across all temperatures tested. Unlike observations from some other studies, no transition of rate-controlling creep mechanisms was observed. The activation energy of creep is slightly lower

than that of bulk vacancy diffusion measured in tracer experiments and decreases with increasing applied stress. EBSD and TEM observations on the steady-state creep microstructure revealed no subgrain boundary formation, which is characteristic of class M metals. Dense dislocation arrays, similar to those observed at lower temperatures, were observed in some regions while others exhibited more widely spaced interacting dislocations. Based on the evidence above, it is believed that creep of CrMnFeCoNi of intermediate grain size at high temperatures is determined by both dislocation-lattice and dislocation-dislocation interactions.

Acknowledgements

The authors are sincerely grateful to Dr. G. R. K. Yaddanapudi for his TEM work performed at the University of California, Davis and Prof. J. K. Mason for fruitful discussions. Research at ORNL (materials synthesis and processing) was supported by the U.S. Department of Energy, Office of Science, Basic Energy Sciences, Materials Sciences and Engineering Division. Research at UC Davis did not receive any specific grant from funding agencies in the public, commercial, or not-for-profit sectors.

References

[1] B. Cantor, I.T.H. Chang, P. Knight, A.J.B. Vincent, Mater. Sci. Eng., A 375-377 (2004) 213-218.
[2] J.W. Yeh, S.K. Chen, S.J. Lin, J.Y. Gan, T.S. Chin, T.T. Shun, C.H. Tsau, S.Y. Chang, Adv. Eng. Mater. 6(5) (2004) 299-303.
[3] G. Laplanche, S. Berglund, C. Reinhart, A. Kostka, F. Fox, E.P. George, Acta Mater. 161 (2018) 338-351.
[4] M. Laurent-Brocq, A. Akhatova, L. Perrière, S. Chebini, X. Sauvage, E. Leroy, Y. Champion, Acta Mater. 88 (2015) 355-365.
[5] N.L. Okamoto, S. Fujimoto, Y. Kambara, M. Kawamura, Z.M. Chen, H. Matsunoshita, K. Tanaka, H. Inui, E.P. George, Sci. Rep. 6 (2016) 35863.
[6] B. Gludovatz, A. Hohenwarter, D. Catoor, E.H. Chang, E.P. George, R.O. Ritchie, Science 345(6201) (2014) 1153-8.

[7] Z. Zhang, M.M. Mao, J. Wang, B. Gludovatz, Z. Zhang, S.X. Mao, E.P. George, Q. Yu, R.O. Ritchie, Nat. Comm. 6 (2015) 10143.
[8] F. Dobeš, H. Hadraba, Z. Chlup, A. Dlouhý, M. Vilémová, J. Matějíček, Mater. Sci. Eng., A 732 (2018) 99-104.
[9] M. Zhang, S.E. Broyles, J.C. Gibeling, Acta Mater. 196 (2020) 384-395.
[10] P. Susila, D. Sturm, M. Heilmaier, B.S. Murty, V.S. Sarma, J. Phys,: Conf. Ser. 240 (2010) 012090.
[11] C. Cao, J. Fu, T. Tong, Y. Hao, P. Gu, H. Hao, L. Peng, Entropy 20(12) (2018).
[12] Y.B. Kang, S.H. Shim, K.H. Lee, S.I. Hong, Mater. Res. Lett. 6(12) (2018) 689-695.
[13] E.J. Pickering, R. Muñoz-Moreno, H.J. Stone, N.G. Jones, Scr. Mater. 113 (2016) 106-109.
[14] F. Otto, A. Dlouhý, K.G. Pradeep, M. Kuběnová, D. Raabe, G. Eggeler, E.P. George, Acta Mater. 112 (2016) 40-52.
[15] K.H. Lee, S.-K. Hong, S.I. Hong, Materialia 8 (2019).
[16] O.D. Sherby, P.M. Burke, Prog. Mater. Sci. 13 (1968) 323-390.
[17] J.Y. He, C. Zhu, D.Q. Zhou, W.H. Liu, T.G. Nieh, Z.P. Lu, Intermetallics 55 (2014) 9-14.
[18] F. Otto, A. Dlouhý, C. Somsen, H. Bei, G. Eggeler, E.P. George, Acta Mater. 61(15) (2013) 5743-5755.
[19] M.W. Decker, J.R. Groza, J.C. Gibeling, Mater. Sci. Eng., A 369(1-2) (2004) 101-111.
[20] L.G. Vettraino, M. Zhang, J.L.W. Carter, J.R. Groza, J.C. Gibeling, Mater. Sci. Eng., A 756 (2019) 538-544.
[21] S.E. Broyles, M. Zhang, J.C. Gibeling, Mater. Sci. Eng., A 779 (2020) 139112.
[22] ASTM E1382-97(2015), Standard Test Methods for Determining Average Grain Size Using Semiautomatic and Automatic Image Analysis, ASTM International, West Conshohocken, PA, 2015.
[23] F. Bachmann, R. Hielscher, H. Schaeben, Solid State Phenom. 160 (2010) 63-68.
[24] F. Otto, N.L. Hanold, E.P. George, Intermetallics 54 (2014) 39-48.
[25] O.D. Sherby, R.H. Klundt, A.K. Miller, Metall. Mater. Trans. A 8(6) (1977) 843-850.
[26] F.A. Mohamed, T.G. Langdon, Acta Metall. 22(6) (1974) 779-788.
[27] M. Vaidya, K.G. Pradeep, B.S. Murty, G. Wilde, S.V. Divinski, Acta Mater. 146 (2018) 211-224.
[28] B. Sonderegger, S. Mitsche, H. Cerjak, Mater. Sci. Eng., A 481-482 (2008) 466-470.
[29] F.J. Humphreys, J. Microsc. 213(3) (2004) 247-256.
[30] F.J. Humphreys, J. Mater. Sci. 36 (2001) 3833-3854.
[31] P. Yavari, F.A. Mohamed, T.G. Langdon, Acta Metall. 29(8) (1981) 1495-1507.
[32] P. Yavari, T.G. Langdon, Acta Metall. 30(12) (1982) 2181-2196.
[33] G. Laplanche, A. Kostka, O.M. Horst, G. Eggeler, E.P. George, Acta Mater. 118 (2016) 152-163.
[34] R. Horiuchi, M. Otsuka, Trans. Jpn. Inst. Met. 13(4) (1972) 284-293.
[35] M.J. Mills, J.C. Gibeling, W.D. Nix, Acta Metall. Mater. 33(8) (1985) 1503-1514.
[36] J. Ding, Q. Yu, M. Asta, R.O. Ritchie, P. Natl. Acad. Sci. 115(36) (2018) 8919.
[37] I. Basu, J.T.M. De Hosson, Scr. Mater. 187 (2020) 148-156.
[38] E.P. George, W.A. Curtin, C.C. Tasan, Acta Mater. 188 (2020) 435-474.

Chapter 6 Elevated-temperature Deformation Mechanisms in a CrMnFeCoNi High-Entropy Alloy[1]

6.1 Introduction

The recent development of high-entropy alloys (HEAs) and medium-entropy alloys (MEAs), together also known as multi-principal element alloys (MPEAs), opens great potential to design new alloys with desirable mechanical properties that can meet the challenges of serving under extreme conditions [1-4]. A primary example class among all MPEAs is the CrCoNi-based single phase FCC alloys that have been shown to possess excellent strength and ductility from room temperature down to cryogenic temperatures [5, 6]. In the high temperature regime, despite having superior oxidation and corrosion resistance and lower cost compared to their BCC refractory counterparts, these alloys are known to have inadequate strength that inhibits their direct utility in high temperature applications. However, the advent of oxide dispersion-strengthened (ODS) MPEAs and high-entropy superalloys (HESAs) [7-9] with CrCoNi-based FCC matrices, has enabled an increase in strength to that comparable to Inconel and Ni-based superalloys and revealed that the mechanical properties of particulate-strengthened alloys with an MPEA matrix can surpass those with a pure metal or dilute alloy matrix. These discoveries immediately suggest the need for a systematic understanding of deformation mechanisms in the unique FCC MPEA matrix at elevated temperatures, as it is the prerequisite for constructing physics-informed models for more complicated particle strengthened MPEAs.

[1]In press as M. Zhang, E.P. George, J.C. Gibeling, *Acta Mater.* (2021)

A detailed understanding of plastic deformation in the MPEAs relies on the identification of the rate-controlling deformation mechanisms and a quantitative description of the dependence of flow properties on strain rate, stress and temperature. For metallic materials, these two aspects can be described within the framework of thermally activated dislocation glide [10], where the rate of deformation is controlled by the rate at which dislocations overcome critical obstacles by thermally activated processes. Therefore, the most general form of the plastic strain rate, $\dot{\varepsilon}$, can be written as:

$$\dot{\epsilon} = \dot{\epsilon}_0 exp\left(-\frac{\Delta G}{k_B T}\right) \tag{6.1}$$

where $\dot{\epsilon}_0$ is the reference strain rate, ΔG is the Gibbs free energy of activation, k_B is the Boltzmann constant, and T is the absolute temperature. ΔG can be further written as:

$$\Delta G = \Delta F - \Delta W = \Delta F - \frac{\sigma b \Delta a''}{M} \tag{6.2}$$

where ΔF is the Helmholtz free energy of activation, ΔW is the external work done by the applied stress, σ is the applied normal stress, b is the magnitude of the Burgers vector, $\Delta a''$ is the activation area, and M is the Taylor factor (3.06 for a randomly oriented polycrystalline FCC metal [11]). We apply the original notation from Kocks, Argon, and Ashby [10], $\Delta a''$, to denote the measurable operational activation area in experiments. We also note that in literature, σ is sometimes used to represent shear stress. For clarity, σ in this paper always refers to normal stress and will be converted to shear stress by dividing by M where necessary (as in Eqn. 6.2). ΔF describes the total energy needed for the dislocations to overcome the obstacles, which is the sum of the mechanical work done, ΔW, and the energy provided by thermal activation, ΔG. It can be

inferred from Eqn. 6.2 that ΔF is only a function of the nature of obstacles and corresponding activation events, whereas ΔG is directly stress dependent.

The activation area, $\Delta a''$, is critical for the determination of the deformation mechanism(s) because it can be related to the area swept by the dislocations during activation events and thus gives the length scale of the spacing of the obstacles. In addition, the relationship between $\Delta a''$ and the applied stress, plastic strain, or composition reflects the stress, strain, or composition dependence of the microstructure, which can then be compared to that of well-known mechanisms. For example, $\Delta a'' \sim 1\ b^2$ for diffusive processes and lattice friction [12, 13], $\Delta a'' \sim 100\ b^2$ and scales inversely with solute concentration for dislocation-solute interactions in the dilute limit [14], and $\Delta a'' \sim 1000\ b^2$ and scales inversely with applied stress (or plastic strain) for forest dislocations [15]. Operationally, $\Delta a''$ can be determined by initiating a change in stress or strain rate when deforming the material and recording the instantaneous response of the other quantity:

$$\Delta a'' = \frac{M k_B T}{b} \cdot \left. \frac{\partial \ln \dot{\epsilon}}{\partial \sigma} \right|_{T, \hat{\sigma}_i} \tag{6.3}$$

We highlight that $\Delta a''$ must be determined under constant microstructure described by the flow strengths of i features, $\hat{\sigma}_i$ (e.g., forest dislocation spacing, subgrain size) because the partial derivative of the logarithmic strain rate $\dot{\epsilon} = \dot{\epsilon}(\sigma, T, \hat{\sigma}_i)$ with respect to σ must be evaluated at constant T and $\hat{\sigma}_i$. Even though truly keeping $\hat{\sigma}_i$ constant is virtually impossible, data acquisition with high time resolution should take place quickly after the strain rate or stress change when the change in microstructure is still small.

Despite the abundance of experimental work performed to characterize the mechanical properties and deformation microstructure in the CrCoNi-family, detailed mechanistic studies using the above framework have been rather rare. Hong, *et al.* [16] carried out strain rate jump tests on a CrMnFeCoNi MPEA at room temperature and measured $\Delta a''$ to be ~100 b^2, which they attributed to the interaction between dislocations and nanoscale clusters, including short-range order (SRO). Wu, *et al.* [17] performed the same tests on CrMnFeCoNi at both room and cryogenic temperatures and reported an $\Delta a''$ on the order of ~100 b^2 at 293 K and ~10 b^2 at 77 K. They applied the Labusch-type strengthening analysis and concluded that the deformation is dominated by long-range bowing of curved dislocations coupled with some short-range effects. Laplanche, *et al.* [18] conducted a series of load relaxation tests on CrMnFeCoNi from 77 K to 423 K and obtained $\Delta a''$ values from ~100 b^2 to ~500 b^2, an increasing trend of $\Delta a''$ with temperature, and a decreasing trend of $\Delta a''$ with plastic strain. They discovered that the flow behavior in CrMnFeCoNi is controlled by a combination of rate-dependent Hall-Petch strengthening, solid solution hardening, and forest dislocation hardening, which appears to be similar to conventional alloys. More importantly, they were able to quantitatively separate the contributions of these mechanisms by using existing hardening models, including a recent model that predicts the flow strength in concentrated random solid solutions and MPEAs given by Varvenne, *et al.* [19, 20]. Therefore, a critical question is whether the same or similar attributes of plastic deformation for CrCoNi-based MPEAs at cryogenic and room temperatures apply at elevated temperatures for creep deformation or there exist other mechanisms (e.g., diffusion and recovery related mechanisms) that control the rate instead. Unfortunately, quantitative mechanistic studies that provide the answer to this question have not been available to date, even though limited creep and high temperature tensile and nanoindentation data are available [8, 21-25]. In our

recent study [23] on the steady-state creep behavior of CrMnFeCoNi, we identified a uniform stress exponent of 3.7 ± 0.1 and an activation energy lower than that for lattice self-diffusion. We concluded that the creep mechanisms are likely to be controlled by dislocation-lattice interactions (concentrated solid solution hardening) and dislocation-dislocation interactions (forest dislocation hardening). Therefore, the main goals of the present study are to mechanically verify whether these two mechanisms are indeed both controlling the rate of deformation in the FCC MPEA matrix and if so, to separate their contributions. To avoid the difficulties in obtaining high quality data by strain rate jump tests and stress relaxation tests at elevated temperatures due to the limitations of extensometry and the oxidation of the material, we conducted stress reduction creep tests in a vacuum creep furnace equipped with in-situ extensometry that provides microstrain resolution and fast data acquisition that provides microsecond time resolution to record the strain rate response of the material to the stress change. The same test equipment and procedure have previously provided mechanistic insights in numerous pure metals and dispersion-strengthened alloys [26-29].

In the present study, we select the well-characterized FCC HEA, CrMnFeCoNi, to generate comparisons with existing data and current theories describing this material. We report on the results from multiple stress reduction creep experiments from different initial stresses. Since uniform stress exponents were found from 1023 K to 1173 K in our recent study [23], indicating no clear change of deformation mechanisms, we select a single temperature of 1073 K and focus on the stress and strain rate dependence of the flow properties. The CrMnFeCoNi is known to remain single phase at this temperature, thereby enabling us to study the properties of the FCC HEA matrix [30]. At lower temperatures, additional phases are known to form during long-term

creep tests [31] leading to dislocation/particle interactions that complicate determination of the role of the matrix in controlling creep. In addition, we measure the values and the stress dependence of the activation area, which then lead to the determination of the deformation mechanisms. Finally, we quantitatively separate the contributions from multiple controlling mechanisms and give a constitutive equation to describe the steady-state creep behavior of CrMnFeCoNi.

6.2 Experimental

An equiatomic CrMnFeCoNi alloy was produced by arc-melting, drop-casting, and cold rolling using similar procedures to those described in Ref. [32]. The constituent elements were arc-melted five times, and the button was flipped between each melt to promote homogeneous melting. Afterwards, it was drop-cast into a 19 × 25.4 × 127 mm^3 copper mold and homogenized in vacuum at 1473 K for 24 h. The material was then cold rolled to a thickness of 0.64 mm (~ 97% reduction in thickness) and a width of 30 mm. Flat creep specimens having gauge sections of 19.05(L) × 2.54(W) × 0.64(H) mm^3 were cut from the as-rolled sheets by electrical discharge machining (EDM). The specimens were annealed in a vacuum furnace at 1173 K for 1 h to reach a completely recrystallized state. The heat treatment produces a single phase FCC alloy with an initial microstructure as shown in Fig. 6-1 consisting of randomly oriented equiaxed grains with an average size of 21±11 μm with a lognormal distribution. This observation is consistent with the characterization of the initial microstructure for cold rolled and annealed CrMnFeCoNi in multiple other studies [32-34], where recrystallized equiaxed grains with a large number of annealing twins and low dislocation density were observed. The samples were polished by 320

and 600 grit SiC abrasives before creep testing to alleviate the potential influence of surface effects on the creep measurements.

Stress reduction creep tests were performed on a true stress-controlled creep machine under vacuum ($\leq 2 \times 10^{-5}$ torr) at 1073 K using the same procedures as in our previous studies [27-29]. The test temperature of 1073 K was chosen because at and above this temperature, the FCC single phase has been shown to be stable, and the formation of second phases known to be present at lower temperatures (e.g. Cr-rich σ phase, NiMn phase) is believed to be negligible [30, 35, 36]. Creep strain was measured directly at the specimen inside the furnace by a Schaevitz 250 MHR linear variable differential transformer (LVDT) utilizing a custom quartz tube and rod fixture as described in Ref. [37]. Constant true stress was maintained throughout the tests using an Andrade-Chalmers lever arm [38] except for one abrupt stress reduction for each sample. The creep samples were first loaded with an initial stress, σ_{in}, to secondary creep which produces a steady-state creep rate of $\dot{\epsilon}_A$. Here, we follow the notation used in Biberger and Gibeling [39] to describe the stresses and creep rates at different stages before and after the stress reduction. After reaching the first steady state, a stress reduction was performed by manually removing part of the load from the arm. Generally, the stress reduction was carried out at ~10% plastic strain for large initial stresses and ~5% for small initial stresses. The forward creep rate immediately after the stress reduction, termed $\dot{\epsilon}_C$, was recorded with fast data acquisition with microstrain and microsecond resolution. $\dot{\epsilon}_C$ is usually termed "constant structure" creep rate because at this stage the change in microstructure is minimal. Therefore, it is the proper strain rate to use in Eqn. 6.3. Subsequently, the samples continued to deform under the reduced stress, σ_{red}, to a second steady state with a creep rate of $\dot{\epsilon}_D$, during which stage the tests were terminated. In order to exclude

any possible load history effects on the microstructure and the creep rates, only one stress reduction was conducted on each sample. In addition, large stress reductions (>60%) were avoided to reduce the likelihood of domination by dynamic recovery. The values of σ_{in} and σ_{red} used in this study are listed in **Table 6-1**.

Electron backscatter diffraction (EBSD) was conducted on a FEI Scios Dualbeam FIB SEM at an operating voltage of 15 kV to investigate the microstructure of CrMnFeCoNi before creep testing. Raw data were post-processed by an open-source toolbox MTEX (version 5.4.0) in Matlab [40] following the same procedures as in Ref. [41]. The EBSD samples were prepared by conventional grinding and polishing down to 0.3 μm alumina and then polishing on a Buehler Vibromet 2 vibratory polisher with 0.05 μm colloidal silica for 4 h.

Transmission electron microscopy was performed on a JEOL 2100F-AC TEM to characterize the dislocation substructure under steady-state creep deformation at an accelerating voltage of 200 kV. The TEM specimens were prepared by conventional pre-thinning techniques including grinding, 3 mm disc punching, polishing and dimpling. Final perforation was carried out by a Fischione 1050 TEM ion mill operating at 5kV, which was then followed by a final polishing at 1 kV for 30 minutes and 0.5 kV for an hour to alleviate ion beam damage.

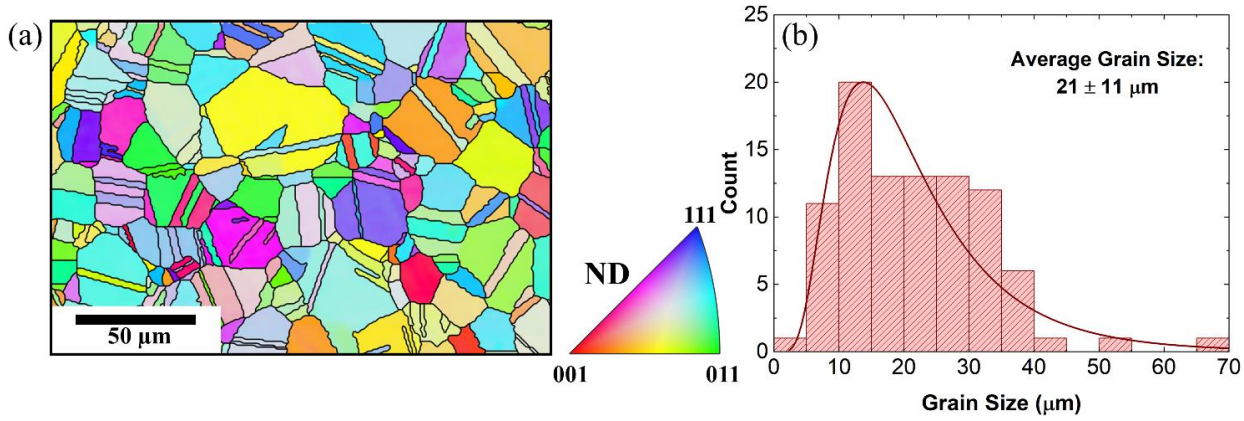

Fig. 6-1(a) EBSD inverse pole figure (IPF) map of the microstructure of CrMnFeCoNi after annealing at 1173 K for 1 h before creep testing; (b) A histogram for the grain sizes measured from EBSD data. The red curve shows the lognormal fit to the histogram.

Table 6-1 Initial and reduced stresses used in the stress reduction creep experiments.

σ_{in} (MPa)	σ_{red} (MPa)
160	144, 130, 120, 112, 96
130	120, 100, 90, 80, 60
100	90, 80, 70, 60, 50
80	76, 72, 64, 56, 48
60	54, 48, 45, 42, 36

6.3 Results and Discussion

6.3.1 Primary Creep

Fig. 6-2 gives representative creep curves up to ~2% true plastic strain to show the primary creep for CrMnFeCoNi loaded under σ_{in} at 1073 K. Due to the large difference in strain rates under different stresses, Fig. 6-2 is separated into (a) for large stresses and (b) for intermediate and small stresses for better visibility. Overall, primary creep for CrMnFeCoNi is very brief — up to only ~1-2% plastic strain — compared to FCC pure metals (~10-30% [42, 43]) and conventional class M and class A alloys (~10-50% [44, 45]) at similar modulus-compensated stresses. The short primary can be attributed to the rather featureless steady-state creep microstructure revealed by recent TEM investigations on CrMnFeCoNi [21, 23]. Unlike pure metals and class M alloys, CrMnFeCoNi does not form subgrains during creep deformation. The solute drag behavior characteristic of class A alloys is also not evident judged by its high dislocation density. Without the formation of these substructures during primary creep, the HEA is able to reach steady-state deformation quickly.

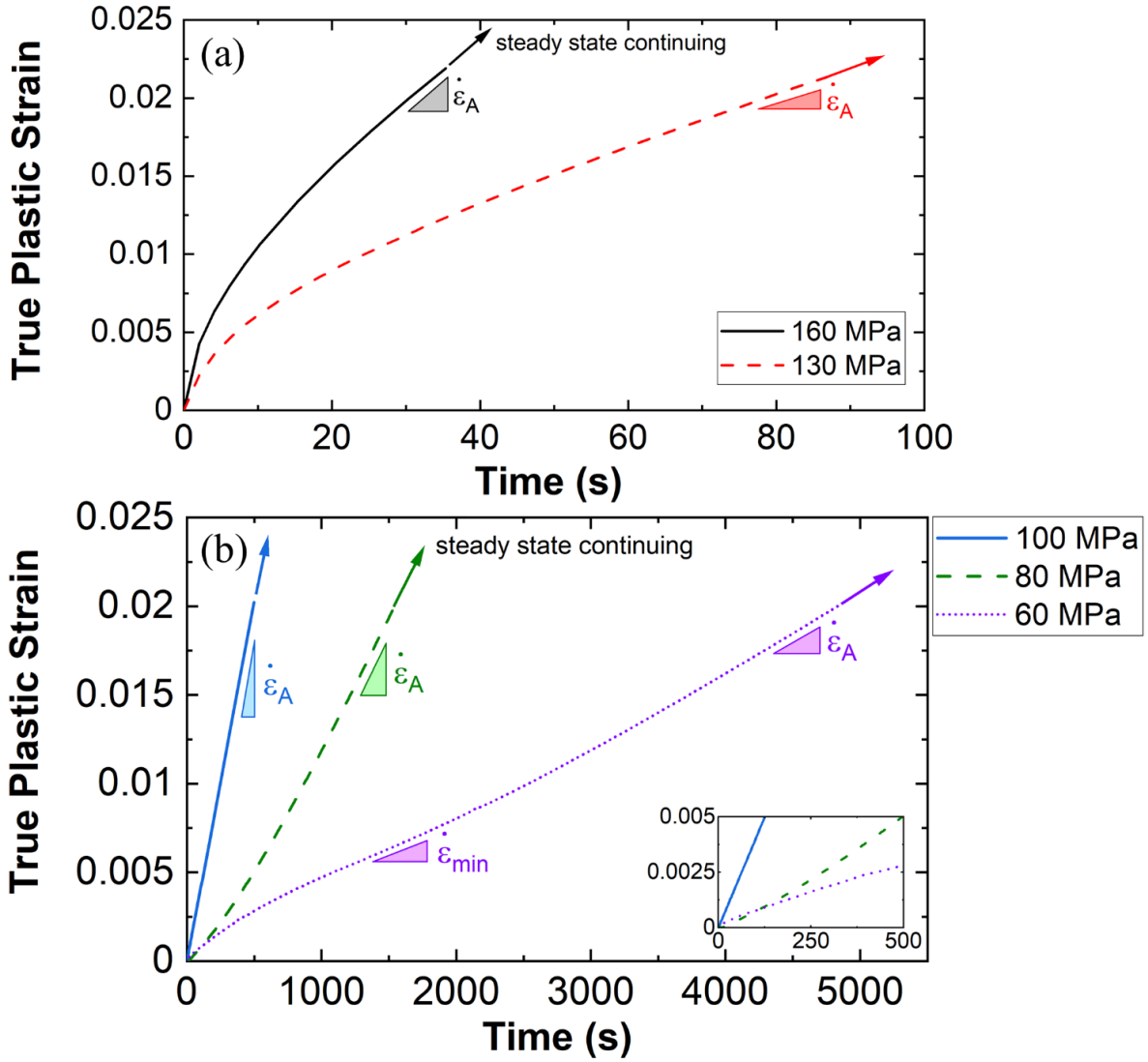

Fig. 6-2 Example creep curves showing primary creep of CrMnFeCoNi samples crept at 1073 K under applied stresses of (a) 160 and 130 MPa; and (b) 100, 80, and 60 MPa up to ~2% true plastic strain. The inset in (b) provides a closer view of the creep curves in the first 0.5% plastic strain. The arrows in the figure indicate the continuation of steady-state deformation under the creep rate of $\dot{\epsilon}_A$.

Fig. 6-2 also shows interesting trends in primary creep for samples deformed at different stresses.

Normal primary creep (creep decelerates to steady state) is present for the large stresses (160 and

130 MPa), yet the shape changes for the low stresses. At 100 MPa, no primary is evident, and the sample deformed directly into steady state. At 80 MPa, the primary becomes inverted (creep accelerates to steady state), and at 60 MPa, the creep rate first decreases then increases to its steady-state value. Interestingly, these trends were not shown in our previous study of CrMnFeCoNi [23], where primary was found to be normal for all these stresses at 1073 K. Because both materials had nearly the same grain size and were annealed under the same conditions, this difference must be related to subtle differences in the initial microstructure, as the material in our previous study was rolled to a slightly larger thickness (~1 mm, 95% thickness reduction). Since primary creep is controlled by the competition between work hardening and recovery [46, 47], it depends strongly on the initial dislocation substructure and density. It appears that primary creep in CrMnFeCoNi has a complicated stress dependence where multiple factors with comparable contributions act in combination. Since we are mostly interested in the stress reduction creep behavior that occurred thereafter, a thorough investigation of the primary creep is beyond the scope of the current paper and will be explored in future work. Meanwhile, here we show that the difference in primary creep does not affect the steady-state creep rate of the material. As displayed in Fig. 6-3, excellent agreement was obtained for the steady-state creep data in both this study and our previous study [23] with a common stress exponent ~3.7.

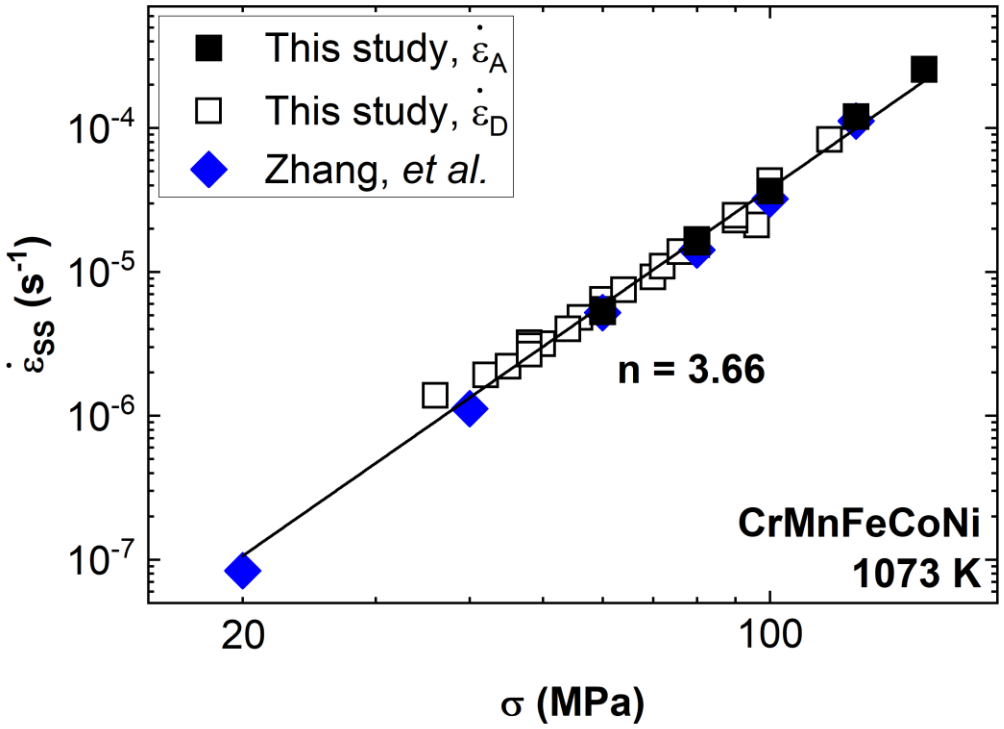

Fig. 6-3 Double logarithmic plot of steady-state creep rate versus applied stress for CrMnFeCoNi tested at 1073 K. The solid square symbols correspond to the creep rates $\dot{\epsilon}_A$ during steady-state deformation under σ_{in} before stress reduction. The empty square symbols represent the creep rates $\dot{\epsilon}_D$ during steady-state deformation under σ_{red} after stress reduction. The creep data for CrMnFeCoNi tested at the same temperature reported by Zhang, *et al.* [23] are also included in this plot (solid diamonds) for comparison. The solid line is a linear fit through all data points shown in the figure. The coefficient of determination, R^2, of the linear fit is 0.99.

6.3.2 Stress Reduction Creep Behavior

Fig. 6-4 shows two example creep curves and their stress reduction transients for CrMnFeCoNi from a large σ_{in} of 160 MPa and a small σ_{in} of 60 MPa. The features exhibited in the two transients are representative for all stress reductions conducted in this study. The difference in their primary creep behavior was described in the previous section. A plateau region is present after the stress reduction, which is a consequence of the superposition of the anelastic backflow caused by the instantaneous backward slip of the mobile dislocations in response to the stress reduction and the forward flow under σ_{red} [48]. This behavior has been previously observed in pure metals and conventional alloys, and the backflow is rationalized by two potential mechanisms: the unbowing of dislocations due to a reduction of the forward stress or the relaxation of dislocation pile ups against grain boundary or subgrain boundary walls [48-51].

Since previous microstructural characterization of CrMnFeCoNi shows a high density of bowed dislocations in a clean matrix with no evidence of subgrains or large-scale dislocation pile-ups [23], the physical origin of the backflow can be attributed to the former mechanism. Recently, Bouaziz, *et al.* [52] discovered a strong Bauschinger effect in a CrMnFeCoNi alloy with a similar grain size through room temperature tension/compression tests, which can be partially related to the backflow behavior shown here. It is worth noting that the long duration of the plateau region (noticeably longer than pure metals [26, 27]) indicates a slow decay for the backflow immediately after a stress reduction. This is believed to be caused by the pinning effect of the "rough" HEA matrix, where the rate of dislocation unbowing can be slow. Unfortunately, it is difficult to separate the net forward flow in the plateau region at present because the stress and time dependent rate of backflow is not known. Nevertheless, since the plateau region is very

short compared to the time for the creep rate to finally evolve to $\dot{\epsilon}_D$ (<5%), the forward creep rate that immediately follows the plateau when anelastic backflow becomes negligible can still be taken as the constant structure creep rate, $\dot{\epsilon}_C$.

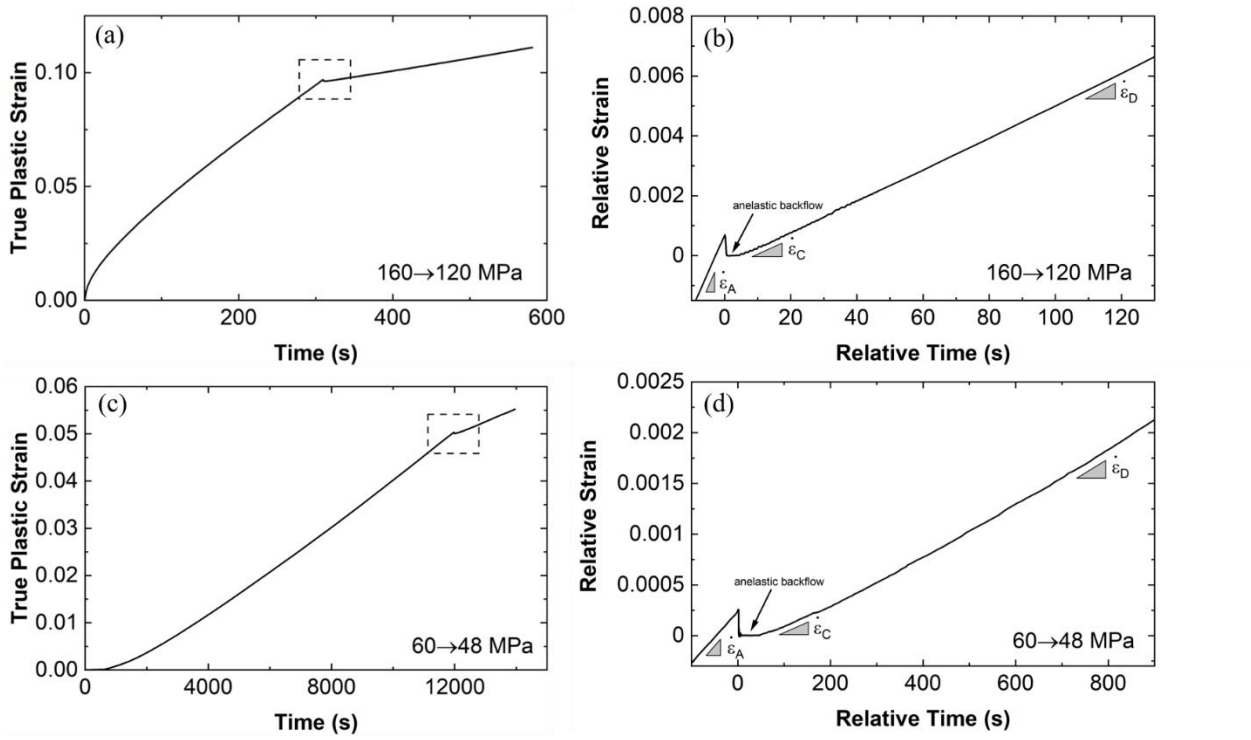

Fig. 6-4 Example creep curves for stress reduction experiments from (a) a large initial stress, 160 MPa; and (c) a small initial stress, 60 MPa to reduced stresses that give similar proportions of stress reductions. The creep tests were interrupted at steady-state deformation at the reduced stress. (b) and (d) are expanded views of the stress reduction transients in (a) and (c), respectively, as indicated by the dashed rectangles. The plateau regions in (b) and (d) show the anelastic backflow of the material following the stress reduction. The curves in (b) and (d) were shifted both horizontally and vertically such that the moment of stress reduction corresponds to zero time and the immediate strain after stress reduction corresponds to zero strain for better visibility and comparison.

The most prominent feature of the transient behavior for CrMnFeCoNi is the rapid rate of the microstructural evolution after a stress reduction (i.e., $\dot{\epsilon}_C$ transitions to $\dot{\epsilon}_D$ very quickly). For most pure metals and conventional alloys, this process takes hours for large stresses and days for small stresses due to the rather sluggish substructure rearrangement following stress reduction [53] (subgrain coarsening for pure metals and class M alloys and annihilation of dislocations pinned by solute atmosphere for class A alloys [26, 37]). In order to understand the origin of the short stress reduction transient, TEM was carried out to examine the steady-state creep microstructure. Fig. 6-5a shows a high-density distribution of curved and entangled dislocations within a grain interior with no subgrain formation, which is consistent with previous characterization of creep structures at elevated temperatures and even those in long-term creep at intermediate temperatures [23, 31]. A more detailed observation of the dislocation interactions is provided in Fig. 6-5b, where extensive lattice pinning (shown by black arrows) and dislocation junctions are present, suggesting combined effects of forest dislocations and concentrated solid solution hardening. Such dislocation substructure highlights the dominance of the pinning effect from the concentrated solid solution matrix at elevated temperatures, which suppresses recovery and other diffusion-related mechanisms (i.e. subgrain boundary formation and solute atmosphere migration) in the HEA. Therefore, the short stress reduction transient of CrMnFeCoNi, along with the brief primary creep, can be explained by the rapid formation and regulation of this relatively simple microstructure.

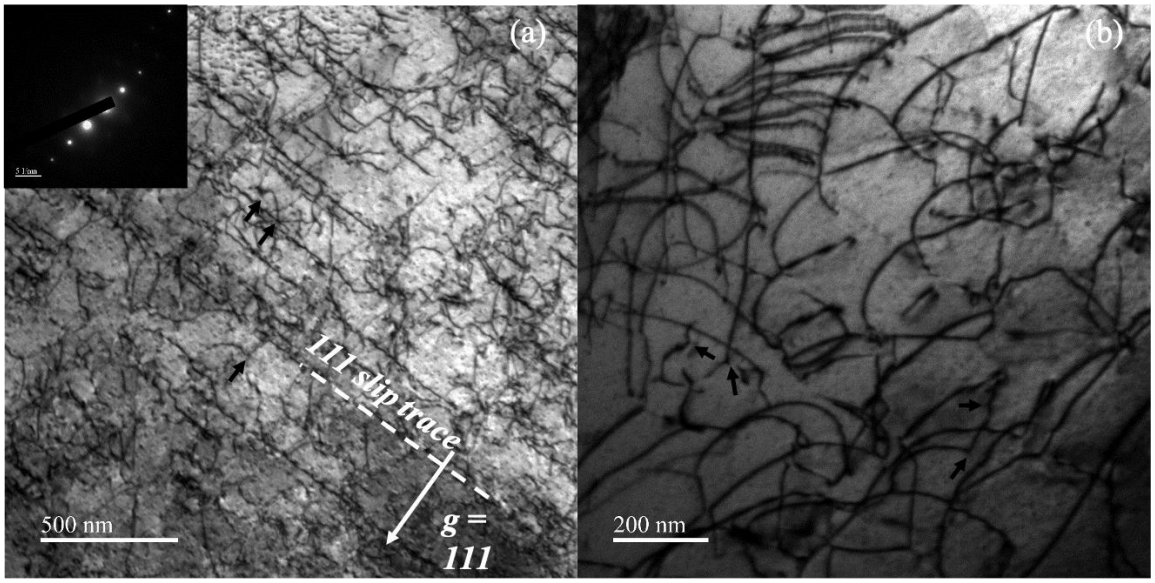

Fig. 6-5 TEM micrographs illustrating the representative dislocation substructure of CrMnFeCoNi during steady-state deformation: (a) high-density arrays of curved dislocations are present within the grain interior with visible (111) type slip trace and no evidence of subgrain boundary formation; and (b) a higher magnification image exhibiting extensive dislocation-lattice and dislocation-dislocation interactions. The black arrows indicate dislocations pinned by the high entropy matrix. The specific TEM specimen was taken from a creep sample crept at 1073 K and 100 MPa, interrupted at steady-state deformation ~ 10% plastic strain. The image was taken under [110] zone axis and [111] two beam condition.

Another important aspect of creep after a reduction of stress is the relative magnitude of $\dot{\epsilon}_C$ and $\dot{\epsilon}_D$ since they give additional insights into the evolution of the microstructure. For pure metals and class M alloys, $\dot{\epsilon}_C$ increases to $\dot{\epsilon}_D$ because the coarsening of the subgrains results in a softer microstructure. Under limited circumstances when the percentage of stress reduction is large, the creep rate will first decrease because of the domination of dynamic recovery and will then increase to $\dot{\epsilon}_D$ [54-56]. For class A alloys $\dot{\epsilon}_C$ decreases to $\dot{\epsilon}_D$ because the decrease in mobile dislocation density with time dominates [37]. In both cases, $\dot{\epsilon}_C$ differs from $\dot{\epsilon}_D$ by approximately one to two orders of magnitude [26, 27, 37]. The values of $\dot{\epsilon}_C$ and $\dot{\epsilon}_D$ for CrMnFeCoNi from all of our experiments are shown in Fig. 6-6. $\dot{\epsilon}_A$ is also included and overlaps with $\dot{\epsilon}_C$ for $\sigma = \sigma_{in}$ since $\dot{\epsilon}_A$ is actually a special type of $\dot{\epsilon}_C$ when the stress reduction is zero. We note that the $\dot{\epsilon}_D$ values for high σ_{red} in Fig. 6-6a (σ_{in} = 160 MPa) are absent because the second steady state cannot be distinguished from tertiary creep under such high stress.

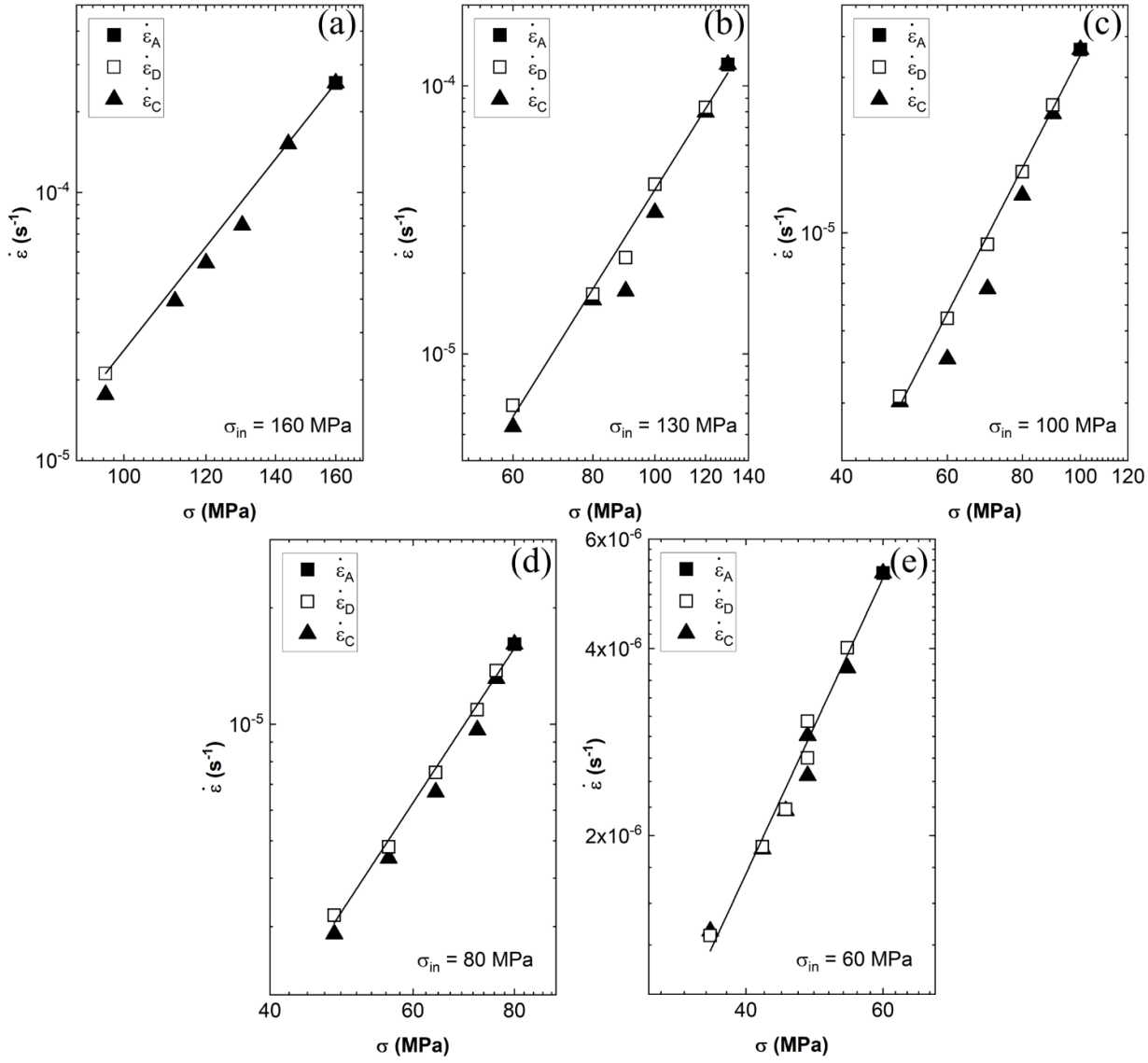

Fig. 6-6 Double logarithmic plots of creep rates $\dot{\epsilon}_A$, $\dot{\epsilon}_C$, and $\dot{\epsilon}_D$ versus applied stress for CrMnFeCoNi crept under initial stresses of (a) 160 MPa; (b) 130 MPa; (c) 100 MPa; (d) 80 MPa; and (e) 60 MPa at 1073 K. The solid line is a linear fit of the steady-state data $\dot{\epsilon}_A$ and $\dot{\epsilon}_D$ versus applied stress that delineates a power-law relationship.

It is evident that $\dot{\epsilon}_C$ is only slightly lower than $\dot{\epsilon}_D$ and the difference is much smaller than that observed in conventional alloys. Several important conclusions can be made from Fig. 6-6 : (i) Recovery mechanisms are not important for CrMnFeCoNi since otherwise $\dot{\epsilon}_C$ will be higher than $\dot{\epsilon}_D$; (ii) The stress reduction transient of CrMnFeCoNi resembles that of pure metals and class M alloys despite the fact that subgrains do not form in CrMnFeCoNi and therefore subgrain coarsening does not exist. The small difference between $\dot{\epsilon}_C$ and $\dot{\epsilon}_D$ is instead believed to be caused by the coarsening of the dislocation network and thus the increase of the forest dislocation spacing, which occurs quickly and has a subtle effect on the creep rate; (iii) the linear fit of the steady-state values ($\dot{\epsilon}_A$ and $\dot{\epsilon}_D$) on double-logarithmic axes also describes $\dot{\epsilon}_C$ reasonably. Hence, the small difference in $\dot{\epsilon}_C$ and $\dot{\epsilon}_D$ appears to permit the usage of steady-state creep rates in Eqn. 6.3. This means that an estimated and perhaps reliable activation area can be determined with constant-stress creep tests only and can be obtained in virtually all stress-controlled test machines; and (iv) the rapid microstructural evolution and its limited effect on creep rates after stress reduction leads to an almost perfect agreement between $\dot{\epsilon}_A$ and $\dot{\epsilon}_D$ in Fig. 6-3 above. This suggests that the steady-state creep rates for CrMnFeCoNi can be considered as a state variable of temperature and applied stress only and are essentially independent of load history. Therefore, our work also justifies the possibility of using of multiple stress changes in one test to obtain different steady-state values, as long as tertiary creep has not been reached. The above features are core to the creep properties of CrMnFeCoNi and have profound implications for the quantitative analysis of the deformation mechanisms given below.

The constant structure data from all initial stresses are concatenated in Fig. 6-7 to demonstrate the stress dependence of the stress reduction creep behavior of CrMnFeCoNi. Linear fits are

given on the semilogarithmic plot to delineate their exponential relationship described by Eqns. 6.1 and 6.2. The goodness of fit (R^2) for all linear fits is above 0.97, validating our current approach. Fig. 6-7 shows only a small stress dependence of the slopes as all data points roughly fall on the same line, although two trends can still be distinguished: (i) the slope of the lines increases for decreasing σ_{in}; and (ii) if all lines are extrapolated to the full stress range, the extrapolated line is lower for higher σ_{in}. That is, the creep rates under the same σ_{red} will be lower for samples subjected to higher σ_{in}. This phenomenon is most pronounced at 160 MPa, where the creep rates appear to be lower than the overall trend. The first observation is directly related to the activation area and is discussed in the next section. The second observation is consistent with our earlier argument that forest dislocations play an important role in the stress reduction transient because a high σ_{in} creates a high microstructural strength due to a higher forest dislocation density, resulting in low constant structure creep rates. The effect of the forest dislocations becomes increasingly important when the applied stress is high.

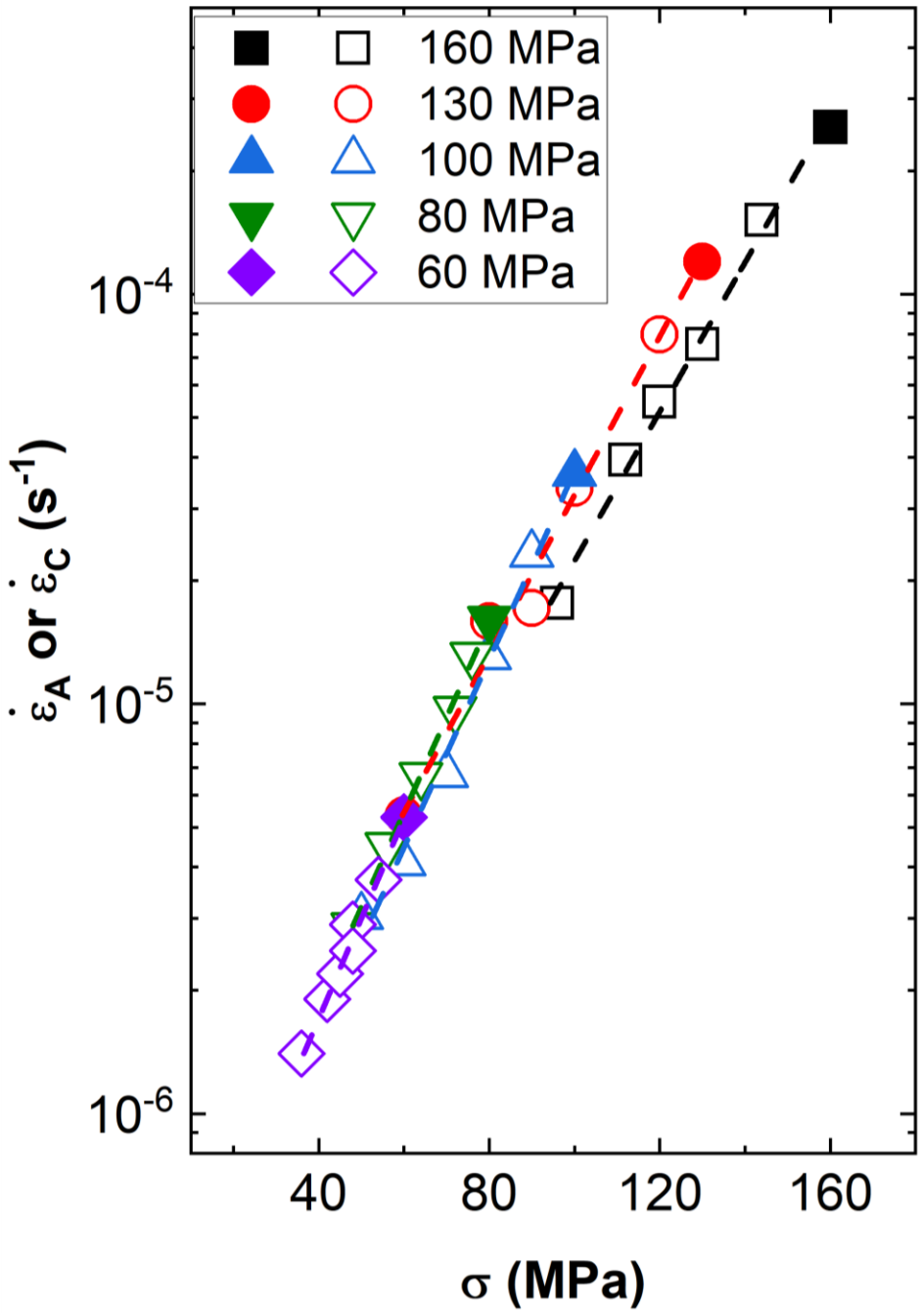

Fig. 6-7 Semi-logarithmic plot of the constant structure creep rate, $\dot{\epsilon}_C$, versus applied stress for CrMnFeCoNi crept at 1073 K. The solid symbols are $\dot{\epsilon}_A$ deforming under σ_{in} and the empty symbols are $\dot{\epsilon}_D$ deforming under σ_{red}. The legend denotes the five series of stress reduction creep experiments starting from their designated σ_{in} values. The dashed lines are linear fits of the constant structure data that delineates an exponential relationship.

6.3.3 Thermal Activation Parameters

The activation areas of CrMnFeCoNi obtained under different σ_{in} calculated by Eqn. 6.3 are given in **Table 6-2** and shown in Fig. 6-8. The values of $\Delta a''$ are on the order of ~100 b^2 and are consistent with those determined at room temperature and cryogenic temperatures [16-18]. Thus, plastic deformation is likely to be controlled by similar mechanisms to those found in the same material at lower temperatures. This argument is supported by our earlier discussion of stress reduction creep transients and TEM characterization, where a striking resemblance of dislocation substructure was revealed for plastic deformation in CrMnFeCoNi at large plastic strains across cryogenic, room, and elevated temperatures. In addition, the activation area decreases monotonically with increasing stress, which indicates the contribution of forest dislocations to relevant glide obstacles because forest dislocation spacing also decreases with increasing stress. We note that the stress dependence of the activation area obtained in our stress reduction creep tests at elevated temperatures is similar to the plastic strain dependence of the activation area obtained in strain rate jump tests and stress relaxation tests, suggesting a common behavior. Therefore, we conclude that the rate-determining deformation mechanisms in CrMnFeCoNi at 1073 K are dislocation-solute interactions and forest dislocation interactions and are the same as those at lower temperatures. This observation also rationalizes the stress exponent of 3.7 obtained previously [23], as it is in between the characteristic stress exponents of solid solution control (~3) and that of forest dislocations control (~5). In a recent review paper on the mechanical properties of HEAs, George, *et al.* [4] pointed out that although new deformation mechanisms have not yet been detected in HEAs, novel combinations of known mechanisms are usually seen. The elevated-temperature deformation of CrMnFeCoNi indeed follows this observation: the expected recovery and diffusion control is missing, and the deformation modes

at lower temperatures continue to operate at elevated temperatures. This finding implies that the existing models that describe plastic deformation at room temperature can be extended to elevated temperatures without significant modification.

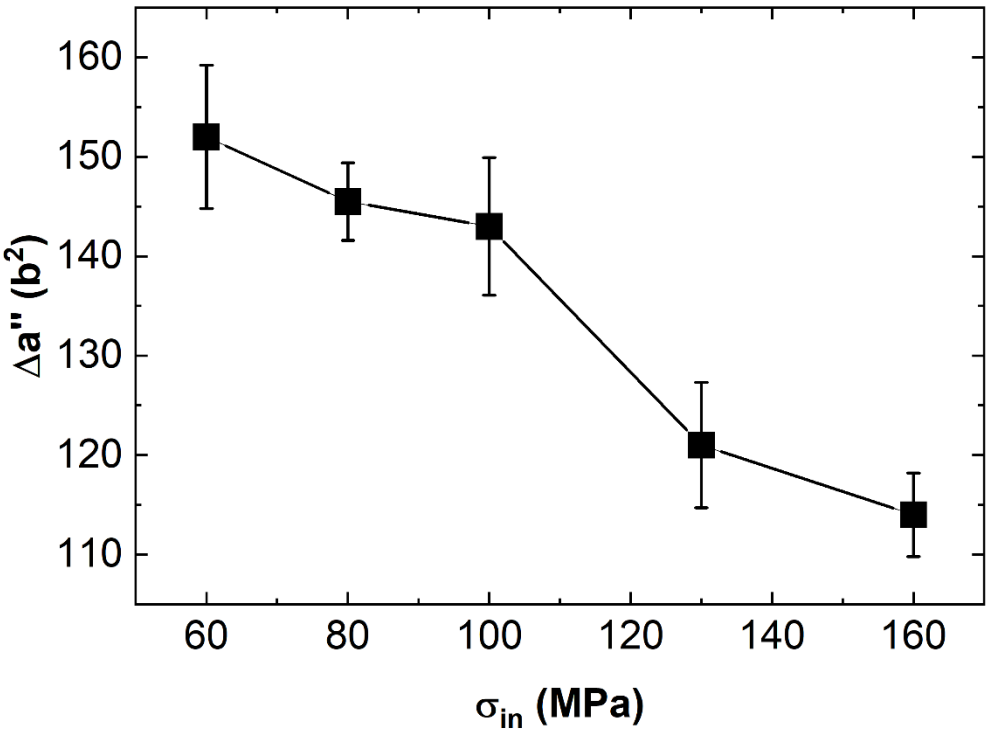

Fig. 6-8 The relationship between the operational activation area, $\Delta a''$, and the initial stress, σ_{in}. The data points were connected with straight lines merely to illustrate the trend.

Table 6-2 Thermal activation parameters for plastic deformation in CrMnFeCoNi at 1073 K described by the thermally activated glide model (Eqn. 6.4).

σ_{in} (MPa)	$\Delta a''$ (b^2)	ΔF (kJ/mol)	$\hat{\sigma}$ (MPa)	ΔG (kJ/mol)
160	114		458	111
130	121		432	119
100	143	170*	365	124
80	145		359	133
60	153		343	141

*Determined for all applied stresses.

It is often of interest to determine the mechanical strength of the microstructure, $\hat{\sigma}$, as it represents the flow stress of the material at 0 K and is essential to determining the glide kinetics of the dislocations. A phenomenological thermally activated glide model that incorporates a single structure parameter, $\hat{\sigma}$, is given by Kocks, *et al.* [10]:

$$\dot{\epsilon} = \dot{\epsilon}_0 \, exp\left[-\frac{\Delta F}{k_B T}\left(1 - \left(\frac{\sigma}{\hat{\sigma}}\right)^p\right)^q\right] \tag{6.4}$$

with:

$$\Delta G = \Delta F\left(1 - \left(\frac{\sigma}{\hat{\sigma}}\right)^p\right)^q \tag{6.5}$$

where p and q are constants that describe the strength and the range of the obstacles. We use p = q = 1 here for simplicity since it is clear from Fig. 6-7 that a direct exponential relationship is adequate to describe the relationship between $\dot{\epsilon}$ and σ. Therefore, the partial derivative of $\ln \dot{\epsilon}$ with respect to σ is (designated as β):

$$\beta = \frac{\partial \ln \dot{\epsilon}}{\partial \sigma} = \frac{\Delta F}{k_B T \hat{\sigma}} \tag{6.6}$$

Since dislocation solute interactions and forest dislocations operate at different length scales, their contribution to $\hat{\sigma}$ can be assumed to be linearly additive:

$$\hat{\sigma} = \hat{\sigma}_{ss} + \hat{\sigma}_f \tag{6.7}$$

where $\hat{\sigma}_{ss}$ is the flow stress contribution of solid solution hardening at 0 K and $\hat{\sigma}_f$ is that for forest dislocation hardening. Eqn. 6.7 neglects the Hall-Petch contribution to the flow stress, which is proven to be a significant part at room and cryogenic temperatures [18]. However, the Hall-Petch effect is not observed for steady-state creep deformation, as the creep rates in the dislocation creep regime are not known to have a grain size dependence except when deformation is diffusional [57]. Therefore, the Hall-Petch effect is not considered in our study. $\hat{\sigma}_f$ can be further written as $(\alpha\mu b\sqrt{\rho}\,)/M$, where α is the Taylor hardening factor, μ is the shear modulus, and ρ is the forest dislocation density. Since $\sqrt{\rho}$ is proportional to σ_f for metallic materials, $\hat{\sigma}_f$ has a linear dependence on σ_f and we obtain:

$$\hat{\sigma}_f = k_f \sigma_f \tag{6.8}$$

where k_f is a dimensionless constant that incorporates all the material constants related to the above equations, and σ_f is the applied stress partitioned on forest dislocations. Combining Eqn. 6.6-6.8, the inverse of β can now be written as:

$$\frac{1}{\beta} = \frac{k_B T \hat{\sigma}_{ss}}{\Delta F} + \frac{k_B T k_f}{\Delta F} \cdot \sigma_f \tag{6.9}$$

In Eqn. 6.9, β is already determined in the linear fits in Fig. 6-7, and $\hat{\sigma}_{ss}$ is calculated by Laplanche, *et al.* [18] to be 318 MPa. $\sigma_f = \sigma - \sigma_{ss}$ can be determined by the knowledge of σ_{ss} at 1073 K, which in strain rate-controlled tests can be estimated as the yield strength of the material. However, in stress-controlled creep tests, a yield strength is not defined. Therefore, σ_{ss} has to be

estimated by other means. Here we use the recent solid solution hardening model for concentrated random solid solutions developed by Varvenne, *et al.* [19, 20], where the expression of the temperature and strain rate dependent σ_{ss} is given by:

$$\sigma_{ss} = \hat{\sigma}_{ss} \cdot \frac{\mu(T)}{\mu_0} \left[1 - \left(\frac{k_B T}{\Delta E_b \cdot \frac{\mu(T)}{\mu_0}} \cdot \ln\left(\frac{\dot{\epsilon}_0}{\dot{\epsilon}}\right) \right)^{\frac{2}{3}} \right] \tag{6.10}$$

where $\mu(T) = 85 - 16/\exp[(448/T) - 1]$ (GPa) is the temperature dependent shear modulus for CrMnFeCoNi [58], μ_0 is the shear modulus at 0 K, $\dot{\varepsilon}_0$ is the reference strain rate and can be taken as 10^5 s^{-1} [19], and ΔE_b is the theoretical zero temperature activation barrier for dislocation glide in a concentrated solid solution matrix and is equal to 0.905 eV calculated in Ref. [18]. The good accuracy of Eqn. 6.10 at room and cryogenic temperatures has been verified for many HEAs by extensive experimental evidence, including CrMnFeCoNi [18, 19, 59, 60], and the application of the model at elevated temperatures can be justified by the fact that the deformation mechanisms at 1073 K turn out to be similar to those at lower temperatures. Furthermore, the model could even be more accurate at elevated temperatures because the SRO effect in HEAs that the model does not take into account is less prominent at high temperatures and is weakened at the large plastic strains used in the current study. A quick validation can be performed by using Eqn. 6.10 to calculate the yield strength at 1073 K and compare it to existing experimental data. Excellent agreement is reached as the calculated value, 70 MPa, is almost equal to the yield strength extrapolated to infinite grain size, 69 MPa, reported by Otto, *et al.* [32].

With known σ_{ss} and $\hat{\sigma}_{ss}$, ΔF can be determined by the intercept in a linear fit of $1/\beta$ versus σ_f as shown in Fig. 6-9. The goodness of fit, R^2, is determined to be 0.95, which validates the

relationship given in Eqn. 6.8. Once ΔF is known, ΔG and $\hat{\sigma}$ can be calculated from Eqn. 6.5 and 6.6, respectively. The values of ΔF, ΔG and $\hat{\sigma}$ are given in **Table 6-2**. The stress dependent ΔG determined from the constant structure creep data turns out to be lower than the apparent activation energy, Q, determined from the steady-state creep data (~225 kJ/mol at 60 MPa and ~219 kJ/mol at 80 MPa) in our previous study [23]. Since ΔG is determined at constant structure and is a more fundamental quantity than Q, their difference indicates that the temperature dependence of the microstructure strongly influences the measured activation energy (note that Q is determined from creep data across different temperatures at a constant stress, commonly normalized by temperature-dependent modulus) . In fact, one can qualitatively predict that Q must be higher than ΔG because the microstructure is softer at higher temperatures, leading to an increase of creep rates at the high temperature regime (or the left end of an Arrhenius plot) and therefore an overestimation compared to the true activation energy at constant structure. The study of the temperature dependence of creep microstructure is beyond the scope of the current study and referred to future work. Nevertheless, both ΔG and Q are much lower than the activation energy of lattice diffusion in CrMnFeCoNi (~300 kJ/mol [61]), which serves an extra piece of evidence that creep in this HEA is not diffusion (climb) controlled. The important fact that creep in CrMnFeCoNi is controlled by thermally activated dislocation glide instead of diffusion suggests that earlier speculation of the role of sluggish diffusion and solute drag effects [21, 22, 25] based on phenomenological strain rate-stress relationships extended from conventional alloys are not relevant to the creep deformation in this HEA. On the other hand, $\hat{\sigma}$ unsurprisingly increases with increasing applied stress, showing again the forest dislocation contribution to the flow stress. The values are nearly twice those of pure Ni determined at a similar temperature [53], signifying a large contribution of solid solution hardening. However, it

is also evident that $\hat{\sigma}$ is much larger than the applied stress, which suggests a significant amount of thermal activation is needed to move dislocations. This partially explains why CrMnFeCoNi loses strength so quickly with rising temperature. Therefore, in order to obtain good creep resistance in FCC MPEAs, second phases must be added to provide athermal contributions to the flow stress.

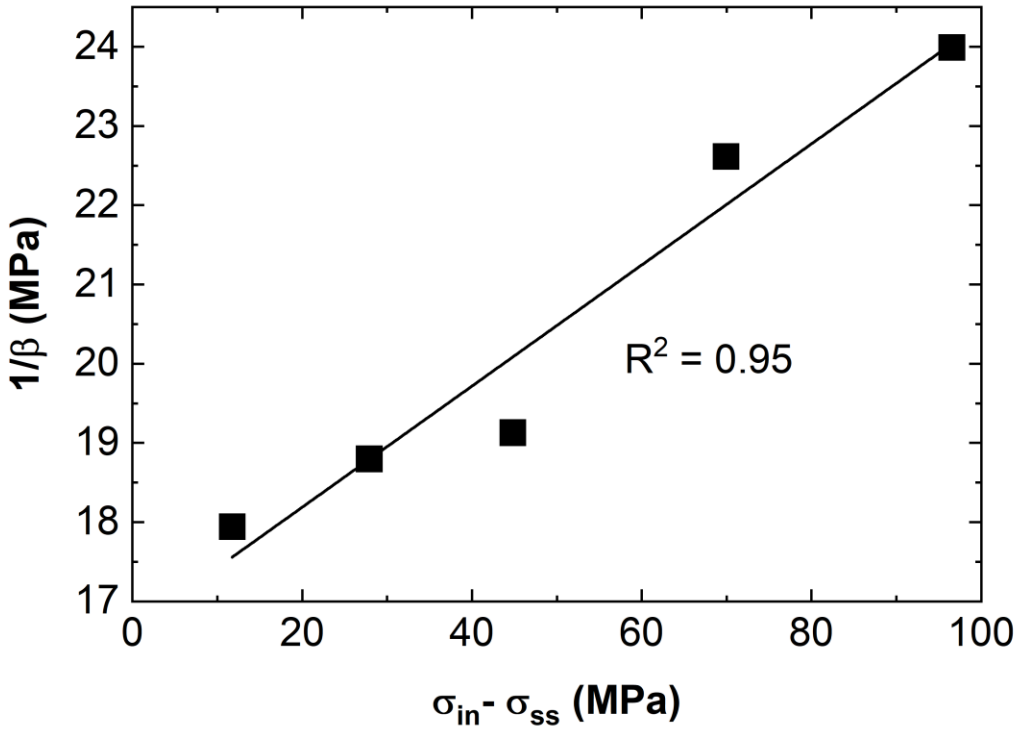

Fig. 6-9 The relationship between the inverse of the slope of ln $\dot{\epsilon}_C$ versus σ, denoted as $1/\beta$, and the initial stress, σ_{in}. The solid line is a linear fit of the data with a coefficient of determination (R^2) of 0.95.

6.3.4 Quantitative Separation of Multiple Mechanisms

Having identified the rate-controlling obstacles in CrMnFeCoNi to be the concentrated solid solution and the forest dislocations, these mechanisms can be readily separated by a standard procedure. Fig. 6-10 shows a schematic of a bowing dislocation interacting with both types of obstacles. As a first approximation, the average spacing between two pinning sites of these obstacles (l_{ss} and l_f) can be estimated as $\Delta a_{ss}''$ and $\Delta a_f''$ divided by b. Again, assuming the stress can be linearly partitioned onto the two obstacles, Eqn. 6.3 can be rewritten as:

$$\frac{1}{\Delta a''} = \frac{b}{Mk_BT} \cdot \frac{\partial \sigma}{\partial \ln \dot{\epsilon}} = \frac{b}{Mk_BT} \cdot \left(\frac{\partial \sigma_{ss}}{\partial \ln \dot{\epsilon}} + \frac{\partial \sigma_f}{\partial \ln \dot{\epsilon}} \right) = \frac{1}{\Delta a_{ss}''} + \frac{1}{\Delta a_f''} \tag{6.11}$$

Since $l_f = M\alpha\mu b/\sigma_f$ by the Taylor hardening relationship, we obtain:

$$\frac{1}{\Delta a_f''} = \frac{\sigma_f}{M\alpha\mu b^2} = C\sigma_f = C(\sigma - \sigma_{ss}) \tag{6.12}$$

where C is a material constant. Eqn. 6.11 then becomes:

$$\frac{1}{\Delta a''} = \frac{1}{\Delta a_{ss}''} + C(\sigma - \sigma_{ss}) \tag{6.13}$$

Therefore, the contribution of solid solution hardening and forest dislocation hardening can be quantitatively separated by plotting $\frac{1}{\Delta a''}$ (often normalized by b^2) versus $\sigma - \sigma_{ss}$ as shown in Fig. 6-11, which is also known as a Haasen plot [62]. The intercept of the linear fit gives the inverse of the activation area that is associated with solid solution hardening only, and $\Delta a_f{}''$ can then be obtained by Eqn. 6.11. The values of the separated activation areas and obstacle spacings, along with the separated microstructure strength and the temperature dependent flow stress, are given in **Table 6-3**.

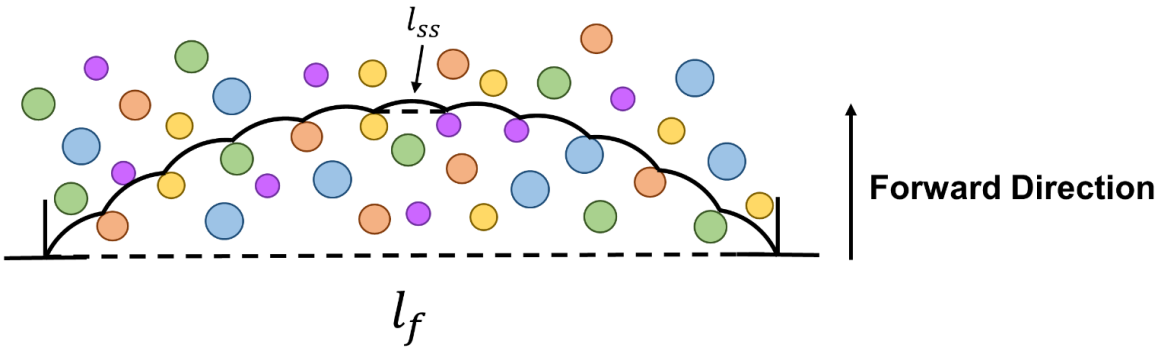

Fig. 6-10 Schematic of the dislocation configuration applied to separate the contributions of solid solution hardening and forest dislocation hardening. The values of the spacing between two adjacent pinning points for the two mechanisms are l_{ss} and l_f, respectively.

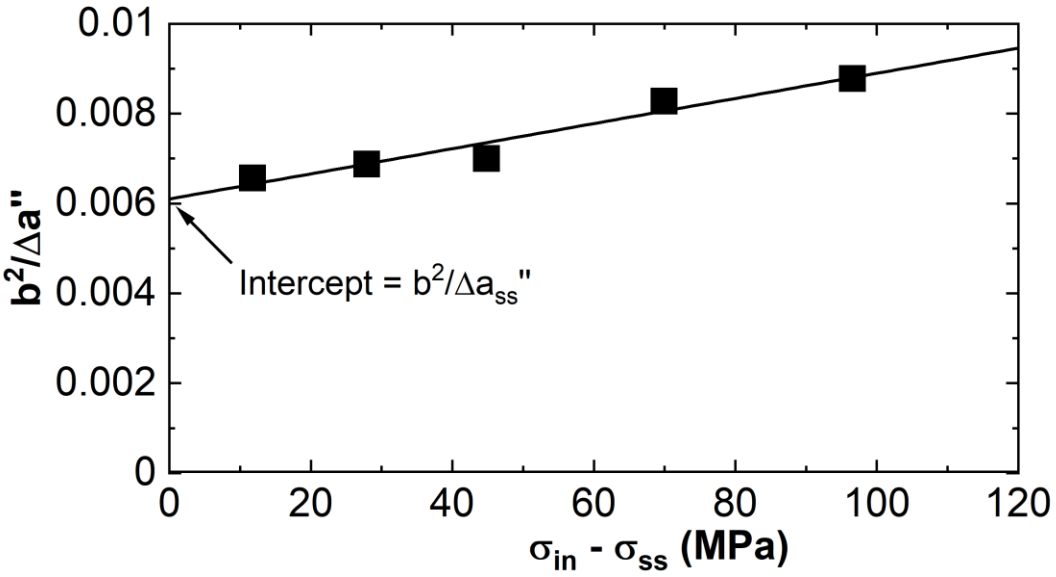

Fig. 6-11 The Haasen plot for CrMnFeCoNi deformed at 1073 K that describes the relationship between the inverse of the activation area (resolved in b^2) and the applied stress subtracted by the flow stress provided by solid solution hardening. The solid line is a linear fit of the data. The intercept of the fit represents the inverse of the separated activation area for solid solution hardening only.

Table 6-3 Separated thermal activation parameters for solid solution hardening and forest dislocation hardening to describe plastic deformation in CrMnFeCoNi at 1073 K.

σ_{in} (MPa)	σ_{ss} (MPa)	σ_f (MPa)	$\hat{\sigma}_{ss}$ (MPa)	$\hat{\sigma}_f$ (MPa)	$\Delta a_{ss}{}''$ (b^2)	l_{ss} (nm)	$\Delta a_f{}''$ (b^2)	l_f (nm)
160	64	96		140			373	95
130	60	70		114			460	117
100	55	45	318*	47	164*	42*	1111	283
80	52	28		41			1284	327
60	48	12		25			2145	547

*Determined for all applied stresses.

The most important observation in **Table 6-3** is that the ratio $\sigma_{ss}/\hat{\sigma}_{ss}$ is much smaller than that of $\sigma_f/\hat{\sigma}_f$, even though σ_{ss} and σ_f themselves are comparable. This implies that the amount of thermal activation needed for dislocations to overcome the solid solution barrier is much larger than that for forest dislocations, which is a critical feature of creep deformation in MPEAs. In addition, the average spacing for solid solution barriers, l_{ss}, is measured to be ~40 nm, which is on the same order as its calculated value ~20 nm by Varvenne, *et al.* [19]. On the other hand, $\Delta a_f''$ for CrMnFeCoNi is in good accordance with measured values for pure metals that feature forest dislocations only [15, 26, 27, 63], and l_f resides within the submicron range for low to intermediate stresses.

Finally, a constitutive equation can be given to describe the steady-state creep behavior of CrMnFeCoNi at 1073 K using Eqn. 6.4, and the necessary parameters can be found in **Table 6-2** and **Table 6-3**. A satisfactory fit was obtained as shown in Fig. 6-12, which suggests that the steady-state creep rate vs. stress relationship can also be represented by an exponential equation in the thermally activated glide framework besides the more well-known and phenomenological power-law equation.

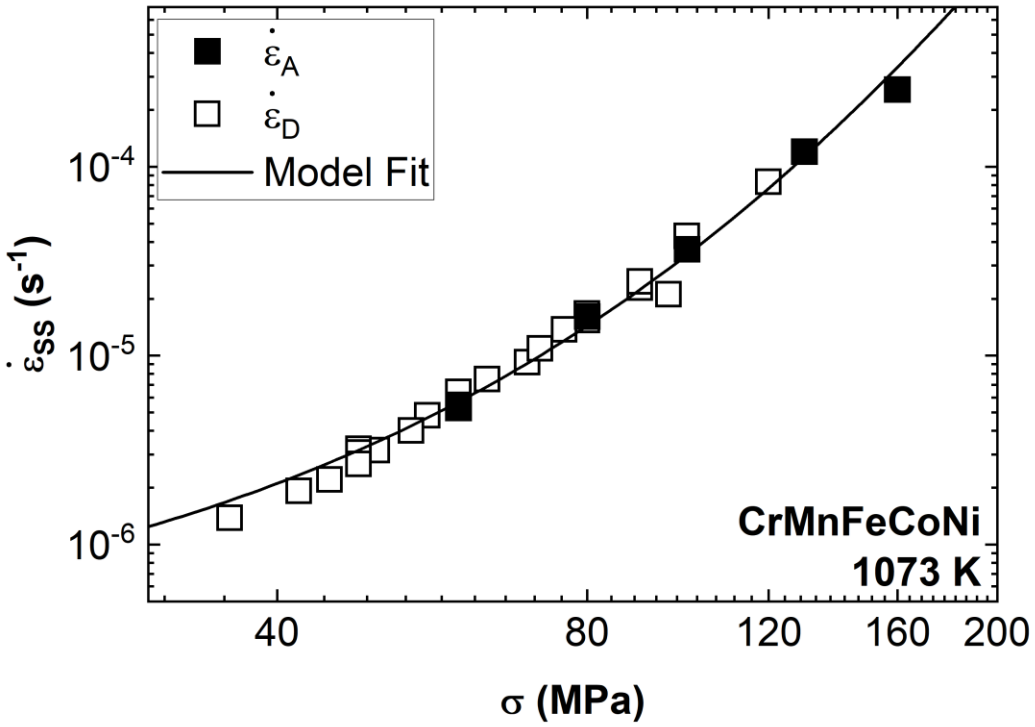

Fig. 6-12 Double logarithmic plot of the steady-state creep rates, $\dot{\epsilon}_A$ (solid symbols) and $\dot{\epsilon}_D$ (empty symbols), versus applied stress for CrMnFeCoNi crept at 1073 K. The solid line shows the thermally activated glide model fit (Eqn. 6.4) to the creep data.

6.4 Conclusions

In this paper, we present the results of a series of stress change experiments designed to probe the mechanisms of elevated-temperature creep deformation of the single-phase FCC CrMnFeCoNi high-entropy alloy. The major findings of this paper are the following:

(1) The primary creep and stress reduction creep transients in CrMnFeCoNi are much smaller than those observed in pure metals and conventional alloys, which is consistent with the simplicity of the substructure in this material observed in TEM observations. Such characteristics result in very accessible steady states for which the steady-state creep rate can be considered as a state function of temperature and stress with a negligible dependence on load history.

(2) The creep rates in CrMnFeCoNi after stress reduction feature a continuous increase to their subsequent steady-state values at the reduced stress. The stress dependence of the stress reduction transients reveals that the softening of the microstructure is likely to originate from the decrease of forest dislocation density.

(3) The activation areas for creep in CrMnFeCoNi have a magnitude ~100 b^2 and scale inversely with the applied stress. These values agree well with those measured at room and cryogenic temperatures, suggesting the rate-controlling deformation mechanisms in CrMnFeCoNi are dislocation-solute interactions and forest dislocation interactions. The Helmholtz free energy of creep was determined to be 170 kJ/mol, which is significantly lower than the activation energy of lattice diffusion. The combined results reveal creep in

CrMnFeCoNi is not diffusion controlled under the applied stresses investigated in the present study.

(4) Mechanical separation of the two rate-controlling mechanisms was successfully conducted using a Haasen plot. The large solid solution contribution to the microstructural strength and its large value compared to the partitioned applied stress demonstrates great importance of thermal activation in creep of CrMnFeCoNi. The activation areas separated for solid solution hardening and forest dislocation hardening are consistent with the values measured for conventional alloys, which reflects that there are no new mechanisms for the steady-state creep deformation in CrMnFeCoNi. The overall results from this paper suggest that the current plastic deformation theories for FCC MPEAs validated at room and cryogenic temperatures can be directly extended to elevated temperatures.

Acknowledgements

Research at ORNL was supported by the U.S. Department of Energy, Office of Science, Basic Energy Sciences, Materials Sciences and Engineering Division. Research at UC Davis did not receive any specific grant from funding agencies in the public, commercial, or not-for-profit sectors.

References

[1] D.B. Miracle, O.N. Senkov, Acta Mater. 122 (2017) 448-511.
[2] O.N. Senkov, D.B. Miracle, K.J. Chaput, J.-P. Couzinie, J. Mater. Res. 33(19) (2018) 3092-3128.
[3] E.P. George, D. Raabe, R.O. Ritchie, Nat. Rev. Mater. 4(8) (2019) 515-534.
[4] E.P. George, W.A. Curtin, C.C. Tasan, Acta Mater. 188 (2020) 435-474.
[5] B. Gludovatz, A. Hohenwarter, D. Catoor, E.H. Chang, E.P. George, R.O. Ritchie, Science 345(6201) (2014) 1153-1158.
[6] B. Gludovatz, A. Hohenwarter, K.V.S. Thurston, H.B. Bei, Z.G. Wu, E.P. George, R.O. Ritchie, Nat. Commun. 7 (2016).
[7] T.M. Smith, A.C. Thompson, T.P. Gabb, C.L. Bowman, C.A. Kantzos, Sci. Rep. 10(1) (2020).
[8] F. Dobeš, H. Hadraba, Z. Chlup, A. Dlouhý, M. Vilémová, J. Matějíček, Mater. Sci. Eng., A 732 (2018) 99-104.
[9] Y.T. Chen, Y.J. Chang, H. Murakami, T. Sasaki, K. Hono, C.W. Li, K. Kakehi, J.W. Yeh, A.C. Yeh, Sci. Rep. 10(1) (2020) 12163.
[10] U.F. Kocks, A.S. Argon, M.F. Ashby, Prog. Mater. Sci. 19 (1975) 1-281.
[11] W.F. Hosford, The Mechanics of Crystals and Textured Polycrystals, Oxford University Press, Oxford, 1993.
[12] M.Z. Butt, Philos. Mag. 87(24) (2007) 3595-3614.
[13] O.D. Sherby, J.L. Robbins, A. Goldberg, J. Appl. Phys. 41(10) (1970) 3961-3968.
[14] B.J. Diak, S. Saimoto, Mater. Sci. Eng., A 234-236 (1997) 1019-1022.
[15] Z.S. Basinski, Philos. Mag. 4(40) (1959) 393-432.
[16] S.I. Hong, J. Moon, S.K. Hong, H.S. Kim, Mater. Sci. Eng., A 682 (2017) 569-576.
[17] Z. Wu, Y. Gao, H. Bei, Acta Mater. 120 (2016) 108-119.
[18] G. Laplanche, J. Bonneville, C. Varvenne, W.A. Curtin, E.P. George, Acta Mater. 143 (2018) 257-264.
[19] C. Varvenne, G.P.M. Leyson, M. Ghazisaeidi, W.A. Curtin, Acta Mater. 124 (2017) 660-683.
[20] C. Varvenne, A. Luque, W.A. Curtin, Acta Mater. 118(C) (2016) 164-176.
[21] C. Cao, J. Fu, T. Tong, Y. Hao, P. Gu, H. Hao, L. Peng, Entropy 20(12) (2018).
[22] J.Y. He, C. Zhu, D.Q. Zhou, W.H. Liu, T.G. Nieh, Z.P. Lu, Intermetallics 55 (2014) 9-14.
[23] M. Zhang, E.P. George, J.C. Gibeling, Scr. Mater. 194 (2021) 113633.
[24] V. Maier-Kiener, B. Schuh, E.P. George, H. Clemens, A. Hohenwarter, J. Mater. Res. 32(14) (2017) 2658-2667.
[25] Y.B. Kang, S.H. Shim, K.H. Lee, S.I. Hong, Mater. Res. Lett. 6(12) (2018) 689-695.
[26] G.S. Nakayama, J.C. Gibeling, Acta Metall. Mater. 38(10) (1990) 2023-2030.
[27] S.E. Broyles, J.C. Gibeling, Scr. Metall. Mater. 33(5) (1995) 767-772.
[28] M. Zhang, S.E. Broyles, J.C. Gibeling, Acta Mater. 196 (2020) 384-395.
[29] M. Zhang, J.C. Gibeling, Scr. Mater. 190 (2021) 131-135.
[30] G. Laplanche, S. Berglund, C. Reinhart, A. Kostka, F. Fox, E.P. George, Acta Mater. 161 (2018) 338-351.
[31] K.A. Rozman, M. Detrois, T. Liu, M.C. Gao, P.D. Jablonski, J.A. Hawk, J. Mater. Eng. Perform. 29 (2020) 5822–5839.

[32] F. Otto, A. Dlouhy, C. Somsen, H. Bei, G. Eggeler, E.P. George, Acta Mater. 61(15) (2013) 5743-5755.
[33] B. Gludovatz, E.P. George, R.O. Ritchie, JOM 67(10) (2015) 2262-2270.
[34] G. Laplanche, A. Kostka, O.M. Horst, G. Eggeler, E.P. George, Acta Mater. 118 (2016) 152-163.
[35] E.J. Pickering, R. Muñoz-Moreno, H.J. Stone, N.G. Jones, Scr. Mater. 113 (2016) 106-109.
[36] B. Schuh, F. Mendez-Martin, B. Völker, E.P. George, H. Clemens, R. Pippan, A. Hohenwarter, Acta Mater. 96 (2015) 258-268.
[37] M.J. Mills, J.C. Gibeling, W.D. Nix, Acta. Metall. 33(8) (1985) 1503-1514.
[38] E.N.D.C. Andrade, B. Chalmers, Proc. R. Soc. Lond., A 138(835) (1932) 348-374.
[39] M. Biberger, J.C. Gibeling, Acta Metall. Mater. 43(9) (1995) 3247-3260.
[40] F. Bachmann, R. Hielscher, H. Schaeben, Texture Analysis with MTEX – Free and Open Source Software Toolbox, Solid State Phenom. 160 (2010) 63-68.
[41] S.E. Broyles, M. Zhang, J.C. Gibeling, Mater. Sci. Eng., A 779 (2020).
[42] O.D. Sherby, P.M. Burke, Prog. Mater. Sci. 13 (1968) 323-390.
[43] A.S. Argon, A.K. Bhattacharya, Acta. Metall. 35(7) (1987) 1499-1514.
[44] R. Horiuchi, M. Otsuka, Trans. Jpn. Inst. Met. 13(4) (1972) 284-293.
[45] C. Phaniraj, M. Nandagopal, S.L. Mannan, P. Rodriguez, Acta Metall. Mater. 39(7) (1991) 1651-1656.
[46] S.K. Mitra, D. McLean, N.P. Allen, Proc. R. Soc. Lond., A 295(1442) (1966) 288-299.
[47] J.H. Gittus, Philos. Mag. 23(186) (1971) 1281-1296.
[48] J.C. Gibeling, W.D. Nix, Acta. Metall. 29(10) (1981) 1769-1784.
[49] G.J. Lloyd, R.J. McElroy, Philos. Mag. 32(1) (1975) 231-244.
[50] L.O. Bueno, R.L. Bell, Mater. Sci. Eng., A 410-411 (2005) 72-78.
[51] F. Mompiou, D. Caillard, M. Legros, H. Mughrabi, Acta Mater. 60(8) (2012) 3402-3414.
[52] O. Bouaziz, J. Moon, H.S. Kim, Y. Estrin, Scr. Mater. 191 (2021) 107-110.
[53] G.S. Nakayama, Ph.D. Dissertation, University of California, Davis, 1990.
[54] J.C. Gibeling, W.D. Nix, Anomalous and Constant Substructure Creep Transients in Pure Aluminum, in: R.C. Gifkins (Ed.) International Conference on the Strength of Metals and Alloys (ICSMA 6), Pergamon Press, Melbourne, Australia, 1982, pp. 613-618.
[55] J. Hausselt, W. Blum, Acta. Metall. 24(11) (1976) 1027-1039.
[56] Z. Sun, S. Van Petegem, A. Cervellino, K. Durst, W. Blum, H. Van Swygenhoven, Acta Mater. 91 (2015) 91-100.
[57] H.J. Frost, M.F. Ashby, Deformation mechanism maps: the plasticity and creep of metals and ceramics, Pergamon Press, Oxford, 1982.
[58] G. Laplanche, P. Gadaud, O. Horst, F. Otto, G. Eggeler, E.P. George J. Alloy Compd. 623 (2015) 348-353.
[59] G. Bracq, M. Laurent-Brocq, C. Varvenne, L. Perrière, W.A. Curtin, J.M. Joubert, I. Guillot, Acta Mater. 177 (2019) 266-279.
[60] B. Yin, S. Yoshida, N. Tsuji, W.A. Curtin, Nat. Commun. 11(1) (2020) 2507.
[61] K.Y. Tsai, M.H. Tsai, J.W. Yeh, Acta Mater. 61(13) (2013) 4887-4897.
[62] P. Haasen, Philos. Mag. 3(28) (1958) 384-418.
[63] G.C. Kaschner, J.C. Gibeling, Acta Mater. 50(3) (2002) 653-662.

Chapter 7 Summary of Results and Opportunities for Future Research

The current study has investigated the creep properties and elevated-temperature deformation mechanisms of several DS alloys with various particle sizes, interparticle spacing, and nature of particle/matrix interfaces as well as a model FCC MPEA, CrMnFeCoNi, in great detail in preparation of modeling the DS-MPEAs that have only become available recently. As discussed in the chapters above, dispersion strengthening may be the most straightforward way to improve the creep strength of MPEAs as precipitation hardening will lead to significant complications in phase stability, which is both poorly studied and very difficult to predict due to the complex compositions in MPEAs. The most important findings of this dissertation are summarized below:

(1) For DS alloys with incoherent interfaces, the attraction between particle/matrix interfaces and dislocations dominates deformation and results in thermally activated detachment-controlled creep in GlidCop Al-15 and Al-60 with fine particles (~5 and 10 nm in size, respectively) and local climb-controlled creep in GRCop-84 with larger particles (~50 nm for the smaller particles). If the particle/matrix interface is coherent, this attraction disappears, and interdislocation interactions become more important instead, as shown in FVS0812.

(2) The threshold behavior observed in DS alloys crept under thermally activation detachment control originates from the thermodynamic back jumps of the just-detached dislocations to the attractive interfaces. A different origin was identified for DS alloys with larger particles where climb is more important. The threshold behavior of these

materials is believed to be caused by the increase in line length for the climbing dislocations.

(3) The steady-state creep deformation of CrMnFeCoNi is controlled by both forest dislocation hardening and concentrated solid solution hardening over a wide range of temperatures and stresses — the same deformation mode as that determined at room and cryogenic temperatures with twinning excluded. The pinning effect from the concentrated solid solution matrix remains dominant at elevated temperatures, leading to limited contributions of recovery and diffusion in this material. However, even though concentrated solid solution hardening constitutes a large portion of the material's flow strength, such hardening is thermal and will therefore diminish quickly as the temperature rises. The addition of hard second phases for athermal contributions to flow strength, such as dispersoids, is therefore considered critical to improve the creep strength of FCC MPEAs.

The above findings carry significant implications in the future development creep resistant FCC MPEAs. Firstly, the quantitative understanding of the deformation mechanisms in the selected DS alloys can be extended to a broad range of other DS alloys based on different material systems and dispersoids, including DS-MPEAs. Hence, once the dispersoid size and distribution as well as the nature of particle/matrix interface are determined for future DS-MPEAs candidates, the type of dislocation/particle interaction can be deduced with minimal amount of creep testing and microstructural characterization. Secondly, the significant pinning effect of the concentrated solid solution will lead to a much lower dislocation mobility in the MPEA matrix

compared to pure metals, which means that the constitutive equations that are solely based on dislocation/particle interactions will not suffice. Instead, a composite model is need to combine the contributions from the matrix and the dispersoids to the resistance to dislocation motion. Finally, the high dislocation density observed in the creep microstructure of the MPEA also implies potentially complicated interdislocation forces on the dislocations that interact with the particles, which in turn results in internal stresses that are difficult to model. Thankfully, these internal stresses and lattice strain can now be measured *in-situ* with state-of-the-art TEM techniques (e.g., nanobeam diffraction, 4D-STEM) [1, 2].

In addition, this investigation has shown the many merits of utilizing a combination of mechanical microscopy and electron microscopy to probe the rate-controlling deformation mechanisms and obtain quantitative descriptions of plastic deformation in the materials. It is therefore desirable to make these efforts customary in the high-temperature testing protocol since obtaining knowledge of the operating deformation modes and microstructure and their correlation to the mechanical properties is the key process to success. Although the current experimental framework has brought forth significant advances towards our understanding of the selected materials, various research avenues still remain open to complement and extend the results that are generated by the above approach. This section thereby identifies several opportunities for future research that will be extremely helpful for the development of state-of-the-art high-temperature structural materials with increasingly complex microstructures and deformation behaviors.

The information obtained by the stress reduction creep experiments presented in the current study reflects an average behavior of dislocations interacting with mesoscale obstacles in the time frame above or equal to microseconds throughout the microstructure of bulk specimens. Therefore, even though these experiments provide adequate information for average thermal activation parameters to describe dislocation kinetics used in the creep models, they have systematic difficulties in probing: (i) local behaviors that vary spatially within the sample; (ii) obstacles that have their length scales below mesoscale; and (iii) processes that occur with time scales below microseconds. Unfortunately, current materials of interest usually have large spatial fluctuations of physical properties (e.g. MPEAs [3, 4]) and form important microstructures on the nano- or even subnano- scales (e.g. short range order (SRO) clusters [5, 6]). In order to study these features that are ubiquitous in today's materials, dedicated *in-situ* nanomechanical tests with finer probes and computer simulations need to be incorporated. Several opportunities for future research that can directly complement the findings in this dissertation are given as follows:

(1) In **Chapter 2**, the thermodynamic back jumps of the dislocations is considered to be the physical origin of the observed threshold behavior. The implementation of this insight to the constitutive equation relies on many assumptions that are due for further verification. For example, the attraction between the particle/matrix interface and the dislocation is assumed to only exist within one atomic distance from the particle, and any longer range attraction is accounted for by a phenomenologically fitted constant, which is vulnerable to absorbing errors from other sources. The activation barrier for back jump is assumed to only consist of the contribution from the applied stress, which needs to be necessarily small to achieve an adequate number of back jumps, resulting in fast motion that is beyond the time resolution of any characterization technique that can directly observe this

behavior. Therefore, it is desirable to carry out molecular dynamics (MD) simulations to verify the back jump processes with a gradient of applied stresses (from zero to a small value). The activation energies for back jump and forward jump can then be extracted and compared to experimental values. These values are also critical inputs for further kinetic Monte Carlo (kMC) or dislocation dynamics (DD) simulations that can generate deformation results comparable to those obtained in bulk experiments.

(2) In **Chapter 3**, dislocation local climb over particles is determined to be the rate controlling deformation mechanism in GRCop-84. Unlike detachment, local climb is a multistep process and cannot be described by the framework of thermally activated glide. Specifically, the activation energy measured by the experiment is correlated with an average time that the dislocations are held at the particles for local climb events to start and finish. Detailed information of the local climb process *per se* (e.g. change of dislocation configuration, the effect of the dislocation-particle/matrix interface attraction) is completely missing. Therefore, a combination of *in-situ* creep experiments and DD simulations can be performed to further understand this process. Since local climb occurs at an activation energy of at least that for interfacial diffusion, it can be directly observed under a TEM with *in-situ* deformation and heating capability. DD simulations can also be included to complement the TEM study with relative ease since the lattice constants and the shear moduli of the matrix and the particles, the size and distribution of the particles, and the climb mobility of dislocations in the matrix (pure Cu) are already known.

(3) In **Chapter 6**, the interesting primary creep behavior in the CrMnFeCoNi MPEA deserves extensive further attention. Not only is this behavior not observed in conventional alloys, this transition from normal to inverted primary creep due to the difference in the applied stress has profound implications towards the engineering application of this material. To date, almost all research on creep is focused on steady-state behavior because the stability of the microstructure allows for relatively easy interpretation of creep data. However, the design criteria of any engineering part will hardly endure such high plastic strain (i.e. the materials serve entirely in the primary stage!). Therefore, an inverted primary creep will be highly desirable because the material starts from zero creep rate in the initial stage of deformation. This intriguing behavior has turned out not to linger, as the steady-state creep rates are not affected by the different behaviors observed in primary creep. The initial hardening behavior and its subsequent destruction is likely to come from the SRO that is often reported in MPEAs. Even though SRO can be readily observed by state-of-the-art TEMs [5, 6], little is known about its effects on the mechanical properties in the MPEAs. Therefore, dedicated *in-situ* TEM experiments (e.g. *in-situ* nanoindentation on a push-to-pull device) need to be performed at elevated temperatures to directly observe the dislocation behavior and substructure and meanwhile compare with the stress-strain curves. *In-situ* strain rate jump tests can also be incorporated to determine activation area that informs the relevant deformation mechanisms in small samples. Besides TEM work, conventional creep tests remain important to infer bulk mechanical properties during primary creep. However, the microstructure is constantly changing, highlighting the importance of a good characterization of the initial microstructure and the conservation of the deformation

microstructure. The first aspect can be accounted for by extensive microhardness, EBSD, and *ex-situ* TEM characterization, and the second can be guaranteed by incorporating rapid sample cooling under load, achieved by a flowing inert gas and a detachable furnace.

References

[1] C. Ophus, Microsc. Microanal. 25(3) (2019) 563-582.
[2] C. Mahr, K. Müller-Caspary, T. Grieb, F.F. Krause, M. Schowalter, A. Rosenauer, Ultramicroscopy 221 (2021) 113196.
[3] W.G. Nöhring, W.A. Curtin, Acta Mater. 128 (2017) 135-148.
[4] T.M. Smith, M.S. Hooshmand, B.D. Esser, F. Otto, D.W. McComb, E.P. George, M. Ghazisaeidi, M.J. Mills, Acta Mater. 110 (2016) 352-363.
[5] R. Zhang, S. Zhao, J. Ding, Y. Chong, T. Jia, C. Ophus, M. Asta, R.O. Ritchie, A.M. Minor, Nature 581(7808) (2020) 283-287.
[6] X. Chen, Q. Wang, Z. Cheng, M. Zhu, H. Zhou, P. Jiang, L. Zhou, Q. Xue, F. Yuan, J. Zhu, X. Wu, E. Ma, Nature 592(7856) (2021) 712-716.

Appendix: Complete Listing of Creep Data

Table A1 Constant stress and stress reduction creep data for GlidCop Al-15 extruded (Al-15 AR) and 1273 K 100 hour anneald (AL-15 AN) as well as GlidCop Al-60 extruded (Al-60 AR) at 973 K. This data set corresponds to the results presented in Chapter 2.

Sample	Test Type	σ_{in} (MPa)	σ_{red} (MPa)	$\dot{\varepsilon}_A$ (s^{-1})	$\dot{\varepsilon}_D$ (s^{-1})	$\dot{\varepsilon}_C$ (s^{-1})
Al-15 AR	Constant Stress	45	--	4.20E-06	--	--
		50		9.80E-06		
		60		8.40E-05		
		65		1.29E-04		
	Stress Reduction	70	35	2.70E-04	5.20E-07	5.40E-06
			20		--	1.80E-07
			50		1.65E-05	1.80E-05
			40		2.70E-06	5.00E-06
			28		6.20E-09	6.30E-07
Al-15 AN	Constant Stress	40	--	3.20E-08	--	--
		54		8.80E-06		
	Stress Reduction	70	55	2.10E-04	1.46E-05	2.60E-05
			50		4.50E-06	1.10E-05
			45		1.60E-06	5.30E-06
			40		5.90E-08	7.40E-07
			35		1.50E-08	4.80E-07
			30		2.00E-08	2.00E-07
Al-60 AR	Stress Reduction	80	60	3.20E-04	--	1.40E-04
			50			3.96E-05
			40			5.20E-06
		70	60	2.70E-05		5.00E-05
			55			3.10E-05
			40			1.60E-06

(Cont. Table A1)

			45			2.10E-06
			50			6.80E-06
		60	50	2.80E-06		3.40E-06
			45			1.30E-06

Table A2 Stress reduction creep data for production rolled GRCop-84 at 923 K. This data set corresponds to the results presented in Chapter 3.

Sample	Test Type	σ_{in} (MPa)	σ_{red} (MPa)	$\dot{\varepsilon}_A$ (s^{-1})	$\dot{\varepsilon}_D$ (s^{-1})	$\dot{\varepsilon}_C$ (s^{-1})
GRCop-84	Stress Reduction	95	55	1.41E-04	1.96E-06	3.10E-06
			65		8.76E-06	9.58E-06
			55		2.08E-06	4.80E-06
			45		5.51E-07	3.45E-06
			55		2.33E-06	9.29E-06
			65		6.90E-06	4.82E-06
			60		3.19E-06	2.81E-06
			50		9.58E-07	2.08E-05
			75		1.72E-05	3.10E-06
		80	65	2.97E-05	5.25E-06	6.74E-06
			50		8.24E-07	1.70E-06
			40		2.75E-07	5.59E-07
			60		2.68E-06	3.21E-06
			55		1.54E-06	2.38E-06
		65	55	6.25E-06	1.44E-06	1.44E-06
			60		5.18E-06	5.18E-06
			40		8.99E-08	8.99E-08
			50		6.30E-07	6.30E-07

Table A3 Constant stress and stress reduction creep data for FVS0812 unaged (UA), high-temperature aged at 798 K and 200 hours (HTA), and medium-temperature aged at 698 K and 200 hours (MTA) in nitrogen. This data set corresponds to the results presented in Chapter 4.

Sample	Test Type	Temperature (K)	σ_{in} (MPa)	σ_{red} (MPa)	$\dot{\varepsilon}_A$ (s^{-1})	$\dot{\varepsilon}_D$ (s^{-1})	$\dot{\varepsilon}_C$ (s^{-1})
UA	Constant Stress	573	135	--	8.70E-09	--	--
			179.6		1.10E-06		
			151.7		3.20E-08		
			206.9		1.60E-05		
		623	172.4	--	4.80E-04	--	--
			103.4		1.50E-08		
			110.3		7.20E-06		
		673	136.2	--	8.30E-04	--	--
			110.3		1.60E-05		
			96.5		2.30E-06		
			75.8		3.60E-08		
		723	71.8	--	1.20E-05	--	--
			60.1		1.10E-06		
		773	38.6	--	1.80E-06	--	--
			53.8		2.60E-04		
			27.6		2.80E-08		
		823	23.4	--	8.80E-05	--	--
			13.8		3.00E-08		
			20.7		4.70E-06		
	Stress Reduction	573	206.9	134.4	3.50E-05	8.70E-09	5.50E-06
				155.0		1.37E-07	1.03E-05
				186.0		3.00E-06	1.50E-05
			186.2	121.0	3.00E-06	4.14E-09	5.50E-07
				138.0		7.70E-09	8.60E-07
				167.5		3.70E-07	1.66E-06
		673	136.2	102.0	8.30E-04	5.76E-06	3.30E-05

(Cont. Table A3)

				122.4		1.00E-04	2.40E-04
				87.8		7.75E-07	4.05E-06
MTA	Constant Stress	573	206.9	--	1.64E-05	--	--
		673	110.3		1.70E-05		
		773	38.6		6.00E-06		
HTA		573	206.9	--	1.44E-04	--	--
		673	110.3		2.60E-04		
		773	38.6		1.40E-05		

Table A4 Constant stress creep data for 1173 K 1 hour annealed CrMnFeCoNi. This data set corresponds to the results presented in Chapter 5.

Sample	Test Type	Temperature (K)	σ_{in} (MPa)	σ_{red} (MPa)	$\dot{\varepsilon}_A$ (s^{-1})	$\dot{\varepsilon}_D$ (s^{-1})	$\dot{\varepsilon}_C$ (s^{-1})
CrMnFeCoNi	Constant Stress	1023	80	--	4.19E-06	--	--
			60		1.49E-06		
			40		3.52E-07		
			130		1.91E-05		
			130		2.00E-05		
			200		1.35E-04		
		1073	20		8.37E-08		
			40		1.12E-06		
			60		5.21E-06		
			80		1.42E-05		
			130		1.12E-04		
			100		3.21E-05		
		1123	40		4.51E-06		
			80		5.33E-05		
			30		1.40E-06		
			20		3.01E-07		
			60		1.85E-05		
		1173	60		4.16E-05		
			80		1.03E-04		
			40		1.14E-05		
			20		7.39E-07		

Table A5 Stress reduction creep data for 1173 K 1 hour annealed CrMnFeCoNi at 1073 K. This data set corresponds to the results presented in Chapter 6.

Sample	Test Type	σ_{in} (MPa)	σ_{red} (MPa)	$\dot{\varepsilon}_A$ (s^{-1})	$\dot{\varepsilon}_D$ (s^{-1})	$\dot{\varepsilon}_C$ (s^{-1})
CrMnFeCoNi	Stress Reduction	160	130	2.56E-04	--	7.55E-05
			112		--	3.94E-05
			96		2.11E-05	1.76E-05
			144		--	1.52E-04
			120		--	5.46E-05
		130	80	1.20E-04	1.67E-05	1.59E-05
			100		4.29E-05	3.37E-05
			60		6.43E-06	5.35E-06
			120		8.29E-05	7.98E-05
			90		2.29E-05	1.72E-05
		100	60	3.65E-05	5.46E-06	4.10E-06
			80		1.54E-05	1.30E-05
			70		9.21E-06	6.74E-06
			50		3.15E-06	3.03E-06
			90		2.47E-05	2.32E-05
		80	64	1.61E-05	7.50E-06	6.68E-06
			56		4.82E-06	4.51E-06
			72		1.09E-05	9.67E-06
			76		1.38E-05	1.31E-05
			48		3.21E-06	2.87E-06
		60	54	5.29E-06	4.01E-06	3.72E-06
			48		3.06E-06	2.90E-06
			42		1.92E-06	1.90E-06
			45		2.21E-06	2.19E-06
			36		1.38E-06	1.40E-06
			48		2.67E-06	2.50E-06